Search for Scalar Leptons at LEP with the L3 Detector

Ph.D. Thesis by

Lei Xia

Search for Scalar Leptons at LEP with the L3 Detector

Thesis by
Lei Xia

In Partial Fulfillment of the Requirements
for the Degree of
Doctor of Philosophy

California Institute of Technology
Pasadena, California

2002

(Submitted October 4, 2002)

Acknowledgment

I would like to express my gratitude for the support and guidance that my academic adviser, Harvey Newman, has given me throughout my graduate study at Caltech. This thesis, which is my very first major work in high energy physics, would have been impossible without his patience and help to me.

It was always a pleasure to work in the supersymmetry analysis group of the L3 experiment. I owe special thanks to Alvise Favara and Sylvie Rosier-Lees, and other group members: Guy Coignet, Jean Fay, Michel Chemarin, Imad Laktineh, Arnaud Balandras, Satyaki Bhattacharya, Ia Iashvili, Gerald Grenier, Marat Gataulline, Borhan Tellili, Serge Sushkov, Haijun Yang, and others.

I would like to thank Bing Zhou who gave me the chance to work on the radiation monitor, from which I got valuable experience on hardware and online software. I also want to thank J.J. Blaising, Chih-Hsun Lin, and Tong Xu, for their help in this work.

My sincere thanks go to my friends, Gang Chen, Changgen Yang, Zhongqiang Yu, Hesheng Chen, Yanan Guo, Guoming Chen, Min Yang, Honglin Zhuang, Jianguo Li, Qian Han, Zhenan Liu, Meng Wang, and many others from IHEP, Beijing; Ziping Zhang, Zizong Xu, Zhaoming Wang, Xiaolian Wang, Tong Xu, and Shuwei Ye from USTC, Hefei; Qun Deng, Hui Yuan, from SIC, Shanghai; Tiesheng Dai and Jianchun Wang from MIT; Xudong Cai and his family; Hanguo Wang from UCLA. Their friendship made my stay at CERN very pleasant. Thanks to the L3+Cosmic collaboration, and its members from IHEP, Beijing: Yuqian Ma, Linkai ding, Changquan Shen, Qingqi Zhu, Cailiu Jing, Haohua Kuang, Xiaofeng Yang, Zhiguo Yao, Yupeng Xu, Xinhua Ma, Yu Lei, Li Li, and many others. It is always a pleasure to discuss with them their interesting physics analysis.

The members of the Caltech group were always friendly and helpful. In particular, I would like to thank Renyuan Zhu, Liyuan Zhang, Sergey Shevchenko, Alvise Favara, Rihua Mao, and graduate students Wenwen Lu, Alexander Shvorob, and Marat Gataullin.

I am very grateful to Harvey Newman for his careful reading of the manuscript, thousands of corrections of my language, and many helpful suggestions. I would like to thank Sergey Shevchenko for his proofreading of my thesis.

My parents and sister always encourage and support me. I am sorry for not being able to visit them often enough.

Last but not least at all, my warmest thanks to Xu Peng, for her love and support. She makes my life so meaningful.

Abstract

In this thesis, I present a search for scalar leptons in e^+e^- annihilation using the L3 detector at LEP. Data collected in 1999 and 2000, at center-of-mass energies between 192 GeV and 208 GeV, was used in this analysis.

This work covered the scalar lepton searches in both SUGRA and GMSB models. To achieve this analysis, a parametrized selection was developed to handle the different event signatures in SUGRA models. Improvement of the L3 simulation and reconstruction program packages was carried out so that one can simulate the scalar leptons in GMSB models correctly. The simulation of the L3 Time Expansion Chamber (TEC) dE/dx measurement was rewritten to facilitate the analysis for a stable slepton signal, which is relevant in some parts of the parameter space in GMSB models.

In this analysis, we didn't observe any significant indication of scalar lepton production of any type. We achieved the following mass exclusion limits for scalar leptons in SUGRA models, for large ΔM ($\Delta M \ > \ 0.3 \times M_{\tilde{l}}$):

$$M_{\tilde{e}_R} \ > \ 97\ GeV \quad (expected\ 97\ GeV) \tag{1}$$

$$M_{\tilde{\mu}_R} \ > \ 86\ GeV \quad (expected\ 86\ GeV) \tag{2}$$

$$M_{\tilde{\tau}_R} \ > \ 78\ GeV \quad (expected\ 79\ GeV) \tag{3}$$

We achieved the following lifetime independent mass exclusion limits for scalar taus in GMSB models:

$$M_{\tilde{\tau}_R} \ > \ 80\ GeV \quad (expected\ 79\ GeV) \tag{4}$$

Contents

List of Tables

List of Figures

1. Introduction and Overview

In this thesis I present the search for scalar leptons which are predicted by supersymmetry theory. The analysis is performed in both Supergravity (SUGRA) and Gauge Mediated Supersymmetry Breaking (GMSB) scenarios. The motivation for this analysis is clear:

- The belief in a more beautiful and fundamental theory behind our current knowledge of particle interactions, the Standard Model, which might lead us to the ultimate understanding of our world. Currently, the best candidate is supersymmetry theory.
- For all the supersymmetric particles, scalar leptons are always among the top few that are most likely to be detected at current or next generation accelerator experiments, and thus to lead to the discovery of supersymmetry.

The data sample analyzed in this thesis was collected using the L3 detector at the LEP accelerator during its last two years of running, 1999 and 2000, when LEP reached its highest center-of-mass energies, ranging from 192 GeV to 208 GeV. The corresponding integrated luminosity is 233.2 pb^{-1} in 1999, and 217.3 pb^{-1} in 2000. LEP was a unique place to search for scalar leptons due both to its clean (machine and physics) background environment, and its ability of provide high center-of-mass energy and high luminosity at the same time. The L3 detector provided superior measurements of electrons, photons and muons by a precise BGO electromagnetic calorimeter and a large muon chamber system inside a 0.5 T magnetic field, which helped to measure the leptons in the final state of scalar lepton decay. However, these factors were counterbalanced by the compact size and hence the limited resolution of the central tracking system, as well as the limited acceptance of some other detectors.

This analysis covers scalar lepton searches in both the SUGRA and GMSB scenarios. In the first case, all of the scalar leptons have a very short lifetime, and we expect to observe a pair of acoplanar leptons in the final state with large missing energy. In the latter case, a scalar tau is always the lightest of the three slepton flavors, and it may have a short or a long lifetime. So we searched for scalar taus only, and developed several selections focusing on different lifetimes. The result of this analysis is interpreted in the framework of the Constrained Minimal Supersymmetric Standard Model.

The thesis is organized as follows.

Chapter 2 gives an overview of the Standard Model, its known problems, and its supersymmetric extension. At the end of this chapter, we also discuss the phenomenology issues in searching for scalar leptons.

Chapter 3 describes the LEP accelerator and the L3 detector, with emphasis on those issues relevant to this analysis, such as the LEP RF system upgrade, beam energy measurement, and various L3 subdetectors.

Chapter 4 covers the L3 radiation monitor which I was responsible for from 1998 to the end of LEP running. This detector provided real time protection of the L3 central tracking system, and gave measurements of the radiation background in the detector area. This chapter discusses both the hardware and the results.

Chapter 5 mainly discusses various simulation issues for this analysis. Since scalar leptons in the GMSB scenario may have long decay length, the simulation program must be able to trace long-lived particles with rather complicated decay modes. The L3 standard simulation program was upgraded for this purpose. The TEC dE/dx signal simulation was totally rewritten to correct many problems existing in the old version. This is crucial for the analysis of heavy stable charged particles, as well as some other analyses which require particle identification.

Chapter 6 describes the analysis for scalar leptons in the SUGRA scenario, in which sleptons decay promptly and leave a pair of acoplanar leptons. Large missing energy is also an important signature in this scenario. However, the configuration of the final state depends strongly on the mass difference between the slepton and the Lightest Supersymmetric Particle (LSP, assumed to be the lightest neutralino). To handle this complication, parametrized selections were developed.

Chapter 7 describes the analysis for scalar taus in GMSB models, in which the stau may have a very large range of possible lifetimes. To take into account all the possibilities, a series of selections were optimized for different decay lengths. This analysis is able to set a stau mass exclusion limit independent of its lifetime.

Chapter 8 summarizes the results obtained in this analysis, and compares them to those obtained in other experiments. A brief outlook for supersymmetry searches at current and future accelerators also is presented.

2. Theory: Standard Model and Supersymmetry

The Standard Model (SM), as an electroweak and strong interaction quantum gauge theory for particle physics, is extremely successful. However, it is believed that the Standard Model is not the ultimate particle theory, because of various concerns. Among many proposed new theories beyond the Standard Model, supersymmetry remains the most motivated and experimentally favored one, not only because it is the only possible extension of the known spacetime symmetries of particle theory, but also because it provides an elegant solution to the hierarchy problem, it may contain a dark matter candidate and it may lead to a grand unified theory. To search for evidence of supersymmetry, one can search directly for the new particles predicted by supersymmetry theory, including scalar leptons which are among the most promising to be found at LEP.

This chapter will give a brief overview of the Standard Model and supersymmetry theory, and at the end, discuss the motivation and various phenomenology issues for this analysis: the search for scalar leptons.

2.1 Standard Model

The Standard Model is a non-Abelian gauge theory, with the gauge group $SU(3)_C \times SU(2)_L \times U(1)_Y$. It incorporates the unified electroweak theory and Quantum Chromodynamics, and describes the electromagnetic, weak and strong interactions between elementary particles.

The particle spectrum of the SM consists of matter fields which are all fermions, gauge bosons that mediate the interaction and the Higgs boson. The fermions in the SM are listed in Table 2.1, and bosons are listed in Table 2.2, with their major quantum numbers. Leptons interact with other particles through electroweak interactions, while quarks also have strong interactions. Fermions came in families. Each family contains a left-handed lepton doublet, a right-handed lepton singlet, a left-handed quark doublet and two right-handed quark singlets. There are, in total, three known fermion families. The 2nd and 3rd are exact repetitions of the 1st family except for the particle masses. The reason for 3 largely identical family is not yet known.

families:	1	2	3	T_3	Y	Q	L	B
Leptons:	$\begin{pmatrix}\nu_e\\ e\end{pmatrix}_L$	$\begin{pmatrix}\nu_\mu\\ \mu\end{pmatrix}_L$	$\begin{pmatrix}\nu_\tau\\ \tau\end{pmatrix}_L$	$1/2$	-1	0	1	0
				$-1/2$	-1	-1	1	0
	e_R	μ_R	τ_R	0	-2	-1	1	0
Quarks:	$\begin{pmatrix}u\\ d\end{pmatrix}_L$	$\begin{pmatrix}c\\ s\end{pmatrix}_L$	$\begin{pmatrix}t\\ b\end{pmatrix}_L$	$1/2$	$1/3$	$2/3$	0	$1/3$
				$-1/2$	$1/3$	$-1/3$	0	$1/3$
	u_R	c_R	t_R	0	$4/3$	$2/3$	0	$1/3$
	d_R	s_R	b_R	0	$-2/3$	$-1/3$	0	$1/3$

Table 2.1: Fermions in the Standard Model, with major quantum numbers.

Bosons		T_3	Y	Q
Gauge	γ	0	0	0
Bosons	Z	0	0	0
	W^+	1	0	1
	W^-	-1	0	-1
	g_i (i=1-8)	0	0	0
Higgs	$\Phi = \begin{pmatrix}\phi^+\\ \phi^0\end{pmatrix}$	$1/2$	1	1
		$-1/2$	1	0

Table 2.2: Bosons in the Standard Model, with major quantum numbers.

In principle, the fermion mass eigenstates are not identical with their weak interaction eigenstates. The two sets of eigenstates of the three fermion families are related by a linear transformation. In the quark sector, it is expressed by a 3×3 matrix, called the Cabibbo-Kobayashi-Maskawa (CKM) matrix [1, 2]:

$$\begin{pmatrix} d' \\ s' \\ b' \end{pmatrix} = \begin{pmatrix} V_{ud} & V_{us} & V_{ub} \\ V_{cd} & V_{cs} & V_{cb} \\ V_{td} & V_{ts} & V_{tb} \end{pmatrix} \begin{pmatrix} d \\ s \\ b \end{pmatrix}, \tag{2.1}$$

in which $(d\ s\ b)$ are the mass eigenstates of the down type quarks, and $(d'\ s'\ b')$ are their weak eigenstates. Equation 2.1 states that the weak eigenstates of the quarks are obtained by mixing their mass eigenstates. A similar story should happen to the lepton sector as well. However, since the masses of the neutrinos are assumed to be 0 [1] in the Standard Model, any mixing of the neutrino mass eigenstates is still their mass eigenstates.

Among the gauge bosons, γ mediates the electromagnetic interaction, and Z^0 and $W^{\pm}$ particles together mediate the weak interaction, while gluons (g_i, i = 1 - 8) mediate the strong interaction. All fermions interact with each other through the exchange of gauge bosons.

2.1.1 Electroweak interaction and Spontaneous Symmetry Breaking [4, 5]

By introducing covariant derivatives, the fermionic terms in the SM electroweak Lagrangian read

$$\mathcal{L}_f = \sum_{\psi} \bar{\psi} i \gamma^{\mu} \mathcal{D}_{\mu} \psi, \tag{2.2}$$

in which

$$\mathcal{D}_{\mu} = \partial_{\mu} \ + \ i g_1 \frac{1}{2} B_{\mu} \cdot Y \ + \ i g_2 W_{\mu} \cdot T, \tag{2.3}$$

where g_1 and g_2 are $U(1)_Y$ and $SU(2)_L$ coupling constants, and the sum of ψ runs through all lepton and quark flavors. This Lagrangian is invariant under local $SU(2)_L \times U(1)_Y$ transformations. By rotating the gauge boson fields to a physical basis, we have

$$\begin{aligned} \mathcal{L}_f = & \sum_{\psi} \bar{\psi} i \gamma^{\mu} \partial_{\mu} \psi \ - \ e \sum_{\psi} Q_{\psi} \bar{\psi} \gamma^{\mu} \psi A_{\mu} \\ & - \ \frac{g^2}{2 cos\theta_W} \sum_{\psi} \bar{\psi} \gamma^{\mu} (g_v \ - \ g_A \gamma_5) \psi Z_{\mu} \\ & - \ \frac{g^2}{\sqrt{2}} \sum_{\psi} \bar{\psi}_L \gamma^{\mu} (\sigma_+ W_{\mu}^+ \ + \ \sigma_- W_{\mu}^-) \psi_L, \end{aligned} \tag{2.4}$$

in which $\sigma_{\pm} = \frac{1}{2}(\sigma_1 \pm i\sigma_2)$. The first term is the free fermion term, the second describes the electromagnetic interaction, and the third term is the weak neutral current interaction, while the last term is the weak charged current term. In this formula, the physical gauge bosons are obtained through mixtures of the "bare" gauge boson fields:

$$\begin{aligned} A_{\mu} &= sin\ \theta_W W_{\mu}^3 \ + \ cos\ \theta_W B_{\mu} \\ Z_{\mu} &= cos\ \theta_W W_{\mu}^3 \ - \ sin\ \theta_W B_{\mu} \\ W_{\mu}^{\pm} &= \frac{1}{\sqrt{2}} (W_{\mu}^1 \ \mp \ i W_{\mu}^2) \end{aligned} \tag{2.5}$$

---

[1] Evidence for oscillation of atmospheric neutrinos was observed recently by the Super-Kamiokande collaboration, which suggests nonzero neutrino masses [3]. If it is confirmed, mixing in the lepton sector also should be taken into account in the Standard Model.

with the weak mixing angle $cos\theta_W = g_2/\sqrt{g_1^2 + g_2^2}$. The total electroweak Lagrangian also contains the gauge boson kinetic terms as well as self-interaction terms,

$$\mathcal{L}_b = -\frac{1}{4}W^i_{\mu\nu}W^{i\mu\nu} - \frac{1}{4}B_{\mu\nu}B^{\mu\nu}, \tag{2.6}$$

in which the field tensors are defined as

$$\begin{aligned} W^i_{\mu\nu} &= \partial_\mu W^i_\nu - \partial_\nu W^i_\mu + g_2\epsilon^{ijk}W^j_\mu W^k_\nu \\ B_{\mu\nu} &= \partial_\mu B_\nu - \partial_\nu B_\mu \end{aligned} \tag{2.7}$$

with ϵ^{ijk} the antisymmetric Levi-Civita tensor.

The SM electroweak Lagrangian shown above describes massless particles, while the physical particles we observe are mostly massive. Since gauge invariance prohibits terms such as $m\bar{\psi}\psi$, we can not add particles mass terms directly into the Lagrangian. This problem is solved by the Higgs mechanism [6], in which the electroweak gauge symmetry is spontaneously broken.

In the SM, the simplest choice of the Higgs field is a complex doublet,

$$\phi = \begin{pmatrix} \phi^+ \\ \phi^0 \end{pmatrix}. \tag{2.8}$$

The key point here is that this Higgs field has a non-trivial scalar potential in the Lagrangian,

$$\begin{aligned} \mathcal{L}_{Higgs} &= (\mathcal{D}_\mu\phi)^\dagger(\mathcal{D}^\mu\phi) - V(\phi) \\ V(\phi) &= \mu^2\phi^\dagger\phi + \lambda(\phi^\dagger\phi)^2, \end{aligned} \tag{2.9}$$

in which $\lambda > 0$ is required by the stability of the theory, and we artificially choose $\mu^2 < 0$ so that the Higgs field has non-vanishing vacuum expectation value,

$$\phi^\dagger\phi = -\frac{\mu^2}{2\lambda} = \frac{v^2}{2} \tag{2.10}$$

with v the vacuum expectation value. Without losing generality, we can choose the vacuum state to be

$$\phi = \frac{1}{\sqrt{2}}\begin{pmatrix} 0 \\ v \end{pmatrix} \tag{2.11}$$

and express the excitation around the ground state as

$$\phi = \frac{1}{\sqrt{2}}\begin{pmatrix} 0 \\ v + H \end{pmatrix}, \tag{2.12}$$

where H is the Higgs boson scalar field. However, such a choice, although it doesn't matter which choice indeed, loses the symmetry of the original $V(\phi)$ and $\mathcal{L}_{Higgs}$. The mass terms of the gauge bosons and the Higgs boson are then generated from $\mathcal{L}_{Higgs}$,

$$\begin{aligned}\mathcal{L}_{Higgs} &= \frac{g_2^2}{4}W^{-\mu}W_\mu^+(v+H)^2 \;+\; \frac{1}{8}(g_2W^{3\mu}-g_1B^\mu)(g_2W_\mu^3-g_1B_\mu)(v+H)^2 \\ &\quad+\; \frac{1}{2}(\partial^\mu H)(\partial_\mu H) \;-\; \frac{\mu^2}{2}(v+H)^2 \;-\; \frac{\lambda}{4}(v+H)^4 \\ &= \frac{1}{2}(\frac{g_2^2v^2}{4})(W_\mu^+W^{-\mu}+W_\mu^-W^{+\mu}) \;+\; \frac{1}{2}(\frac{(g_1^2+g_2^2)v^2}{4}Z_\mu Z^\mu) \;+\; \frac{1}{2}(2\mu^2H^2) \;+\; \cdots\end{aligned} \tag{2.13}$$

from which we can read off the boson masses directly,

$$\begin{aligned}M_W &= \frac{g_2v}{2} \\ M_Z &= \frac{v}{2}\sqrt{g_1^2+g_2^2} \\ M_\gamma &= 0 \\ M_H &= \sqrt{2}\mu.\end{aligned} \tag{2.14}$$

The fermion masses are generated through Yukawa couplings with the Higgs boson with the form

$$G_f[(\bar{\psi}_L\phi)\psi_R \;+\; \bar{\psi}_R(\phi^\dagger\psi_L)] \tag{2.15}$$

and this gives the fermion mass,

$$M_f \;=\; \frac{G_fv}{\sqrt{2}}. \tag{2.16}$$

So the coupling between fermion and the Higgs boson is proportional to the fermion mass.

The Higgs mechanism introduced above is the minimal choice, since we can have additional doublets or larger multiplets. This choice of the Higgs sector, called the Minimal Standard Model (MSM), has been proven to be renormalizable [7].

2.1.2 Quantum Chromodynamics

The strong interaction is also described by a non-Abelian gauge theory named Quantum Chromodynamics (QCD). The symmetry group of this theory is $SU(3)_C$, and the gauge bosons associated with this interaction are gluons carrying "color" quantum number, g_α, with $\alpha \;=\; 1,...,8$.

In analogy to electroweak theory, the covariant derivative in QCD has the form

$$\mathcal{D}_\mu \;=\; \partial_\mu \;-\; ig_3(\frac{\lambda_\alpha}{2})A_\mu^\alpha, \tag{2.17}$$

in which g_3 is the strong coupling constant and A_μ^α are the gluon fields. As in electroweak theory, the quark-gluon interactions are contained in the following terms of the QCD Lagrangian,

$$\mathcal{L}_q \;=\; \sum_q \bar{q}i\gamma^\mu\mathcal{D}_\mu q, \tag{2.18}$$

in which the sum of q runs through all quark fields. In addition, the QCD Lagrangian also contains the kinetic term for the gluon fields which describes the gluon self-interaction,

$$\mathcal{L}_g = -\frac{1}{4} F^{\alpha}_{\mu\nu} F^{\mu\nu}_{\alpha} \tag{2.19}$$

with the gluon field tensor defined as

$$F^{\alpha}_{\mu\nu} = \partial_\mu A^{\alpha}_{\nu} - \partial_\nu A^{\alpha}_{\mu} + g_3 f^{\alpha\beta\gamma} A_{\mu\beta} A_{\nu\gamma}, \tag{2.20}$$

where $f^{\alpha\beta\gamma}$ are the structure constants. So we can see that gluon fields have three- and four-gluon vertexes, meaning that point-like gluon-gluon interactions are allowed.

2.1.3 Tests of the Standard Model and Remaining Open Questions

The Standard Model, in particular the electroweak theory, has been tested experimentally with extreme accuracy. Some of the most recent results obtained at LEP are listed below as an example [8, 9, 10]:

$$\begin{aligned} M_Z &= 91187.5\ (2.1)\ MeV \\ \Gamma_Z &= 2495.2\ (2.3)\ MeV \\ M_W &= 80450\ (39)\ MeV \\ \Gamma_W &= 2150\ (91)\ MeV \\ N_\nu &= 2.9841\ (83) \end{aligned} \tag{2.21}$$

Triple Gauge Couplings:

$$\begin{aligned} g_1^Z &= 0.990^{+0.023}_{-0.024} \quad (SM: 1) \\ \kappa_\gamma &= 0.896^{+0.058}_{-0.056} \quad (SM: 1) \\ \lambda_\gamma &= -0.023^{+0.025}_{-0.023} \quad (SM: 0) \end{aligned} \tag{2.22}$$

However, there are still many open questions for the Standard Model. Some of them make us believe that the SM cannot be the ultimate theory. We list here some of the major concerns about the Standard Model:

- The SM does not incorporate gravity. Although gravity is always negligible in particle interactions at current energy scales due to its extremely small coupling constant, we have to consider its effect at very high energies near the Planck scale ($\simeq 10^{19}\ GeV$) where gravity has comparable strength with the other interactions. And a grand unified theory including gravity is always desirable.

- The Standard Model depends on eighteen free parameters[2]. One can assume that a “final” theory should not have so many free parameters. We expect a grand unified theory to include relations between the gauge couplings, and perhaps also among the fermion masses and boson masses.

- The hierarchy problem. Although the Higgs mechanism solved the particle mass problem, it turns out that when a large energy scale is involved (for example, to embed the Standard Model in a grand unification theory), the mass of the Higgs boson is always calculated from an algebraic sum of extremely large positive and negative quantities. To keep the electroweak scale as low as we observe, we need a rather small Higgs mass, and hence a ‘fine-tuning’ of the theory parameters. This is rather suspicious. The hierachy problem is discussed in more detail in Appendix A.

Despite the great success of the Standard Model, people are still searching for a theory beyond it.

2.2 Supersymmetry

Supersymmetry is a subject of considerable interest among physicists and mathematicians, not only because of its nice features such as solving the hierarchy problem which is inevitable for almost any extension of the Standard Model, but also due to some fundamental concerns. An important result of Haag, Sohnius and Lopuszanski states that the supersymmetry algebra is the only graded Lie algebra[3] of symmetries of the S-matrix consistent with relativistic quantum field theory [11].

2.2.1 Supermultiplets and particle content of MSSM [12]

Supersymmetry is a symmetry relating fermions and bosons. A supersymmetry transformation turns a bosonic state into a fermionic state, and vice versa. The operator Q which generates such a transformation must be an anti-commuting spinor, with

$$Q|Boson\rangle = |Fermion\rangle; \qquad Q|Fermion\rangle = |Boson\rangle \tag{2.23}$$

---

[2] One of the choices of these parameters is: the QED coupling constant α, M_Z, M_W, M_H, the masses of the charged leptons, the masses of the quarks, the strong coupling constant α_s, the three mixing angles and a phase in the CKM matrix.

[3] Graded Lie algebra (or superalgebra) is an algebraic system whose defining relations involve anticommutators as well as commutators [11].

The supersymmetry generators Q and $Q^\dagger$ must satisfy an algebra of anti-commutation and commutation relations with the form

$$\begin{aligned} \{Q_\alpha, Q^\dagger_{\dot\alpha}\} &= 2\sigma^\mu_{\alpha\dot\alpha} P_\mu \\ \{Q_\alpha, Q_\beta\} &= \{Q^\dagger_{\dot\alpha}, Q^\dagger_{\dot\beta}\} = 0 \\ [Q_\alpha, P_\mu] &= [Q^\dagger_{\dot\alpha}, P_\mu] = 0, \end{aligned} \tag{2.24}$$

in which σ_μ are Pauli matrices, $\alpha, \beta, \dot\alpha, \dot\beta$ = 1,2 and P_μ is the momentum generator of space-time translations. The single-particle states of a supersymmetric theory fall naturally into irreducible representations of the supersymmetry algebra which are called supermultiplets. Each supermultiplet contains both fermion and boson states which are superpartners of each other. Particles that inhabit the same irreducible supermultiplet must have equal masses. Since Q and $Q^\dagger$ commute with the generators of the gauge transformations, particles in the same supermultiplet must also be in the same representation of the gauge group, and thus must have the same electric charges, weak isospin and color degrees of freedom. In each supermultiplet, the number of bosonic degrees of freedom equals the number of fermionic degrees of freedom.

The simplest supermultiplet consists of a single Weyl fermion[4] and two real scalars. This is called chiral[5] (or matter, or scalar) supermultiplet.

The next simplest supermultiplet contains a spin-1 vector boson. If the theory is to be renormalizable, this must be a gauge boson which is massless, at least before the gauge symmetry is spontaneously broken. Its superpartner is therefore a massless spin-1/2 Weyl fermion, called a gaugino. Such a combination of spin-1/2 gauginos and spin-1 gauge bosons is called a gauge (or vector) supermultiplet.

For N = 1 supersymmetry with renormalizable interactions, other representations are always reducible to combinations of chiral and gauge supermultiplets. In a supersymmetric extension of the Standard Model, each of the known fundamental particles must therefore be in either a chiral or gauge supermultiplet and have a superpartner with spin differing by 1/2 unit.

Since only chiral supermultiplets may contain fermions whose left- and right-handed parts transform differently under the gauge group, all Standard Model fermions (quarks and leptons) therefore must be members of chiral supermultiplets. In addition, the Higgs boson must reside in a chiral supermultiplet too, since it has spin 0. However, it turns out that one chiral supermultiplet is not enough; we need at least two, both for triangle gauge anomaly cancellation[6] and for giving mass to up-type quarks as

---

[4] A Weyl fermion is a two-component spinor with definite "handedness"

[5] Chirality is the nature of an object whose left- and right-handed components have distinct properties. A chiral supermultiplet may host fermions whose left- and right-handed parts have different interaction properties.

[6] In a gauge theory in which gauge bosons couple to a chiral current, the triangle diagrams appear in the one-loop

Names		spin 0	spin 1/2	$SU(3)_C, SU(2)_L, U(1)_Y$
squarks, quarks	Q	$(\tilde{u}_L, \tilde{d}_L)$	(u_L, d_L)	$(\mathbf{3}, \mathbf{2}, +1/3)$
(× 3 families)	$\bar{U}$	$\tilde{u}^*_R$	$u^\dagger_R$	$(\bar{\mathbf{3}}, \mathbf{1}, -4/3)$
	$\bar{D}$	$\tilde{d}^*_R$	$d^\dagger_R$	$(\bar{\mathbf{3}}, \mathbf{1}, +2/3)$
sleptons, leptons	L	$(\tilde{\nu}, \tilde{e}_L)$	(ν, e_L)	$(\mathbf{1}, \mathbf{2}, -1)$
(× 3 families)	$\bar{E}$	$\tilde{e}^*_R$	$e^\dagger_R$	$(\mathbf{1}, \mathbf{1}, +2)$
Higgs, higgsinos	H_u	(H_u^+, H_u^0)	$(\tilde{H}_u^+, \tilde{H}_u^0)$	$(\mathbf{1}, \mathbf{2}, +1)$
	H_d	(H_d^0, H_d^-)	$(\tilde{H}_d^0, \tilde{H}_d^-)$	$(\mathbf{1}, \mathbf{2}, -1)$

Table 2.3: Chiral supermultiplets in the Minimal Supersymmetric Standard Model.

Names	spin 1/2	spin 1	$SU(3)_c, SU(2)_L, U(1)_Y$
gluino, gluon	$\tilde{g}$	g	$(\mathbf{8}, \mathbf{1}, 0)$
winos, W bosons	$\tilde{W}^\pm, \tilde{W}^0$	$W^\pm, W^0$	$(\mathbf{1}, \mathbf{3}, 0)$
bino, B boson	$\tilde{B}^0$	B^0	$(\mathbf{1}, \mathbf{1}, 0)$

Table 2.4: Gauge supermultiplets in the Minimal Supersymmetric Standard Model.

well as down-type quarks and charged leptons. The vector bosons of the Standard Model clearly must reside in gauge supermultiplets. Their fermionic superpartners are generally referred to as gauginos. Now we have specified all the chiral and gauge supermultiplets for a minimal phenomenologically viable extension of the Standard Model. The chiral and gauge supermultiplets are summarized in Table 2.3 and Table 2.4, respectively.

---

corrections to the three-gauge-boson vertex function. The anomalous term violates the Ward identity for this amplitude. Thus, such a theory can be gauge invariant only if the anomalous contribution is somehow canceled [13].

2.2.2 MSSM Lagrangian and R-parity

The MSSM Lagrangian can be constructed from the chiral superfields, gauge and gaugino fields, by requiring gauge symmetry and supersymmetry as follows [14, 15],

$$\begin{aligned}\mathcal{L} \;=\; & \sum_i (\mathcal{D}_\mu \mathcal{S}_i)^\dagger (\mathcal{D}^\mu \mathcal{S}_i) \;+\; \frac{i}{2}\sum_i \bar{\psi}_i \gamma^\mu \mathcal{D}_\mu \psi_i \\ & - \frac{1}{4}\sum_A F_{\mu\nu A} F^{\mu\nu}_A \;+\; \frac{i}{2}\sum_A \bar{\lambda}_A \gamma^\mu \mathcal{D}_\mu \lambda_A \\ & - \sqrt{2}\sum_{i,A}\left[\mathcal{S}_i^\dagger (g_\alpha t_{\alpha A}) \bar{\psi}_i \frac{1-\gamma_5}{2}\lambda_A \;+\; h.c.\right] \\ & - \frac{1}{2}\sum_A \left[\sum_i \mathcal{S}_i^\dagger g_\alpha t_{\alpha A} \mathcal{S}_i\right]^2 ,\end{aligned} \tag{2.25}$$

in which $\mathcal{S}_i$ (ψ_i) is the scalar (fermion) component of a chiral superfield, $F_{\mu\nu A}$ is a gauge field, λ_A is a gaugino field, and $t_{\alpha A}$ is the hermitian matrix representation of the interaction gauge group. The first two lines of the Lagrangian describe the particle interactions with gauge bosons and thus contain the SM Lagrangian. The third line gives interactions of gauginos with chiral superfields, and the last line describes quartic couplings of the scalars in chiral superfields.

Given the superfield components, the only freedom one has in constructing the supersymmetric Lagrangian is the superpotential $\mathcal{W}$, which is an analytic function of the chiral superfields $\hat{S} = Q, \bar{U}, \bar{D}, L, \bar{E}, H_u, H_d$. In a renormalizable theory, an $SU(3)_C \times SU(2)_L \times U(1)_Y$ invariant superpotential has the following form (for the first generation):

$$\begin{aligned}\mathcal{W} \;=\; & \epsilon_{ij}\mu H_u^i H_d^j \;+\; \epsilon_{ij}\left[\lambda_L H_d^i L^j \bar{E} \;+\; \lambda_D H_d^i Q^j \bar{D} \;+\; \lambda_U H_u^i Q^j \bar{U}\right] \\ & + \; \epsilon_{ij}\left[\lambda_1 L^i L^j \bar{E} \;+\; \lambda_2 L^i Q^j \bar{D}\right] \;+\; \lambda_3 \bar{U}\bar{D}\bar{D},\end{aligned} \tag{2.26}$$

in which i, j are the $SU(2)_L$ doublet indices and $\epsilon_{ij} = -\epsilon_{ji}$ ($\epsilon_{12} = 1$). In general, the λ coefficients should be matrices which mix the interactions of the 3 generations. The superpotential gives the following terms in the Lagrangian:

$$\mathcal{L}_\mathcal{W} \;=\; -\sum_i \left|\frac{\partial \mathcal{W}}{\partial \hat{S}_i}\right|^2 \;-\; \frac{1}{2}\sum_{i,j}\left\{\bar{\psi}_i \left[\frac{1-\gamma_5}{2}\right]\left(\frac{\partial^2 \mathcal{W}}{\partial \hat{S}_i \partial \hat{S}_j}\right)\psi_j \;+\; h.c.\right\}. \tag{2.27}$$

Both the scalar potential and the Yukawa interactions of fermions with scalars can be found in $\mathcal{L}_\mathcal{W}$. The μ term gives mass terms for the Higgs bosons. The $\lambda_{L,D,U}$ terms give the Yukawa interactions of the fermions with the Higgs bosons. So these coefficients are determined by fermion masses and the Vacuum Expectation Values (VEV's) of the neutral members of the Higgs doublets. Here an additional free parameter with respect to that of the SM appears, which is defined as $\tan\beta = v_2/v_1$, with $v_1 = \langle H_d^0 \rangle$, $v_2 = \langle H_u^0 \rangle$.

The $\lambda_{1,2,3}$ terms result in lepton and baryon number violating interactions. For example, they can mediate proton decay at tree level by exchange of a scalar down quark. Among the many ways to avoid this kind of problem, a usual one is to require an additional symmetry, called R-parity. R-parity is a quantum number that distinguishes SM particles and their SUSY partners, and is defined as

$$R = (-1)^{3(B-L)+2s}, \tag{2.28}$$

in which s is the spin of the particle. So all Standard Model particles have R-parity +1, while their SUSY partners have R-parity −1. Obviously, one removes all the $\lambda_{1,2,3}$ terms by requiring R-parity conservation[7].

The assumption of R-parity conservation has important phenomenological consequences:

- The lightest sparticle, called the lightest supersymmetric particle (LSP), must be absolutely stable. If the LSP is electrically neutral, it interacts only weakly with ordinary matter.
- Each sparticle other than the LSP must eventually decay into a state which contains an odd number of LSPs (usually just one)
- In collider experiments, sparticles can only be produced in even numbers (usually in pairs)

The LSP is an attractive candidate [16] for the non-baryonic cold dark matter that is thought to make up ∼30% of the mass of the observable universe. And in collider experiments, a signal for R-parity conserving SUSY is missing energy from the non-observed LSPs.

2.2.3 Supersymmetry breaking [12]

One important observation is that supersymmetry can not be an exact symmetry of the world, otherwise it becomes extremely easy to discover supersymmetry: all SUSY particles would then have masses degenerate with their SM partners. So a realistic phenomenological model must contain supersymmetry breaking, leading to heavy SUSY particle masses. However, from a theoretical perspective, we expect that supersymmetry should be an exact symmetry which is spontaneously broken.

The exact mechanism of supersymmetry breaking is not clear now, however, we know that for spontaneous supersymmetry breaking it requires us to extend the MSSM. In addition, if we want to have

---

[7] The R-parity conservation requires that the product of R-parity for all the fields of a vertex is +1. We consider $(-1)^{3(B-L)}$ and $(-1)^{2s}$ separately. The product of $(-1)^{2s}$ is +1, due to the angular momentum conservation. And it is easy to check that the quark and lepton supermultiplets all have $(-1)^{3(B-L)} = -1$, while the Higgs and gauge supermultiplets have $(-1)^{3(B-L)} = +1$, therefore the $\lambda_{1,2,3}$ terms violate R-parity.

a phenomenologically viable theory, it seems that supersymmetry breaking occurs in a "hidden sector" of particles which have no (or only very small) direct couplings to the "visible sector" chiral supermultiplets of the MSSM. However, the two sectors do share some interactions to mediate supersymmetry breaking from the hidden sector to the visible sector, which appear as calculable soft terms in the effective Lagrangian.

There are two main proposals for what the mediating interactions might be. The first is that they are gravitational. In this gravity-mediated supersymmetry breaking scenario (often referred as SUGRA), the energy scale of SUSY breaking in the hidden sector should be roughly 10^{10} or 10^{11} GeV, and the spin-3/2 gravitino has a mass of the order of electroweak scale. The second main possibility is that the flavor-blind mediating interactions for supersymmetry breaking are the ordinary electroweak and QCD gauge interactions. In this gauge-mediated supersymmetry breaking (GMSB) scenario, the MSSM soft terms arise from loop diagrams involving some messenger particles [8], and the SUSY breaking scale is much lower, around 10^4 or 10^5 GeV. In addition, the gravitino has a mass of order eV to KeV, and is therefore the LSP. The two models have very different phenomenological consequences.

From a practical point of view, we usually directly introduce extra soft terms which break supersymmetry explicitly in the effective MSSM Lagrangian,

$$\mathcal{L} \;=\; \mathcal{L}_{SUSY} \;+\; \mathcal{L}_{soft}. \tag{2.29}$$

The possible soft operators for the MSSM are: mass terms for scalar members of the chiral multiplets and gaugino members of the gauge supermultiplets, bi-linear mixing terms ("B" terms) and trilinear scalar mixing terms ("A" terms). So the soft terms are given by (for the first generation) [15, 18],

$$\begin{aligned}
-\mathcal{L}_{soft}^{MSSM} \;=\; & m_1^2|H_d|^2 \;+\; m_2^2|H_u|^2 \;-\; B\mu\epsilon_{ij}(H_d^i H_u^j + h.c.) \\
& + \; M_Q^2\bar{Q}^i Q^i \;+\; M_U^2\bar{U}U \;+\; M_D^2\bar{D}D + \; M_L^2\bar{L}^i L^i \;+\; M_E^2\bar{E}E \\
& + \; \frac{1}{2}\left[M_1\bar{\tilde{B}}^0\tilde{B}^0 \;+\; M_2\bar{\tilde{W}}^a\tilde{W}^a \;+\; M_2\bar{\tilde{g}}\tilde{g}\right] \\
& + \; \frac{g_2\epsilon_{ij}}{\sqrt{2}M_W}\left[\frac{m_d}{cos\beta}A_d H_d^i Q^j \tilde{d}_R^* \;+\; \frac{m_u}{sin\beta}A_u H_u^j Q^i \tilde{u}_R^* \;+\; \frac{m_e}{cos\beta}A_e H_d^i L^j \tilde{e}_R^* \;+\; h.c.\right],
\end{aligned} \tag{2.30}$$

in which i,j are the $SU(2)_L$ doublet indices. The scalar and gaugino mass terms have the desired effect of breaking the mass degeneracy between SM particles and their SUSY partners. The tri-linear A-terms affect primarily the particles of the third generation. The $B\mu$ term mixes the scalar components of the

---

[8] The messengers couple to a supersymmetry-breaking VEV $\langle F \rangle$, and also have $SU(3)_C \times SU(2)_L \times U(1)_Y$ interactions which provide a link to the MSSM [12]. The messenger sector is formed by some new superfields and it is the main source of model dependence [17].

two Higgs doublets. In general, all the mass and interaction terms should be matrices for all three generations.

Unlike the supersymmetry-preserving part of the Lagrangian, $\mathcal{L}_{soft}^{MSSM}$ introduces many new parameters which were not present in the SM. A careful count [19] reveals that there are 105 masses, phases and mixing angles in the MSSM Lagrangian which has no counterpart in Standard Model. Among them, 104 are from $\mathcal{L}_{soft}^{MSSM}$, and only one, tan$\beta$, is from $\mathcal{L}_{SUSY}$.

2.2.4 Constrained MSSM

In the general form of the MSSM with R-parity conservation, one expects that most of the 105 extra free parameters should be related. Currently we have several experimental hints that suggest how to reduce the total number of parameters. One of them is the behavior of the gauge coupling constants. The evolution of the coupling constants with energy is sensitive to the particle content of the theory. Evolving the measured coupling constants within the framework of Standard Model, there is no apparent unification at a single point at high energy. However, if we do this in SUSY theory with particle masses at the electroweak scale, then the constants meet at roughly 10^{16} GeV, as shown in Figure 2.1 [12]. In addition, we usually assume the gaugino masses also unify at M_{GUT}, with $M_1(M_{GUT}) = M_2(M_{GUT}) = M_3(M_{GUT}) = m_{1/2}$. Their mass at the electroweak scale is given by the renormalization group (RG)

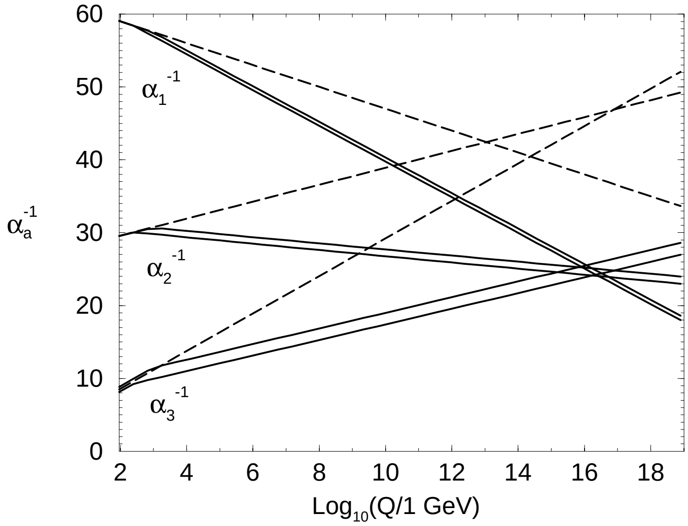

Figure 2.1: RG evolution of the inverse gauge couplings $\alpha_a^{-1}(Q)$ in the Standard Model (dashed lines) and in the MSSM (solid lines) [12].

equations[9] [20],

$$\frac{3M_1}{5g_1^2} \;=\; \frac{M_2}{g_2^2} \;=\; \frac{M_3}{g_3^2}, \quad M_2 \;=\; 0.82m_{1/2} \tag{2.31}$$

To avoid lepton number violation, the slepton mass matrices $\tilde{M}_L$, $\tilde{M}_E$ should be flavor diagonal. Constraints on Flavor Changing Neutral Currents (FCNC) suggest that the squark mass matrices and trilinear couplings are also flavor diagonal [21]. We also assume that all squarks and sleptons have the same mass at the GUT scale, and the same trilinear couplings:

$$M_Q^2(M_{GUT}) \;=\; M_D^2(M_{GUT}) \;=\; M_U^2(M_{GUT}) \;=\; M_L^2(M_{GUT}) \;=\; M_E^2(M_{GUT}) \;=\; m_0^2 \tag{2.32}$$

$$A_d(M_{GUT}) \;=\; A_u(M_{GUT}) \;=\; A_e(M_{GUT}) \;=\; A_0 \tag{2.33}$$

The MSSM with all these assumptions is called the constrained MSSM (CMSSM) [22], and we are left with only 6 parameters:

- M_2: the $SU(2)_L$ gaugino mass at the electroweak scale
- m_0: the universal scalar mass at the GUT scale
- A_0: the universal trilinear coupling at the GUT scale
- tanβ: the ratio of VEV's of the two Higgs doublets
- μ: the higgsino mass parameter at the electroweak scale
- M_A: the mass of the CP-odd Higgs boson.

The CMSSM is highly predictive: once the 6 parameters are set, the sparticle spectrum can be calculated at the electroweak scale by the RG equations. The SUSY interpretation of this analysis is carried out in the framework of the CMSSM.

2.2.5 Neutralinos and charginos [12]

The higgsinos and electroweak gauginos mix with each other because of the effects of electroweak symmetry breaking. The neutral higgsinos ($\tilde{H}_u^0$ and $\tilde{H}_d^0$) and the neutral gauginos ($\tilde{B}$, $\tilde{W}^0$) combine to form four neutral mass eigenstates: $\tilde{\chi}_1^0$, $\tilde{\chi}_2^0$, $\tilde{\chi}_3^0$, $\tilde{\chi}_4^0$, in order of increasing mass, called neutralinos.

The charged higgsinos ($\tilde{H}_u^+$ and $\tilde{H}_d^-$) and the winos ($\tilde{W}^+$ and $\tilde{W}^-$) mix to form two mass eigenstates with charge ±1: $\tilde{\chi}_1^\pm$, $\tilde{\chi}_2^\pm$, in order of increasing mass, called charginos.

---

[9] The parameters of a renormalizable field theory are scale-dependent entities. And renormalization group equations are simple differential equations that describe this scale dependence. [13]

The lightest neutralino, $\tilde{\chi}_1^0$, is usually assumed to be the LSP, unless there is a lighter gravitino or unless R-parity is not conserved, because it is the only MSSM particle which can make a good cold dark matter candidate.

2.3 Scalar leptons

Whether in gravity mediated SUSY breaking models or in gauge mediated SUSY breaking models, scalar leptons are always listed as one of the most probable SUSY particles to be found at this generation of collider experiments, due to their relatively light masses and/or distinctive signatures involving final-state leptons. The analysis described in this thesis is focused on the search for scalar leptons. We will discuss here the phenomenology issues relevant to SUSY scalar leptons.

2.3.1 Fermion mass and mixing

The physical masses of SUSY fermions at the electroweak scale are determined from their masses at the GUT energy scale by using the RG equations. There are three contributions to the running of sfermion masses: the gaugino coupling, the Yukawa coupling and the trilinear interactions.

The gaugino contribution to the sfermion mass-squared parameter, M_F^2, remains positive as the energy scale evolves downward. The squarks become considerably heavier than the sleptons as they have contributions proportional to the strong coupling constant from the gluino loops.

The Yukawa and trilinear contributions, which are negligible for the first two generations, significantly modify the mass running of the third generation sfermion. Their contributions always decrease the masses when evolving to lower energy scale. Since the Yukawa coupling for stop (the top SUSY partner) is very large due to its large mass, the mass parameter for stop decreases most.

In principle, sfermions of the same electric charge and color quantum numbers mix with each other. The mass eigenstates are obtained by diagonalizing 6×6 mass-square matrices, one for each: up type squarks, down type squarks and sleptons. To avoid large Flavor Changing Neutral Currents (FCNC), we can assume that these matrices are block diagonal and can be decomposed into 2×2 matrices. As an example, the mass-square matrices for charged sleptons are

$$\mathcal{M}_{\tilde{l}}^2 = \begin{pmatrix} m_{\tilde{l}_L}^2 & a_l m_l \\ a_l m_l & m_{\tilde{l}_R}^2 \end{pmatrix} \tag{2.34}$$

with

$$\begin{aligned} m^2_{\tilde{l}_L} &= M^2_{\tilde{L}} + m^2_Z \cos 2\beta\ (I^3_l - Q_l \sin^2\theta_W) + m^2_l \\ m^2_{\tilde{l}_R} &= M^2_{\tilde{L}} + Q_l\, m^2_Z \cos 2\beta \sin^2\theta_W + m^2_l \\ a_l &= A_l - \mu\ (\tan\beta)^{-2I^3_l}. \end{aligned} \tag{2.35}$$

So the slepton masses are determined by the soft SUSY masses $M_{\tilde{L}}$ at the electroweak scale, A_l, μ and tanβ. The left- and right-handed sfermions will mix due to the off-diagonal terms, and this mixing is proportional to the corresponding SM lepton masses – we can safely neglect the mixing of $\tilde{e}$ and $\tilde{\mu}$, but not for $\tilde{\tau}$. These results also apply to squarks.

The transformation between mass and weak eigenstates of sleptons is usually expressed by a mixing angle:

$$\begin{pmatrix} \tilde{l}_1 \\ \tilde{l}_2 \end{pmatrix} = \begin{pmatrix} \cos\theta_{LR} & \sin\theta_{LR} \\ -\sin\theta_{LR} & \cos\theta_{LR} \end{pmatrix} \begin{pmatrix} \tilde{l}_L \\ \tilde{l}_R \end{pmatrix} \tag{2.36}$$

with

$$\cos\theta_{LR} = \frac{-a_l m_l}{\sqrt{(m^2_{\tilde{l}_L} - m^2_{\tilde{l}_1})^2 + a^2_l m^2_l}} \tag{2.37}$$

and the mass eigenvalues are

$$m^2_{\tilde{l}_{1,2}} = \frac{1}{2}(m^2_{\tilde{l}_L} + m^2_{\tilde{l}_R} \mp \sqrt{(m^2_{\tilde{l}_L} - m^2_{\tilde{l}_R})^2 + 4a^2_l m^2_l}), \tag{2.38}$$

in which $\tilde{l}_1$ is always the lightest eigenstate. At high tanβ, $\tilde{\tau}_L$ and $\tilde{\tau}_R$ are strongly mixed and give a large mass splitting between the two mass eigenstates, $\tilde{\tau}_1$ and $\tilde{\tau}_2$. A similar result also applies to $\tilde{b}$ and $\tilde{t}$. So $\tilde{\tau}_1$, and maybe also $\tilde{b}_1$ and $\tilde{t}_1$, are likely to be the lightest detectable SUSY particles.

2.3.2 Scalar lepton in SUGRA

In SUGRA models, the possible SUSY particles that may be detected at LEP are sleptons, third generation squarks, the lightest charginos, and the next to lightest neutralinos. And the LSP is assumed to be the lightest neutralino, $\tilde{\chi}^0_1$.

Scalar leptons can be produced in pair in e^+e^- collisions through s-channel γ/Z exchange, while for scalar electrons, its production cross section is enhanced by t-channel $\tilde{\chi}^0_1$ exchange and thus its cross section depends on the $\tilde{\chi}^0_1$ mass. Figure 2.2 shows the diagrams of slepton production processes. Figure 2.3 shows the production cross section as a function of the slepton mass, at $\sqrt{s} = 189$ GeV.

Assuming R-parity conservation, scalar leptons always have very short lifetimes in this scenario. The scalar lepton decays into its partner lepton mainly via $\tilde{l}^\pm \to \tilde{\chi}^0_1 l^\pm$, but also via cascade decays, such as $\tilde{l}^\pm \to \tilde{\chi}^0_2 l^\pm \to \tilde{\chi}^0_1 Z^* l^\pm$, which may be important in some regions of the parameter space.

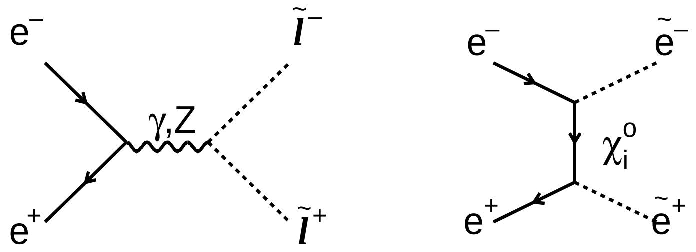

Figure 2.2: The Feynman diagrams for slepton production processes.

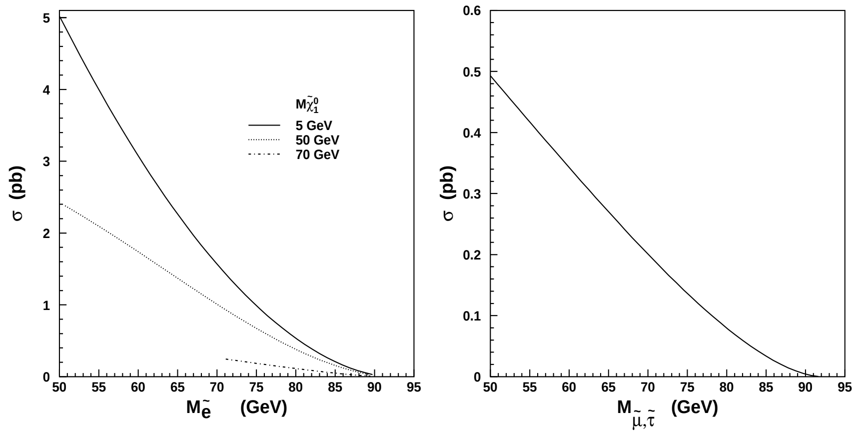

Figure 2.3: The production cross section of the sleptons, as a function of the slepton mass, at $\sqrt{s} = 189\ GeV$. The cross section of the selectron depends on the mass of the LSP, due to the t-channel contribution.

Due to the stable, weakly interacting LSP, the slepton signature is very clear: two acoplanar leptons of the same flavor with large missing energy. However, this clear and simple final state suffers from irreducible SM background processes such as 2-photon collisions and W-pair production.

2.3.3 Scalar lepton in GMSB

In GMSB models, supersymmetry breaking takes place at a rather low scale $\sqrt{F}$, which leads to a light gravitino:

$$m_{\tilde{G}} = \frac{F}{\sqrt{3}M_P} \simeq 2.5\ eV(\frac{\sqrt{F}}{100\ TeV})^2, \tag{2.39}$$

which has a mass of order eV to KeV. So the gravitino is generally the Lightest Supersymmetric Particle (LSP). In GMSB models with a Next to Lightest Supersymmetric Particle (NLSP) lighter than $\sim$ 100 GeV, i.e., accessible at LEP2, the NLSP is always a neutralino or a stau throughout the parameter space [23]. However in the stau NLSP case, it is possible that $\tilde{e}_R$ and $\tilde{\mu}_R$ are almost mass degenerate with $\tilde{\tau}_1$, and act as "co-NLSPs." Assuming that R-parity is conserved, the scalar leptons (when they are NLSP or co-NLSP) decay into their corresponding lepton and a gravitino, $\tilde{l} \rightarrow l\tilde{G}$. Depending on the mass of the gravitino, the decay length of the NLSP is given by

$$L_{NLSP} = 1.76 \times 10^{-3}\sqrt{(\frac{E_{NLSP}}{m_{NLSP}})^2 - 1}\,(\frac{m_{NLSP}}{100\ GeV/c^2})^{-5}(\frac{m_{\tilde{G}}}{1\ eV/c^2})^2\ cm. \qquad (2.40)$$

Given the scale of $m_{\tilde{G}}$, the decay length of the NLSP could vary from being undetectable, to longer than the radius of any LEP detector.

In GMSB models, scalar leptons can be pair-produced in e^+e^- collisions through s-channel γ/Z exchange, and t-channel $\tilde{\chi}_1^0$ exchange enhances the scalar electron production. However, since the scalar τ is always the lightest of the three scalar lepton flavors, we only search for the scalar tau NLSP in this analysis, and we also cover the co-NLSP case. This analysis covers the entire stau lifetime range, and we can expect a lifetime independent mass limit from it. One can also foresee that for rather long stau lifetimes, we should be very careful about the background from cosmic rays. The neutralino NLSP case is covered by a separate analysis, focused on single and multi-photon events.

3. LEP and the L3 Detector

This analysis is based on the data collected by the L3 detector at the LEP (Large Electron-Positron) storage ring. The LEP program has been very successful both from the accelerator point of view and the detector and physics point of view. This chapter gives a brief overview of LEP and the L3 detector, with emphasis on those aspects that are important for SUSY searches.

3.1 LEP accelerator

LEP is a large electron-positron collider operated by the European Laboratory for Particle Physics (CERN), located near Geneva, Switzerland (Figure 3.1).

The early development of LEP started in the 70's. In the Annual Reports to the CERN Council in 1979 and 1980, it said, "After many years of studies of different types of machines ... the choice of the European community settled ... on a very large electron-positron collider called LEP. ... The basic feature of the present LEP design is a large machine circumference in which the machine will be installed in stages corresponding to the new physics events that are predicted by the unified theory of weak and electromagnetic interactions. The first predicted event is the ... Z^0 at an energy of 90 GeV. Since these bosons can be produced singly, the LEP machine energy is about 50 GeV per beam ... The next predicted event is the production of pairs of the charged intermediate boson — W^+W^- pairs — at an energy of about 180 GeV which requires LEP energies of about 90 GeV per beam. ... To explore the Z^0 region, only a part of the RF accelerating cavities and their power amplifiers will be installed in the machine. To reach the next energy stage one has the choice either to install the full set of copper RF accelerating cavities or to install superconducting cavities, if they are ready at that time. ... the latest development of the LEP Project is to use the PS and SPS machines as the injectors for LEP ... "

Finally, LEP was built into a Main Ring tunnel of 26.67 km circumference, and consists of eight straight and eight curved sections. The former hosts the four LEP experiments, ALEPH [24], DELPHI [25], L3 [26] and OPAL [27], as well as the RF accelerating cavities, while the latter hosts dipole bending magnets, quadrupole and sextupole focusing magnets. The plane of the LEP tunnel is inclined by 1.4%, to ensure that all underground caverns and the main part of the tunnel would be located in solid rock while, at the same time, limiting the maximum depth of the shafts to less than 150 m (see Figure 3.2).

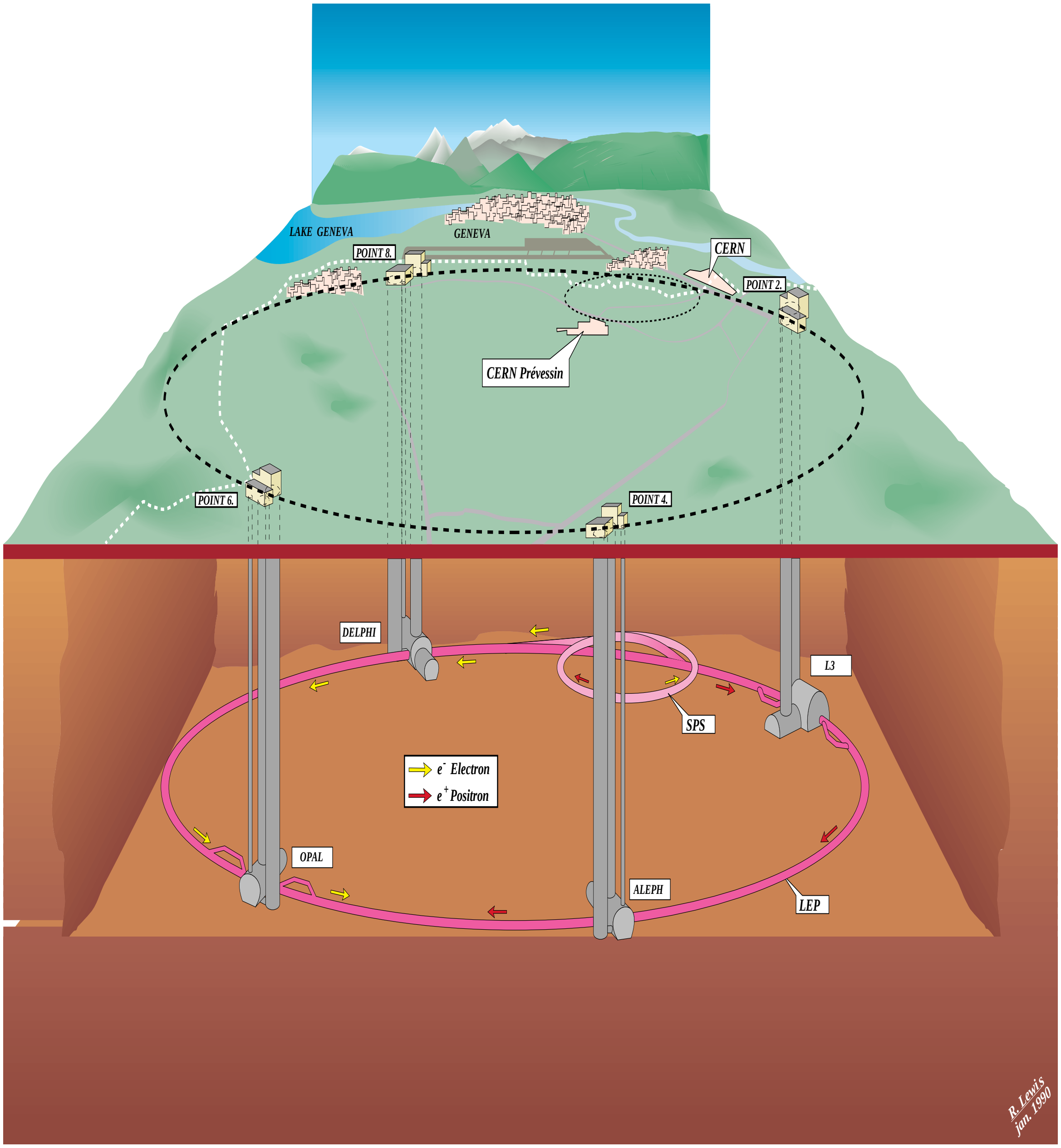

Figure 3.1: 3-D schematic view of LEP accelerator, Super Proton Synchrotron (SPS), four LEP experiments, and the surrounding Geneva area. The varying depths of the experiments below the ground, from 50 m for L3 to 150 m for ALEPH, are not shown in this sketch.

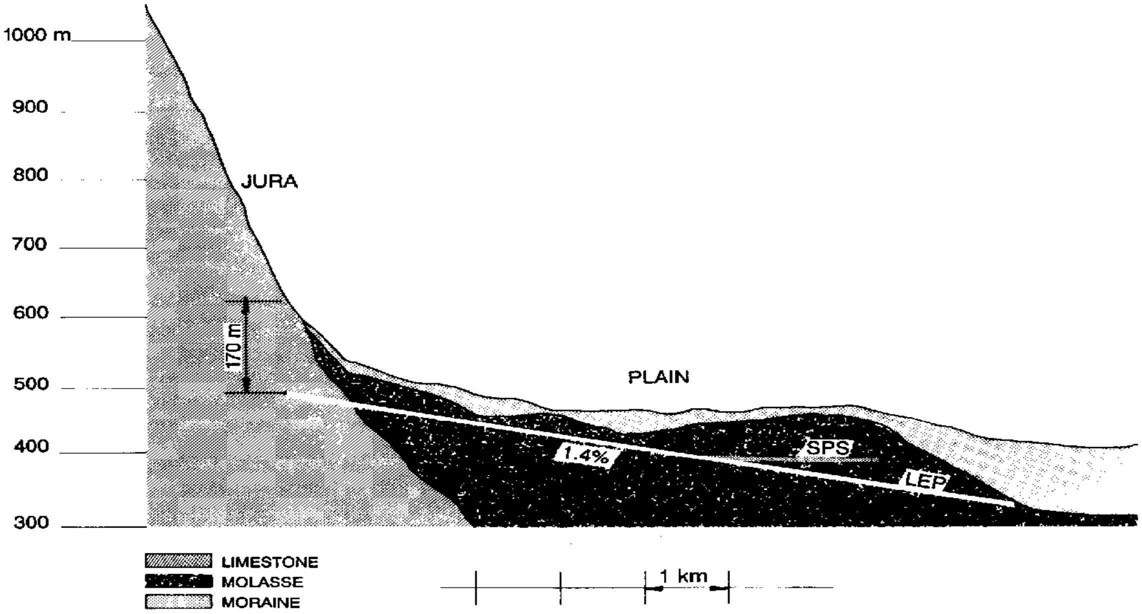

Figure 3.2: Inclined plane of the LEP tunnel.

3.1.1 Injectors and pre-injectors [28]

The LEP storage ring was the last accelerator in a chain of five (see Figure 3.3). The LEP injectors consisted of two linacs of 200 MeV and 600 MeV followed by a 600 MeV Electron-Positron Accumulator (EPA), which injected into the CERN Proton Synchrotron (PS) operating as a 3.5 GeV e^+e^- synchrotron. The PS then injected into the CERN Super Proton Synchrotron (SPS), which operated as a 20 GeV electron-positron injector for LEP. The decision to use the two already existing CERN proton synchrotrons (the SPS and the PS) and all the infrastructure associated with them resulted in significant economies both in cost and in time.

In order to serve LEP, both the PS and the SPS operated in multicycle mode. In this mode, a supercycle was used which incorporated four cycles of electrons or positrons, followed by one cycle of protons. Due to the fact that the electrons or positrons were accelerated in the dead-time between the proton cycles, the filling of LEP had little or no effect on the 450 GeV SPS fixed target physics program, which ran in parallel.

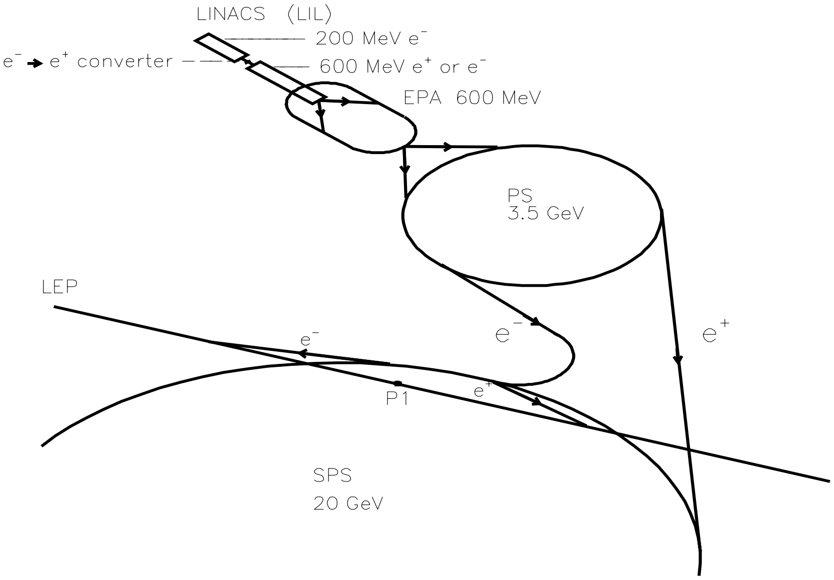

Figure 3.3: LEP injectors and pre-injectors.

3.1.2 LEP energy and RF power upgrade

The maximum possible beam energy in LEP depends on the energy loss of electrons/positrons per turn and the available RF voltage to restore this loss. The radiative energy loss per turn U_0 is a steep function of the beam energy E [29, 30]:

$$U_0[eV] \approx 8.85 \times 10^4 \frac{E^4[GeV]}{\rho[m]} = 28.5 \times E^4[GeV]. \tag{3.1}$$

Here, an iso-magnetic lattice is assumed and ρ denotes the average bending radius of the ring collider ($\sim 3100\,m$ for LEP). On the other hand, to obtain a finite quantum lifetime τ_q, an overvoltage is needed to maintain a bucket size large enough to allow quantum excitations [31]. The required RF voltage per turn in LEP is shown as a function of the beam energy in Figure 3.4.

The LEP RF system originally consisted of 128 copper cavities organized in 8 RF units of 16 cavities per unit, where each cavity provided 2.5 MV of accelerating voltage. This setup enabled LEP to run at the peak of the Z resonance until 1995. By October 1995, in addition to the copper cavities, a total of 64 superconducting (SC) cavities[1] were operational, allowing an increase in beam energy from 45 GeV to 70 GeV. The first 16 SC cavities were constructed of solid Nb with a design gradient of 5 MV/m,

---

[1] The SC cavities at LEP ran at 352 MHz, in standing wave mode, with four-cell, and an active length of 1.7 m.

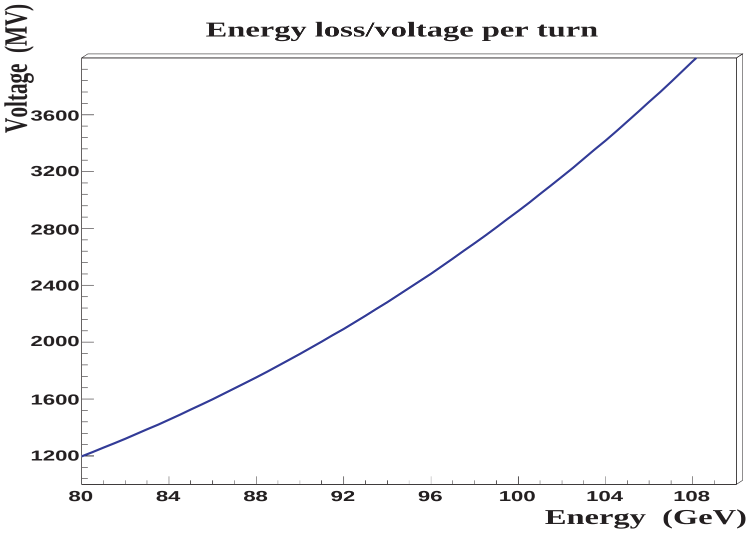

Figure 3.4: The required RF voltage per turn, to make up for radiative energy losses in LEP, as a function of the beam energy [31].

while all later ones were made by sputter-coating a Cu substrate with a thin layer of Nb with a higher design gradient of 6 MV/m. In 1996, the number of SC cavities increased to 144, and $W^{\pm}$ physics on LEP started at 80.5 GeV beam energy. Subsequently more SC cavities were added, when all available space was filled, partially replacing the original copper system. The final configuration of the LEP RF system included 56 Cu cavities, 16 solid Nb SC cavities and 272 sputtered Nb SC cavities [30].

With continual upgrading of the RF system, LEP was able to increase the beam energy from 45 GeV before 1995 to 104 GeV in 2000 (see Figure 3.5). The last two years of LEP physics emphasized the search for new phenomena such as the Higgs boson, and consequently the highest possible beam energy at good luminosity became the main priority. Instead of increasing the number of SC cavities, as in previous years, the gain in beam energy during the last two years was mainly achieved[2] by pushing the RF system far beyond its original specifications (see Figures 3.5 and 3.6), and leaving less RF margin [30, 32].

The solid Nb cavities had a nominal design gradient of 5 MV/m and were operated up to 4.5 MV/m. The average gradient of the sputtered SC cavities was significantly increased above the design gradient of 6 MV/m (see Figure 3.6). In 2000, the LEP RF system routinely provided more than 3620 MV, allowing the beam energy to be raised up to 104.5 GeV [30].

---

[2] Other factors were as follows: using reduced RF frequency, increasing bending radius by using corrector magnets, and changing the horizontal damping partition number, etc.

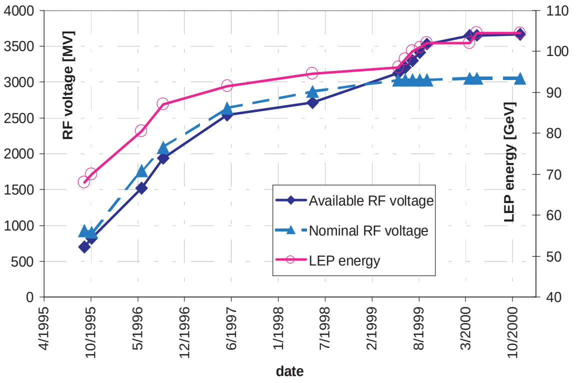

Figure 3.5: Beam energy, available and nominal RF voltage from 1995 until 2000 [30].

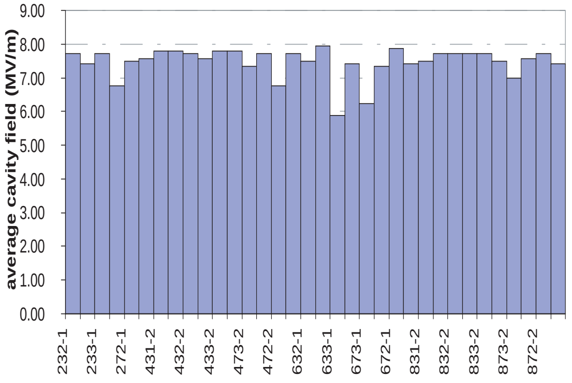

Figure 3.6: Average accelerating gradient of RF units with sputtered SC cavities after conditioning in 2000 [30].

An RF voltage margin was necessary due to cavity trips from time to time[3]: by working at an energy lower than the maximum, it was possible to keep the beam when having RF trips. Trips of the RF cavities were issued by an interlock system, and occurred mainly due to field emission, on a statistical basis. An RF trip resulted in the lost of the voltage of eight cavities driven by the same klystron, about 100 MV, corresponding to 0.8 GeV in beam energy. Due to the cost in energy of the RF voltage margin, a special ramping strategy was implemented in 2000 to obtain the highest possible beam energy with good luminosity. A physics fill was started at an energy equivalent to a 2 klystrons margin, then after a while the beam was ramped, under physics conditions, to an energy equivalent to a 1 klystron margin. Towards the end of a fill the beam energy was ramped to the maximum (no RF margin), the end of fill then being given by the next RF trip [30, 32].

3.1.3 Beam energy measurement

For many LEP physics measurements, such as the properties of the Z^0 and the mass of the $W^\pm$ bosons, the precise determination of LEP beam energy was crucial.

Evaluation of LEP1 center-of-mass energy [33]

During LEP1 runs, in the region of the Z resonance, the beam energy was accurately measured by the resonant depolarization method. The attained precision was more than one order of magnitude better

---

[3] The average time between RF trips was 14 min and recovery normally took about 2 min [30].

than that provided by other existing methods [34].

Due to the Sokolov-Ternov effect [35], an electron beam can be vertically polarized because of the emission of synchrotron photons. The asymptotic polarization level is

$$P_\infty = \frac{8}{5\sqrt{3}} \frac{1}{1+\tau_p/\tau_d} \ , \tag{3.2}$$

where $1/\tau_p$ and $1/\tau_d$ are the rates of self-polarization and depolarization of the beam. In the simplest model, the ratio $\tau_p/\tau_d \propto E^2$. An oscillating radial field from an RF-magnet was used to artificially deflect the polarization vector. The depolarization is maximized if the RF-magnet field is in phase with the spin precession. This happens when the frequency of the oscillating field f_{dep} satisfies,

$$f_{dep} = (k \pm [\nu]) \cdot f_{rev} \ , \tag{3.3}$$

where f_{rev} is the revolution frequency of the particles ($f_{rev} = 11.25\ kHz$ at LEP) and k is an integer. $[\nu]$ denotes the non-integer part of the spin tune, which is the number of cycles the spin vector of a beam particle will precess during one revolution in the storage ring. ν is directly proportional to the beam energy E:

$$\nu = \frac{aE}{mc^2} = \frac{E[MeV]}{440.6486(1)[MeV]} \ , \tag{3.4}$$

where a is the anomalous magnetic moment of electron, and m is the mass. Knowing f_{rev} to $\sim 10^{-10}$, and measuring f_{dep} up to $\sim 2\ Hz$ in $\sim 1\ MHz$, one can get ν, and thus calculate E to $\Delta E/E = 2 \cdot 10^{-6}$. Combining systematics, the overall uncertainty on E_{cm} is less than $1\ MeV$. The measurement was so accurate that it was actually sensitive to, for example, the tidal effects of the Moon and Sun, and even passing trains [36].

Evaluation of LEP2 center-of-mass energy [37, 38]

Due to an insufficient polarization level, the center-of-mass energy at LEP2 was evaluated using a magnetic extrapolation method. The average beam energy was measured with the resonant depolarization method in the range 41 - 61 GeV, and the beam energy for the physics run was then inferred from the change of the magnetic field in LEP main bending dipoles, measured by NMR (Nuclear Magnetic Resonance) probes both during the resonant depolarization measurements and during physics fills.

A flux-loop field measurement was used to compare with the NMR probe method, and determine the systematic uncertainty of the beam energy measurement. Two alternative methods of beam energy determination, the LEP2 spectrometer[4] and a fit of the total RF voltage to the synchrotron tune, were

---

[4] The setup consisted of a steel bending magnet flanked by a triplet of beam position monitors at each side providing a measurement of changes in the bending angle when the beams were accelerated to physics energies [39].

implemented since 1999. All these methods gave consistent results. Table 3.1 shows the result of beam energy measurements from the LEP energy working group[5].

Year	Nominal $E_{CM}(GeV)$	Uncertainty of $E_b(MeV)$	E_{CM} spread (MeV)
1996	161	27	144 ± 7
1996	172	30	165 ± 8
1997	183	25	219 ± 11
1998	189	20	237 ± 12
1999	193	21	254 ± 13
1999	196	21	266 ± 13
1999	200	21	265 ± 13
1999	202	21	253 ± 13
2000	206	25	236 ± 12

Table 3.1: The uncertainty of beam energy and luminosity weighted center-of-mass energy spread [38].

3.1.4 Particle background at LEP detectors [41, 42]

The two main types of beam induced particle backgrounds in the LEP experiments were photons from synchrotron radiation (SR) in the fields of straight section quadrupoles and off-energy electrons/positrons from bremsstrahlung of beam particles with rest-gas molecules along the straight sections and the first part of the bending arcs. The rate of off-energy electrons produced by beam-gas interactions is to first order independent of beam energy. However, the number of radiated SR-photons and the critical energy of the spectra increase sharply with beam energy and would lead to very high photon background level during LEP2 running.

To cope with this situation, the background protection system has been upgraded for LEP2 running, by adding collimators, using enlarged vacuum chambers, photon absorbers and synchrotron radiation masks close to the interaction points (IPs). Dedicated radiation monitoring system and a beam-dump trigger system have been installed on the LEP detectors, to provide extra protections against radiation background, especially during unstable beam conditions.

---

[5] A recent report of the LEP beam energy measurement, using radiative return to the Z events, also showed consistent results [40].

3.1.5 LEP performance [43]

LEP, from its commissioning in 1989 until its final shutdown in November 2000, operated in many different modes, with many different optics settings and at many different energies. LEP has provided a huge amount of data for the precision study of the Standard Model and searches beyond that, first on the Z^0 resonance, then above the $W^\pm$ threshold, and finally, with beam energy above 100 GeV, hunting for the Higgs bosons. A summary of the performance through the years is shown in Table 3.2.

As an example, Figure 3.7 shows the maximum expected mass, with 3σ sensitivity, reachable in searches for the Standard Model Higgs boson at LEP, given the produced luminosity and energy.

Year	Beam Energy $[GeV]$	Total Current $[mA]$	$\int L\ [pb^{-1}]$	Peak Lumi. $[10^{30}cm^{-2}s^{-1}]$
1989	45.6	2.6	1.74	4.3
1990	45.6	3.6	8.6	7
1991	45.6	3.7	18.9	10
1992	45.6	5.0	28.6	11.5
1993	45.6	5.5	40.0	19
1994	45.6	5.5	64.5	23.1
1995	45.6-70.0	8.4	46.1	34.1
1996	80.5-86.0	4.2	24.7	35.6
1997	91.0-92.0	5.2	73.4	47.0
1998	94.5	6.1	199.7	100
1999	96.0-101.0	6.2	253	115
2000	100.0-104.5	5.2	233.4	60

Table 3.2: Performance of LEP from 1989 to 2000 [29, 43].

3.2 The L3 detector

Over the quarter of century before the construction of the LEP detectors, some of the most spectacular discoveries in experimental particle physics have been associated with precision measurements of photons and leptons. Examples are the discovery of the J/ψ, the discovery of the Υ, and the discovery of the Z^0 and $W^\pm$. So the main purpose of the L3 detector, as it was designed, was not to verify any particular

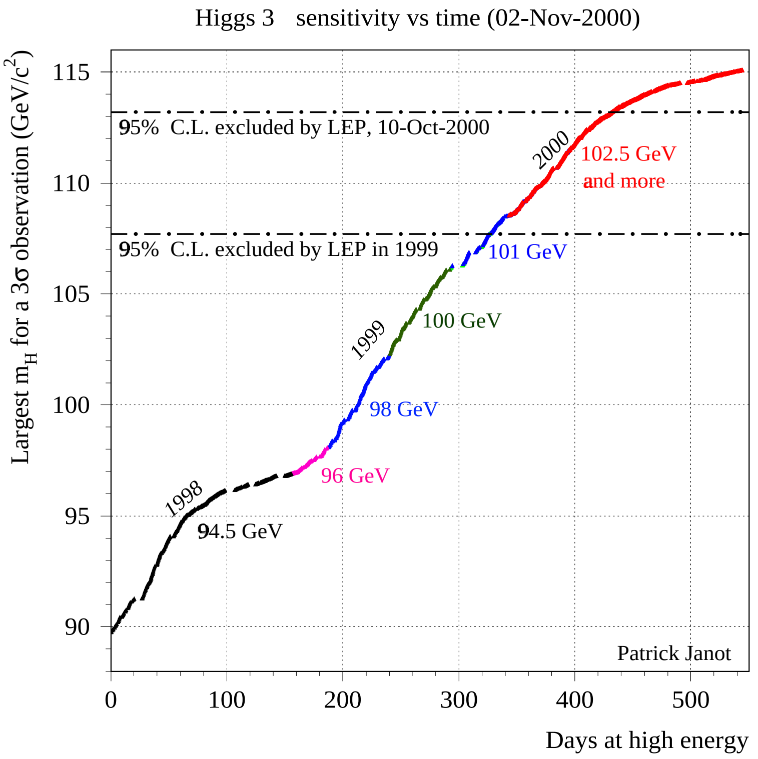

Figure 3.7: Given the delivered luminosity and energy at a specific date, the corresponding expected mass limit with 3σ sensitivity in searching for the Higgs boson, as a function of running days.

theory or prediction, but to use the good resolution of the detector on leptons and photons to explore the unknown [44] by searching for new physics processes.

L3 was built to have superior ability to measure photons, electrons, and muons with a resolution of $\Delta P/P \sim 1\%$, and at the same time, to measure hadron jet energies with a good resolution [44]. The detector was a multi-layered cylindrical set of different devices, each of which measured different physical quantities in e^+e^- collision events. Starting from the center, close to the beam pipe, the L3 detector consisted of a series of sub-detectors:

- Silicon Microvertex Detector (SMD)
- Luminosity Monitor (LUMI)
- Time Expansion Chamber (TEC)
- Scintillation Counters

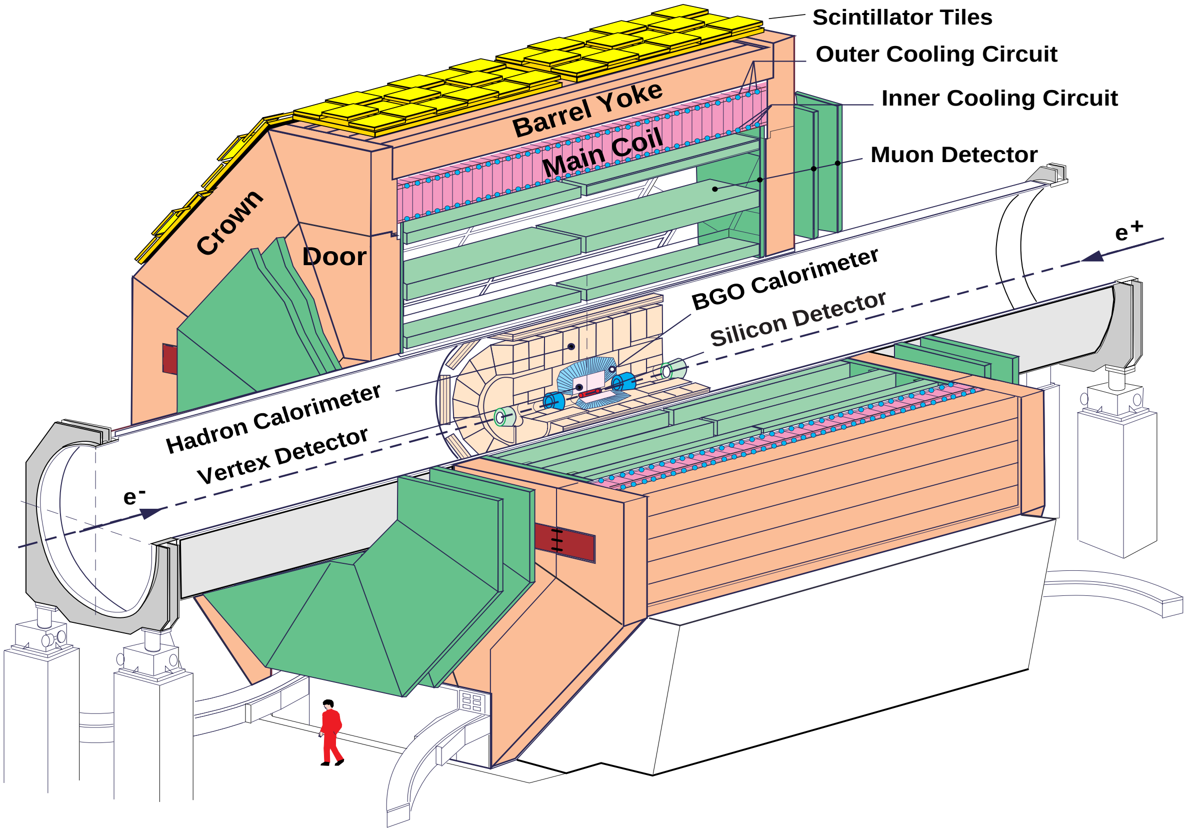

Figure 3.8: A perspective view of the L3 detector.

- Crystal Electromagnetic Calorimeter (ECAL)
- Hadron Calorimeter (HCAL) and Muon filter
- Muon Chambers (MUCH)

All of these sub-detectors were mounted inside a large volume ($\sim 1300\ m^3$) solenoid magnet producing a magnetic field of 0.5 T. Before the 1999 and 2000 LEP running, a 202 m^2 t_0 scintillator system was installed in two phases on top of the L3 magnet. Together with an air shower scintillator array on the roof of the surface hall above L3, it enabled precise measurements of cosmic muons with momenta between 20 GeV and 2 TeV, using the existing L3 sub-detectors. The cosmic muon measurement (L3+Cosmics) was carried out in parallel with the colliding beam experiment, without disturbing each other.

A perspective view of L3 detector is shown in Figure 3.8, and a detailed side view of the inner

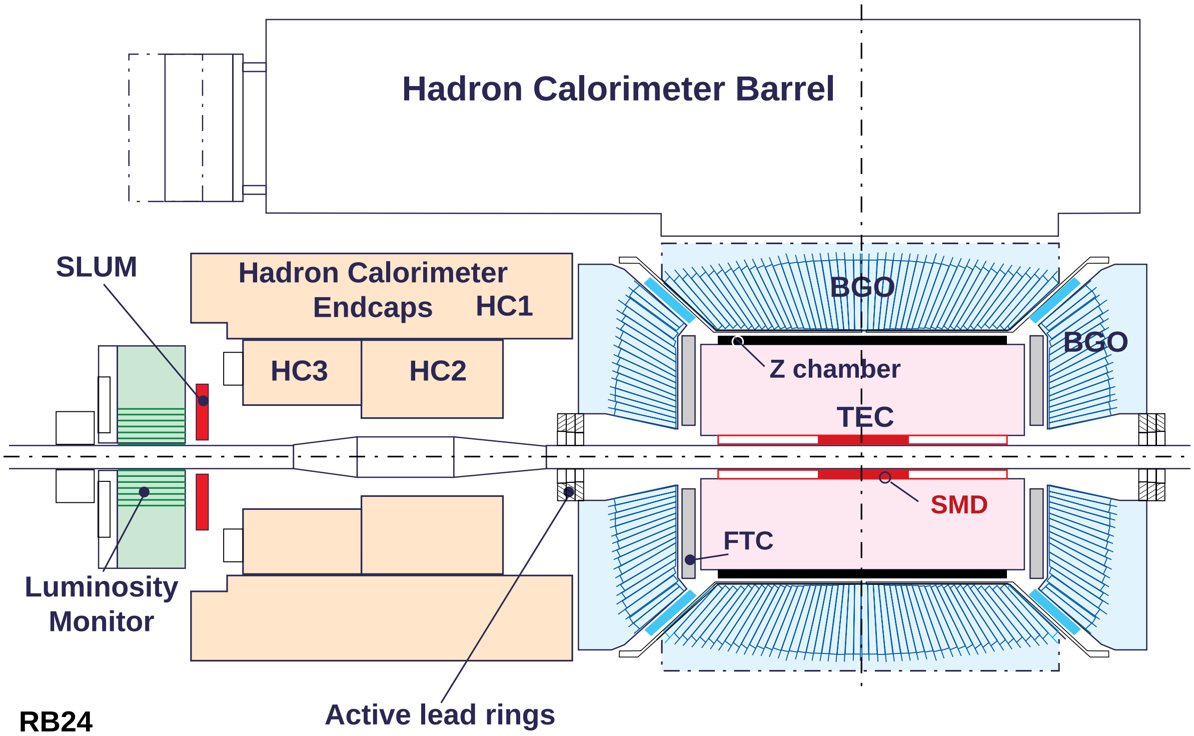

Figure 3.9: A side view of the L3 inner detector components: SMD, TEC, ECAL, HCAL, in the region around the beam pipe, and the forward detector components: ALR (Active Lead Rings), SLUM (Silicon), and LUMI (Crystal) for luminosity measurement.

detectors is shown in Figure 3.9. In the following sections, the L3 sub-detectors will be discussed in detail, with an emphasis on those aspects related to vertex determination, track detection, and lepton identification, which are crucial for this analysis.

3.2.1 Silicon Microvertex Detector [45]

The L3 Silicon Microvertex Detector (SMD) was installed before the 1993 running, since the radius of the LEP beam pipe at its four interaction points was reduced from 8 *cm* to 5.5 *cm* at the beginning of 1991.

It consisted of 24 identical "ladders," arranged in two cylindrical layers with mean radii 60.7 *mm* and 77.5 *mm*, respectively (see Figure 3.10). Each ladder was built from 4 silicon sensors, and each sensor was 70 *mm* long, 40 *mm* wide, and 300 μm thick. The sensor was a high purity n-type silicon wafer, with parallel strips every 25 μm along the z direction on one side and every 50 μm along the ϕ direction on the other side. The strips along the z direction were on the junction side, had a readout pitch of 50 μm, and could measure the $r - \phi$ coordinate with ~ 7 μm resolution. The strips along the ϕ direction were on the ohmic side of the sensor, had a readout pitch of 150 *mm* ($|cos\theta| < 0.53$) or 200 *mm* ($0.53 < |cos\theta| < 0.93$), and could measure the $r - z$ coordinate with 14 μm resolution. The installation of SMD significantly improved the transverse momentum resolution and the impact parameter measurement. Figures 3.13 and 3.14 show the DCA and $1/P_T$ resolution in the year 2000, combining information from both the SMD and TEC.

The L3 SMD provided 2π coverage in azimuthal angle, and covered the polar angle region $|cos\theta| < 0.93$. It had 72576 readout channels in total. The whole system added very little material ($\sim 1.3\%$ of a radiation length at normal incidence) in front of the other detectors.

To protect the SMD against catastrophic radiation damage, a dedicated radiation monitor was installed in the vicinity of SMD to provide both a fast beam dump signal if the radiation dose rate exceeded a pre-defined threshold and a long term monitoring of the total radiation dose. More detail on the radiation monitor and its operation will be given in Chapter 4.

3.2.2 Time Expansion Chamber [46]

The L3 Time Expansion Chamber (TEC) was designed to perform both vertex detection and particle tracking. This detector had the following tasks in the L3 experiment:

- Measure the transverse momentum and determine the sign of charged particles

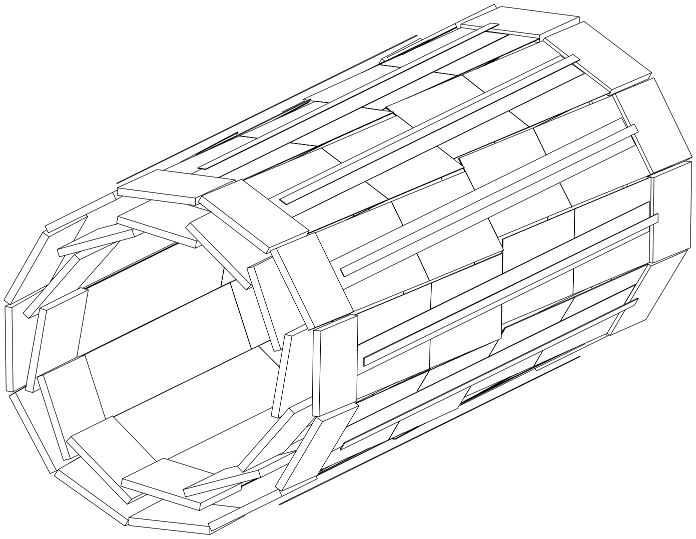

Figure 3.10: A perspective view of L3 Silicon Microvertex Detector (SMD).

- Determine the charge multiplicity of the event
- Together with SMD, reconstruct the interaction point and determine the lifetime of short lived particles
- Determine the particle's entrance point to the electromagnetic calorimeter (ECAL), and distinguish electrons from photons together with the ECAL
- Measure the ionization of tracks to identify particles and search for unknown heavy charge particles with long lifetime

The TEC was a cylinder with an inner radius of 90 mm, an outer radius of 457 mm and a total sensitive length of 970 mm. It consisted of two concentric chambers which are in the same gas volume (Figure 3.11). The inner TEC chamber was divided into 12 symmetric sectors and the outer TEC chamber into 24 symmetric sectors. Figure 3.12 shows one inner and two outer TEC sectors, and the wire distribution.

In order to precisely measure the momentum of energetic charged particles in the small inner volume defined by ECAL, the TEC was designed with the following characteristics: a low drift velocity ($\sim$ 6 $\mu m/ns$), a low diffusion gas, a shaping amplifier removing the ion tail of analog pulses from the

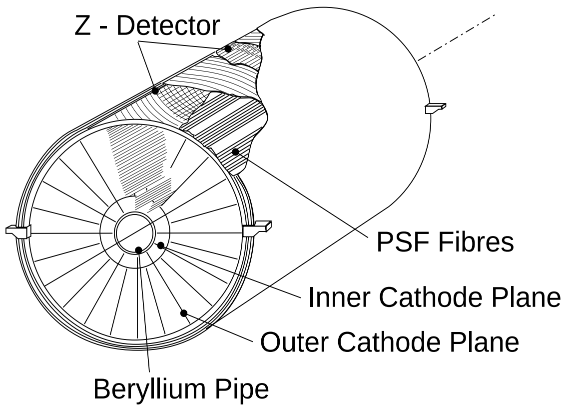

Figure 3.11: A perspective view of the L3 TEC.

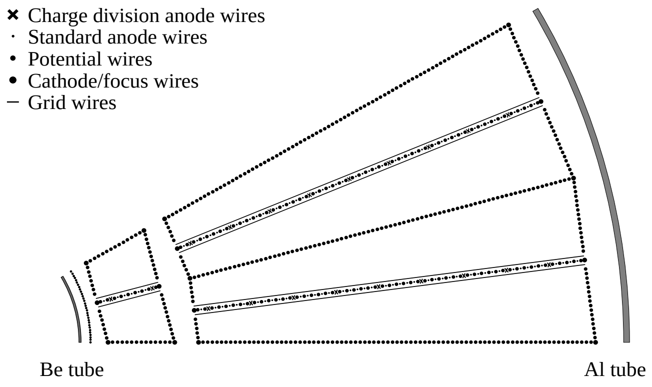

Figure 3.12: A TEC ϕ sector viewed in $r-\phi$ plane.

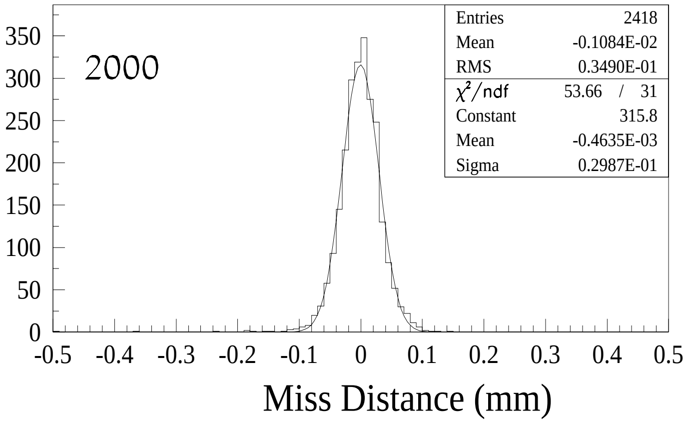

Figure 3.13: The L3 DCA resolution: TEC + SMD.

anode, and a readout of the signals from the wires by 100 MHz flash analog-to-digital converters (FADC) to allow for drift time determination by the center of gravity method [44, 46]. An average single wire spatial resolution of 58 μm and a double track resolution of 640 μm were achieved.

Figure 3.13 shows the DCA resolution in year 2000 of the L3 vertex detectors, $\sigma = 30\ \mu m$, combining information from both the SMD and TEC. Figure 3.14 shows the $1/P_T$ resolution in year 2000, combining information from both the SMD and TEC.

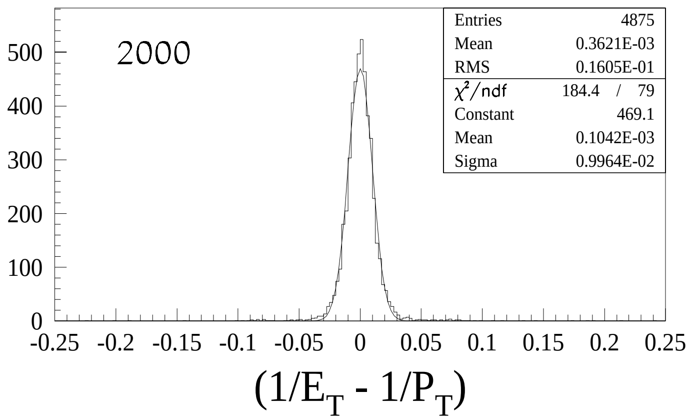

Figure 3.14: The L3 $1/P_T$ resolution: TEC + SMD.

3.2.3 Crystal Electromagnetic Calorimeter and RFQ Calibration

The Electromagnetic Calorimeter was designed to measure the energies and positions of electrons and photons with energy ranging from 20 MeV to 100 GeV with high resolution and, together with the hadron calorimeter, determine properties of hadronic final states [44].

The L3 ECAL used bismuth germanium oxide (BGO) crystals as both the showering and detecting medium. The detector consisted of about 11,000 BGO crystals pointing to the interaction region. They were mounted in the cells of a carbon fiber honeycomb structure, and were made in two main parts: the central part ("barrel") and the forward part ("end-caps"). The barrel part consisted of 7,680 crystals, each cut into a truncated pyramid shape, 24 cm long with 2 $cm \times 2$ cm inner end, 3 $cm \times 3$ cm outer end. The ECAL barrel covered the polar angle range $42^o < \theta < 138^o$. The two end-caps consisted of 1527 BGO crystals each, and covered range of polar angles $11.6^o < \theta < 38^o$ and $142^o < \theta < 168.4^o$. All crystals pointed to the interaction region, with a small angular offset to suppress photon leakage. By coating the polished crystals with high reflectivity paint, one obtained a nearly uniform light collection efficiency. At the outer end of each crystal, two photo-diodes, each with 1.5 cm^2 active area and $\sim 70\%$ quantum efficiency at 480 nm, were glued to the crystal surface to collect the scintillation light [44, 47].

Due to the strong dependence of crystal light yield on its temperature, the whole system was under strict thermal control. The gradient along the crystal axis was designed to be less then $0.25^oC/24$ cm. In addition, several hundred AD590 thermal sensors were installed to monitor temperature changes with a sensitivity of $\pm 0.1^oC$ [44].

The crystal light yield could be affected by irradiation and its self recovery. It was then crucial to

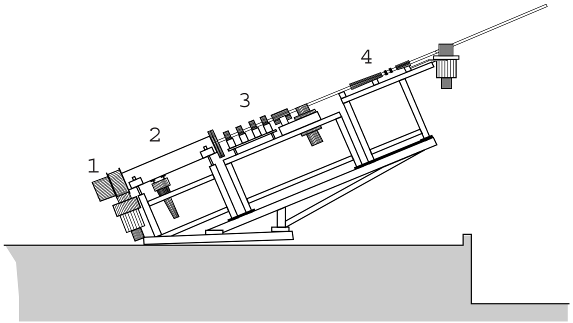

Figure 3.15: Perspective view of the RFQ system: 1. ion source, 2. RFQ accelerator, 3. steering and focusing magnets, 4. beam neutralizer.

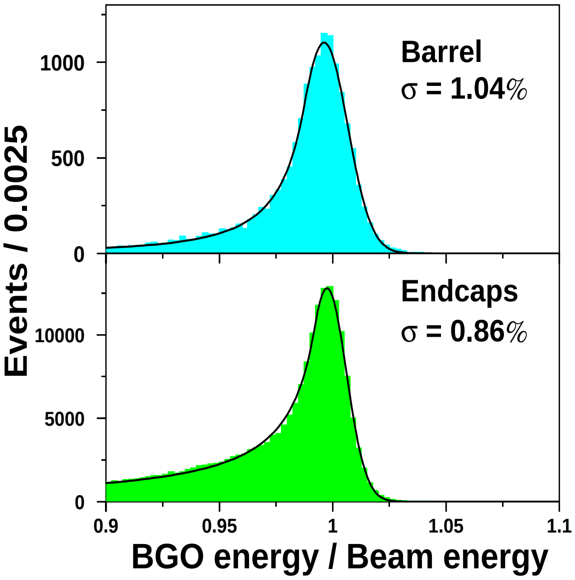

Figure 3.16: Bhabha energy spectrum in the ECAL barrel and end-caps region, obtained in 2000.

have accurate calibration and stability monitoring of the crystals, so that the designed high resolution of the calorimeter could be achieved. A combination of several methods was used. Before installation, a pre-calibration of each crystal with cosmic rays and of each photo-diode with a Co^{57} source was made. The barrel part of the calorimeter was further calibrated at a CERN SPS test beam, as well as a special test beam extracted from the LEP injector. After installation, a xenon flash method [48] was used to monitor the transparency of crystals, as well as to track the overall response of a given crystal relative to its neighbors. The precise absolute calibration was achieved by Caltech's RFQ calibration system together with Bhabha scattering information [44, 47].

The RFQ calibration system [49, 50] used a pulsed H^- beam from a radio-frequency quadrupole (RFQ) accelerator to hit a lithium target installed inside the ECAL. The beam was neutralized by a beam neutralizer so that it can pass through the magnetic field of the L3 detector. Radiative capture of the protons by the target produced 17.6 MeV photons with very high rate, which were used to calibrate the calorimeter in a few days [51].

A perspective view of the RFQ system is shown in Figure 3.15. It consists of

- a 30 KeV H^- ion source

- a 1.85 MeV RFQ accelerator
- steering and focusing magnets
- a beam neutralizer with nitrogen cell
- a Li target (not shown on the plot)

The ion source, RFQ accelerator and neutralizer cell were shielded from the fringe field of the L3 magnet. By using the 17.6 MeV photons from the target as the calibration source, we obtained an absolute calibration with the calibration constant:

$$Calibration\ Constant\ (KeV/ADC\ channel) = \frac{E_{HH^+}}{HH^+ - Pedestal}\ , \tag{3.5}$$

where the HH^+ edge was the half height point on the upper edge of the calibration signal peak. The sharp falling edge of the peak ensured this point to be the least sensitive to a number of possible systematic effects. Using this calibration directly, which was referred as the "RFQ Only" method, one observed a typical energy resolution $\sim$ 2.3%, while without any calibration, it was larger than 8%. This method was limited by the nonlinearity of the calorimeter when extrapolate the calibration from 17.6 MeV to high energy, and by the geometric effects since the target was placed far away from the interaction point.

To overcome these limitations, an 'RFQ+Bhabha' method has been introduced [51, 52]. It took the "RFQ Only" calibration as the relative inter-calibration, and used Bhabha event information to correct the geometric effects and detector non-linearity. Applying this method, an overall resolution of $\sim$ 1% was achieved in the energy spectrum of Bhabha scattering electrons and positrons, corresponding to a calibration precision of better than 0.5%. Figure 3.16 shows the Bhabha spectrum in 2000, after "RFQ+Bhabha" calibration.

3.2.4 Scintillation Counters

The L3 scintillation counter system consisted of 30 single plastic counters in the barrel region and 8 plastic counters on each endcap. It was located between the electromagnetic and hadronic calorimeters, covered the polar angle region $cos\theta < 0.83$ in the barrel and goes down to $cos\theta = 0.90$ in the end-caps.

The time resolution of the counter system was approximately 1 ns, so it could clearly reject the cosmic muons from colliding beam events (for example, di-muon events). The flight time for a cosmic muon to go through the two opposite layers of the scintillation counters is about 5.8 ns. The scintillator hit multiplicity was also used as an independent trigger for hadronic events.

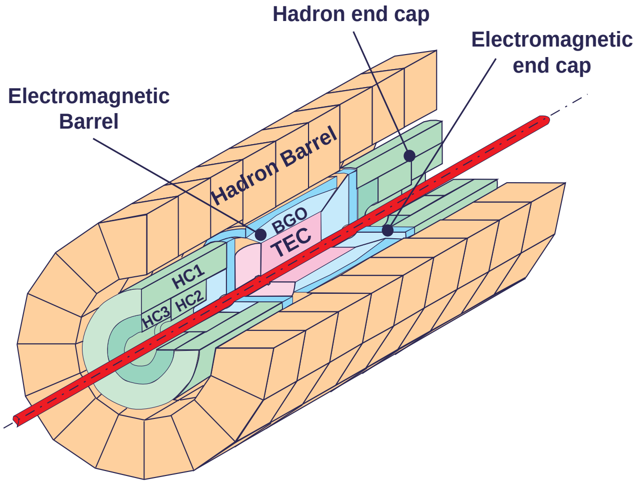

Figure 3.17: A perspective view of the L3 hadron Calorimeter (HCAL).

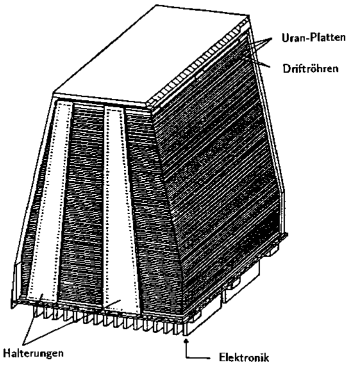

Figure 3.18: A barrel module of the L3 hadron Calorimeter.

3.2.5 Hadron Calorimeter

The energy of hadrons emerging from e^+e^- collisions was measured in L3 by the total absorption technique with the electromagnetic and hadron calorimeters. The hadron calorimeter (HCAL) consisted of three parts: the central "barrel" made of nine rings with sixteen modules in each ring and a muon filter outside the rings; and two end-caps. A perspective view of the hadron calorimeter is shown in Figure 3.17, and a barrel module is shown in Figure 3.18. Depleted uranium plates were used in the barrel and end-caps as the absorption material, and the sampling elements were chosen to be wire chambers operating in the proportional mode with analog pulse height readout. The muon filter used brass absorber layers alternating with brass proportional tubes, and was designed to reduce the rate of punch-through particles reaching the precise muon spectrometer [44, 47].

The barrel part of the HCAL covered the angular region $35^o < \theta < 145^o$, and the end-caps extended the coverage to $5.5^o < \theta < 174.5^o$, which is 99.5% of the 4π solid angle. The energy resolution, σ, defined as the standard deviation of a Gaussian fit to the pulse height distribution, as a function of E was found to be

$$\frac{\sigma}{E(GeV)} = (\frac{55}{\sqrt{E(GeV)}} + 5)\%. \tag{3.6}$$

Since uranium is radioactive, it also served as a built in γ source for the calibration of the wire chambers. The chambers were oriented in such a way that alternating chambers had their wires perpendicular to each other, to get a better angular resolution of hadron jets.

By measuring the total energy of two-jet events at the Z^0 peak, an energy resolution of 10.2% was

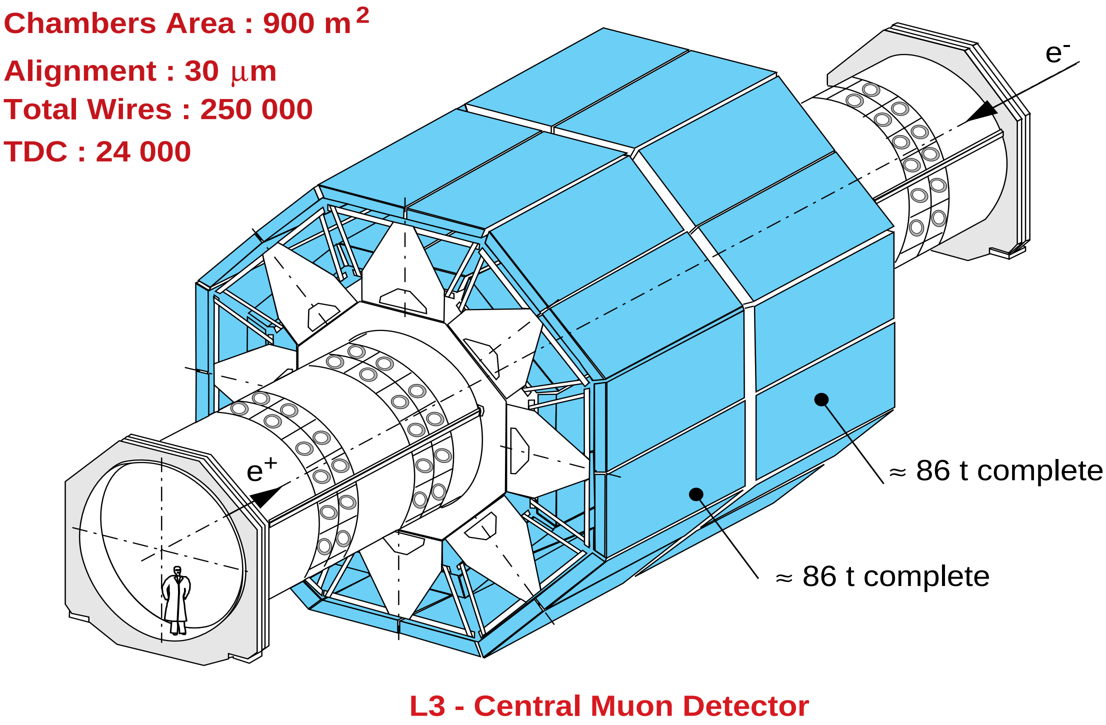

Figure 3.19: A perspective view of the L3 Muon Chambers.

reached, which is in very good agreement with the above formula. The angular resolution achieved was $\Delta\theta = 2.5^o$ and $\Delta\phi = 3.5^o$.

3.2.6 Muon Chambers [44, 47]

The design goal of the L3 muon chambers was to precisely measure muon momentum and direction in the central muon detector, *i.e.*,

- to measure the curvature of 50 GeV muon tracks to 2% accuracy
- to reach a di-muon mass resolution of 1.4% at 100 GeV

The central muon detector consisted of two "ferris wheels," each of which included eight independent units, called "Octants" (see Figure 3.19). Each octant (see Figure 3.20) consisted of a special mechanical structure supporting five precision drift chambers (P chambers). There were two chambers in the outer layer (MO), each with 16 signal wires, two chambers in the middle layer (MM), each with 24 signal

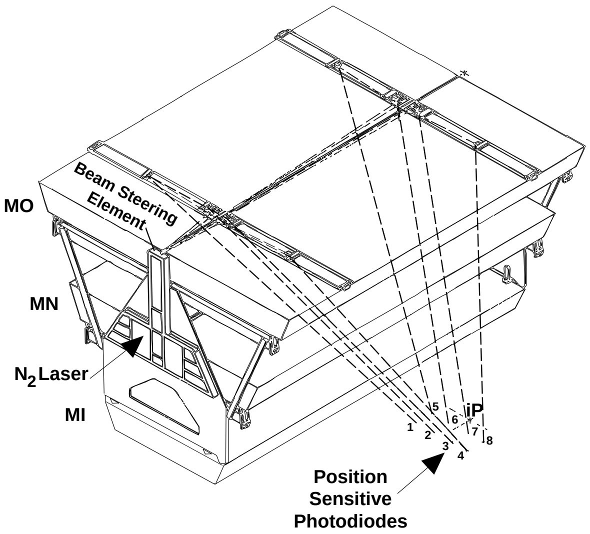

Figure 3.20: A perspective view of a single octant and the laser monitoring system.

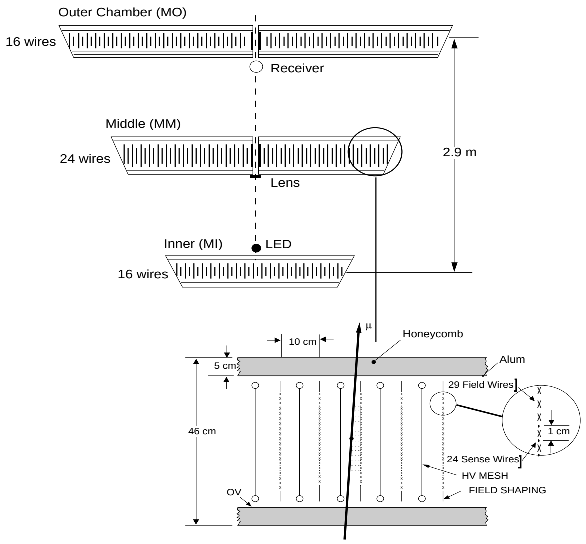

Figure 3.21: The "MO," "MM," and "MI" chambers in an octant and the wire configuration in a P chamber.

wires, and one inner chamber (MI), with 16 signal wires (see Figure 3.21). The three layers of chambers were approximately 1 m apart, and measure track coordinates in the bending plane. The top and bottom covers of the MI and MO chambers were each equipped with two additional layers of chambers which measured the z coordinate along the beam pipe direction (Z chambers).

Each P-chamber contained about 320 signal wires and a total of 3,000 wires (including field shaping, cathode and guard wires), and had a single wire resolution of about 200 μm. The Z chambers consisted of two layers of drift cells offset by one half cell with respect to each other to resolve the left-right ambiguities. The chamber resolution was typically 300 to 500 μm.

To achieve the design resolution, the reduction of systematic errors in the alignment was critical. Because muons with energies more than 3 GeV were confined to a single octant, the alignment errors between chambers in the same octant were dominant and were kept below 30 μm. The positions of the chambers were further monitored *in situ* by a laser system (see Figure 3.20) after installation. Each of the 16 octants contained a two-stage nitrogen ultraviolet laser. The laser beam was directed up and across the top of the outer chamber layer. Mirrors directed the beam down through quartz windows into selected drift cells of all layers of an octant, pointing roughly to the interaction point. Each octant had eight laser beam trajectories, which left a straight-line ion trail in the gas, to simulate infinite momentum particles coming from the interaction point. The sagitta of the "laser events" should have

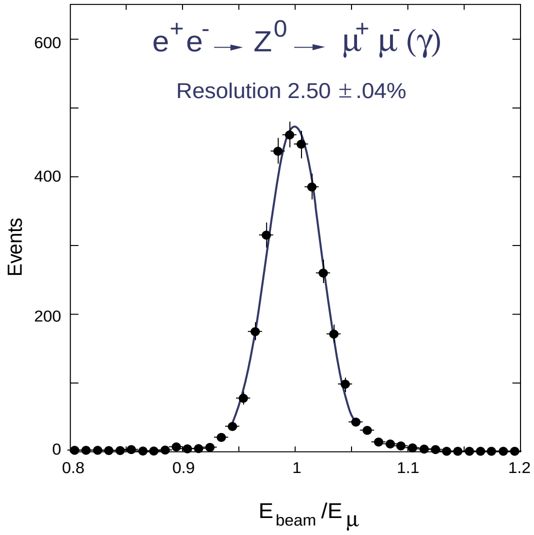

Figure 3.22: The resolution on muon momentum at the Z^0 peak.

been zero, and this was used to verify the alignment. Two laser beams had movable mirrors and could produce parallel trajectories of known separation, allowing us to measure and constantly monitor the electron drift velocity.

The central muon chambers covered the polar angle region $44^o < \theta < 136^o$ with high precision ($\sim 2\%$, using all three P chambers), which was about 64% of the 4π solid angle. It also covered $35^o < \theta < 44^o$ and $136^o < \theta < 145^o$ with lower precision ($\sim 15\%$, MI and MM chambers only), which was another 12% of the solid angle. During the shutdown periods in 1993-1994 and 1994-1995, a forward-backward muon chamber system (FB) was installed on the L3 magnet doors (see Figure 3.8), and this extended the angular coverage to $22^o < \theta < 158^o$. The FB chambers consisted of three layers, with one inside the magnet door, and two outside. With the FB muon chambers, the L3 muon system covered polar angles $36^o < \theta < 43^o$ and $137^o < \theta < 144^o$ with MI, MM and the inner layer of FB, and had momentum resolution of $\sim 2 - 20\%$ depending on θ. It covered $22^o < \theta < 36^o$ and $144^o < \theta < 158^o$ with the three layers of FB chambers, and had momentum resolution of approximately 25% in these regions.

The accuracy of the L3 muon chamber system during the experiment was verified by $Z \rightarrow \mu^+\mu^-$ data, taking into account the radiative corrections. The observed resolution, $\sigma(E_{beam}/p_\mu) = 2.5\%$, agreed with the design value (see Figure 3.22).

3.2.7 Luminosity Monitor [53]

The integrated luminosity serves as an absolute normalization of event rates observed in detectors. At L3, it was determined by a small angle Bhabha scattering ($e^+e^- \rightarrow e^+e^-(\gamma)$) measurement, in the luminosity monitor (LUMI). The Bhabha scattering cross section has been calculated with high precision from QED. To lowest order, the small angle Bhabha cross section (integrated over the azimuthal angle, ϕ), in a detector with a polar angle coverage from θ_{min} to θ_{max} is given by

$$\sigma = \frac{16\pi\alpha^2}{s}(\frac{1}{\theta^2_{min}} - \frac{1}{\theta^2_{max}}), \tag{3.7}$$

where α is the fine-structure constant and s is the square of the center-of-mass energy. For small scattering angles as we consider here, the reaction is dominated by t-channel exchange and the $\gamma - Z$ interference effects are small.

The L3 luminosity monitor consisted of a calorimeter made of BGO crystals (LUMI), which provided excellent energy resolution and an efficient trigger, complemented by a tracker made of single-sided silicon wafers (SLUM). The wafers had very high intrinsic geometrical precision ($1 - 2\ \mu m$) and could be accurately positioned and measured (to 6 μm).

The luminosity detector was situated at small polar angles (see Figure 3.9). The LUMI consisted of two detectors, which were situated on each side of the interaction point, at a distance of 2730 mm, with polar angle coverage of $31 - 62\ mrad$ relative to the beam line on both sides. Each calorimeter was cylindrically symmetric and consisted of 304 BGO crystals parallel to the beam axis. Each crystal was read out by a Hamamatsu photodiode, and monitored by a green light LED mounted on the front side.

The SLUM was mounted in front of each LUMI calorimeter. On each side, the detector had three layers which consisted of 16 overlapping wafers: two layers of strips concentric with the beam axis (r wafers) to measure the θ angle of a traversing particle, and one layer of strips perpendicular to the beam axis (ϕ wafers) to measure its ϕ angle. The r wafers each contained 96 silicon strips with three different pitches: $64 \times 0.5\ mm$, $16 \times 1.875\ mm$, $16 \times 1.0\ mm$, so that the cut boundaries of the fiducial volume had the best granularity. There were 64 channels on each ϕ wafer, giving a total of 8192 channels for the complete SLUM detector.

The Bhabha events were selected using the calorimetric measurement in the BGO to provide a background free sample of events, and the silicon tracker selected only those Bhabhas that were contained in a precisely defined fiducial volume. The uncertainty in the L3 luminosity measurement came mainly from systematics: the uncertainty on the theoretical cross section and limited Monte Carlo statistics.

For data sets used in this analysis, the uncertainty on the integrated luminosity is about 0.2%.

3.2.8 T_0 Scintillators and L3+Cosmics [54]

Since the L3 detector had a huge solenoidal magnet of volume $\sim 1,300\ m^3$, and a high-precision muon spectrometer installed in this volume, it was an ideal detector for cosmic muon measurement. In order to reconstruct a muon track passing through the detector, an excellent knowledge of the time when a muon passed through each layer of the muon detector was required. In contrast to the colliding beam events, where beam crossing provided accurate timing, the measurement of cosmic muons relied on the newly installed t_0 scintillators on top of the original L3 detector (see Figure 3.8). The time of passage through each layer of the muon chambers could be calculated from the precise timing obtained from t_0 and the time-of-flight from the scintillator to each of the layers. The experiment that used these facilities to measure cosmic muons is called L3+C.

L3+C was a unique detector in several respects. It had a large acceptance of some 200 m^2sr and was covered by only 30 m of overburden, in contrast to other underground muon experiments. The energy threshold was therefore accordingly low (15 GeV), and the multiple scattering of muon tracks remained below 4 $mrad$ above 100 GeV energy. The precision drift chambers allowed the measurement of muon momenta between 20 GeV and 2 TeV, with one of the best resolutions obtained so far. The parallel running of colliding beam experiment and cosmic muon measurement enabled L3+C to determine the resolution and detector efficiency, by using the muon pairs from Z^0 decays.

The t_0 scintillator system covered a total area of 202 m^2, and was divided into three separate parts for the three top octants with 72, 72 and 58 m^2, respectively. The smallest unit of the scintillator array was a scintillator tile with a size of $25 \times 25 \times 2\ cm^3$; sixteen of these tiles were packed in an aluminum box forming a 1 m^2 scintillation area called a cassette. The readout was performed by wavelength shifting fibers and photomultipliers (XP2020 by Philips). The average hit efficiency was 96.3%, and the average time resolution was about 1.8 ns.

3.2.9 Trigger and Data Acquisition System [44, 47]

The L3 trigger and data acquisition system made use of three levels of triggers and several levels of event buffering before the data was written out to mass storage. Because of the complexity of the L3 detector, it was physically and logically divided into sub-detectors, each of which had its own separate level-1 trigger electronics chain, which encoded the trigger data and sent them to the level-1 trigger logic and level-2 trigger. This data stream was completely separate from the main detector data which was used by the level-3 trigger. The task of the data acquisition system was to coordinate the flow of data with the decisions of all the levels of triggers.

The Level-1 trigger

For L3, the level-1 trigger decision was made for every beam crossing. Thus, it had to be done within 22 μs (11 μs in 8 bunch mode). Once a positive decision was made, the subsequent digitization process took $\sim$ 500 μs, which was the dead time of the system. In case of a negative decision, all the electronics were cleared before the next bunch crossing.

A level-1 trigger occurred if one of the following five criteria was met.

- Energy trigger: total calorimeter energy greater than 20 GeV, or energy in the electromagnetic calorimeter greater than 10 GeV, or the energy in the barrel region of both the BGO and HCAL above 15 GeV, or a BGO cluster with an energy above 1 GeV which accounted for at least 80% of all the ECAL energy was found (single photon trigger), or a cluster in the ECAL or HCAL of at least 2.5 GeV, close in ϕ to a TEC track (cluster trigger).

- TEC trigger: at least two tracks with transverse momentum $p_T > 100$ MeV (for $28^o < \theta < 37^o$, $143^o < \theta < 152^o$) or $p_T > 150$ MeV (for $37^o < \theta < 143^o$), and with a separation greater than 120^o in the transverse plane.

- Scintillator trigger: at least 5 out of the 30 scintillator counters were hit within 30 ns of a beam crossing, where the hits were well separated.

- Muon trigger: at least one muon track in the muon chambers with transverse momentum greater than 1 GeV, measured by at least 2 out of 3 P chambers, and 3 out of 4 Z chambers.

- Luminosity trigger: a small angle Bhabha scattering identified by the luminosity monitor

The Level-2 trigger

The L3 level-2 trigger checked those events that passed only one level-1 selection criterion. By using more data available at this time and analysing information from more than one sub-detector, the level-2 trigger could reject calorimeter triggers arising from electronic noise and some of the TEC triggers generated from beam gas, etc.

The Level-3 trigger

The L3 level-3 trigger used all of the digitized data for an event, so it had finer granularity and higher resolution compared to the level-1 and level-2 triggers. As in level-2, the level-3 trigger checked those events with one level-1 trigger only, using more complicated algorithms and more stringent criteria. If a positive decision was made on level-3, the event was then written out to tape.

The level-1 trigger rate was about $5-20\ Hz$, and the rate of writing tape was reduced to $1-5\ Hz$ after level-3.

4. Running of the L3 Radiation Monitor

Silicon microstrip detectors for colliding beam experiments can be damaged by high instantaneous radiation rates which may destroy the coupling capacitors in the front-end electronics by a voltage spike, and by long-term cumulative radiation doses which significantly decrease the gain and increase the leakage current of the silicon detector. Therefore, a radiation monitoring system (RM) was built for the silicon microvertex detector (SMD) in L3. It had several functions [55]:

- measuring radiation dose rates and integral doses
- providing alarms if persistent high radiation levels threaten long-term damage
- providing a trigger signal to LEP to dump the beam (within 1 ms) to protect the SMD in the event of exceptionally high instantaneous dose rates.

This chapter describes the radiation monitoring system for L3, which was installed in the L3 detector in April 1993 (sensors and the monitoring system) and April 1994 (beam dump trigger). The hardware status and running results are also described here.

4.1 Introduction [55]

The main radiation background in the L3 central tracking region came from low-angle (with respect to the beam axis) leptons and photons, such as off-momentum electrons and photons from bremsstrahlung processes in the beam optical elements. To monitor the SMD radiation conditions, the RM sensors were mounted near the inner surface of the L3 Active Lead Rings (ALR), facing the IP. The ALR was installed around the beam pipe in 1991, on both sides of IP, approximately 1 m away, to reduce the background seen in the L3 TEC. Thus the sensors were shielded in the direction away from the IP, and sampled the low angle radiation coming through the SMD from the far side of the beam pipe. Figure 4.1 shows the layout of the RM sensors.

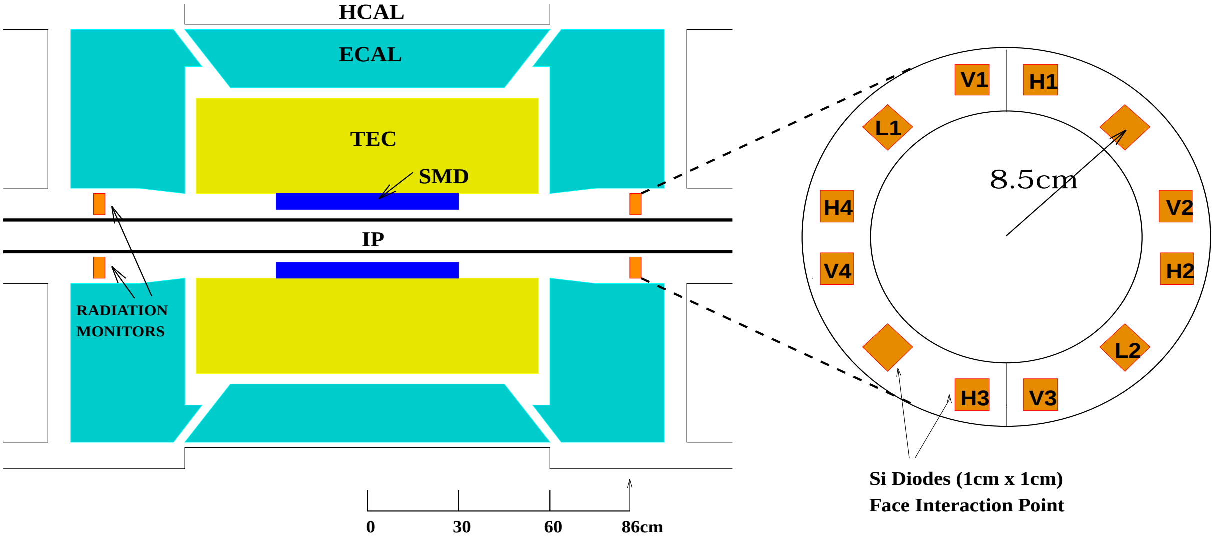

Figure 4.1: The radiation monitor layout in L3 [55].

The RM senors were silicon diodes with a thickness of 600 μm, and size of $1 \times 1\ cm^2$ (Hamamatsu S1723-06). These diodes with the associated amplifiers were calibrated at CERN with a very strong radiation source, which covered dose rates from $0-170\ rad/h$, and showed excellent linearity of response (see Figure 4.2). Twelve of these silicon diodes were mounted on each side of the SMD in front of ALR, 86 cm from IP. The diodes were located 8.5 cm from the beam axis. Ten silicon diodes from each side were used and connected to the amplifiers.

In order to handle the large dynamic range of the radiation signal (from below 1 $mrad/hr$ to over $10^7\ rad/hr$), the amplifiers had three different configurations.

- V-channel (Very High Gain): amplifiers/voltage-frequency converters were connected to four diodes on each side of the SMD (shown as V1 - V4 in Figure 4.1). The frequency signals from these amplifiers were sent to scalers and then monitored by the L3 online VAX cluster. The data from these channels were used for online monitoring, and integrated dose calculation, and to produce an alarm in case of high radiation level for a long period of time. The V-channels covered a dose rate range from 1 $\mu rad/s$ to 60 $mrad/s$.

- H-channel (High Gain): amplifiers were connected to four diodes from each side of the SMD (shown as H1 - H4 in Figure 4.1). Signals from these channels were used for high dose rate monitoring and to provide the LEP beam dump trigger and a PC based DAQ system trigger. The H-channels covered a dose rate from 6 $mrad/s$ to 18 rad/s.

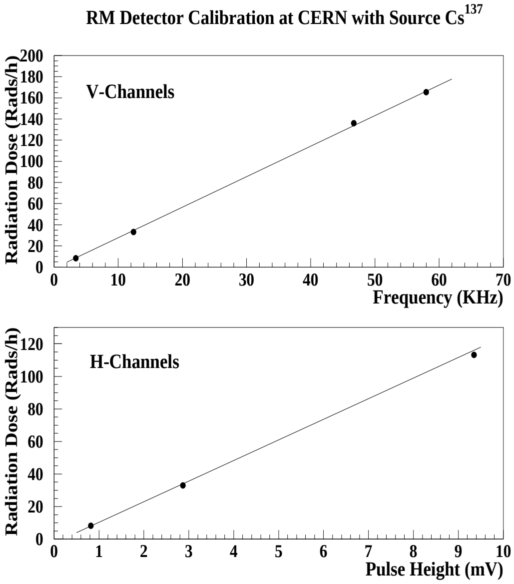

Figure 4.2: Detector calibration using a ${}^{137}Cs$ source at CERN [55].

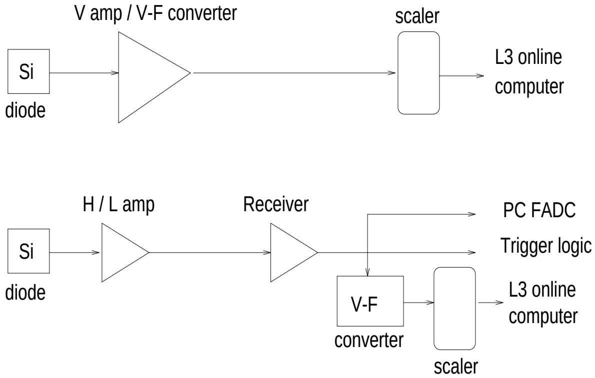

Figure 4.3: Signal routes from the V and H/L channel silicon diode detectors [55].

- L-channel (Low Gain): amplifiers were connected to two diodes on each side of the SMD (shown as L1 and L2 in Figure 4.1). The L channel signals were used to measure extremely high radiation spikes which could saturate the H-channel amplifiers. The dose rate range covered by the L-channels was from 1.33 rad/s to 6 $krad/s$.

A schematic plot of the data flow from the V and H/L channels is shown in Figure 4.3. The signals from the sensors were used for three purposes:

- Online Monitoring: including a radiation level display in the L3 control room, warning message generation for a continuous high radiation level, and calculation of the integrated radiation dose. For this purpose, signals from all three channels were used continuously through a voltage-frequency converter/scaler path, and handled by the L3 online VAX cluster.

- Beam Dump Triggering: a fast beam dump trigger was provided to LEP if a dangerous radiation level lasted for a certain period of time. Two independent trigger logics were implemented based on the H and L channel signals respectively, and will be discussed in Section 4.2.

- Spike recording: since the H and L channels amplifiers were chosen to have a short time constant (about 100 μs), it was possible to study the pulse shape of rapid intense radiation fluxes occurring typically during beam injections, beam adjustments or beam losses, and to determine by what kind of beam condition the dump was triggered. This was done by sending the H and L channel signals to a PC based flash-ADC for waveform recording. Its trigger logic will be discussed in Section 4.2.

4.2 Trigger and data acquisition

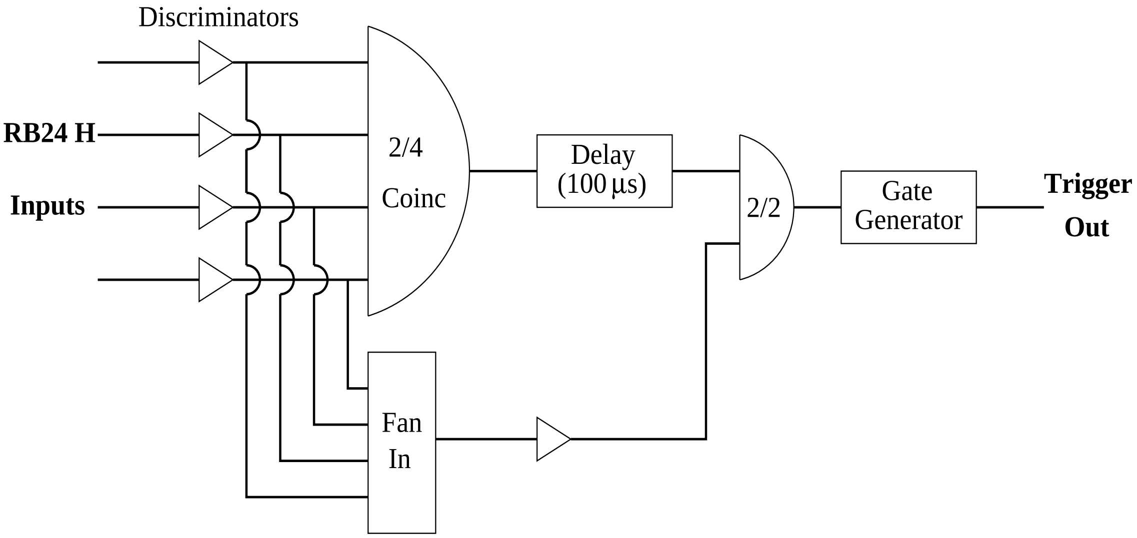

Figure 4.4: Trigger logic for the PC DAQ system [55].

The trigger schemes for the PC DAQ and beam dump were very similar. The differences were the input channels and the threshold, the coincidence level, and the delay time settings. A schematic diagram of the PC DAQ trigger logic is shown in Figure 4.4. The data acquisition through the L3 online cluster and the PC system also is discussed in this Section [55].

Trigger for PC DAQ system

As shown in Figure 4.4, the trigger inputs were the 4 H-channels from one side of the L3 detector (RB24 side). In order to record high radiation rate spikes, the discriminators were set to latch mode, and the threshold was set to a voltage equivalent of 150 $mrad/s$; that was rarely reached by a continuous radiation level. To reduce triggering by very short spikes and noise, the trigger required at least two out of the four input channels to exceed the discriminator threshold, and to last for at least 100 μs. The typical trigger rate during stable LEP physics running was typically $1/week$, and it was much higher during calibration runs at the Z^0 peak and during machine development.

Trigger for LEP beam dump

There were two separate beam dump trigger logics for L3, the low threshold trigger and the high threshold trigger. Both provided a fast beam dump signal when dangerous radiation level occurred. The low threshold trigger fired if at least 2 out of the 4 H-channels from either side (RB24 or RB26) were above 6 rad/s for at least 300 μs. In addition, it required the SMD bias voltage to be on. The trigger electronics was the same as the one shown in Figure 4.4, except for the input channel used, and a final 2/2 coincidence with the SMD bias. The high threshold trigger took the two L-channels from each side of the detector as the input, and required two out of the four channels to exceed 600 rad/s for at least 300 μs. This trigger didn't require the SMD bias to be on, and had the same electronics as the one shown in Figure 4.4, except for the input channel used.

Data acquisition

The RM DAQ included continuous recording of the radiation level with the L3 online cluster and a spike spectrum recorded with a PC based system.

The online VAX cluster read and recorded the output of the RM scaler every 10 seconds, applied a pedestal subtraction and a noise veto cut. The current radiation dose was then calculated and displayed in the L3 control room. If the dose level exceeded 1 rad/h, or the dose accumulated during a high radiation period exceeded 500 $mrad$, a warning message was issued on the run control screen. The L3 shift leader reported this warning to the LEP control room. The integrated radiation dose suffered by the L3 vertex detectors was also calculated based on this sampling at 10 second intervals.

The PC DAQ system was built with two National Instruments Waveform-ADCs. One was EISA A2000, which had four channels that could support up to a 1 MHz sampling rate. The four channels on this board were connected to the four H-channels from RB24 side, which was the same side as those used by the PC DAQ trigger. The other board was an AT-MIO-16F-5, which had up to 16 channels and a 200 KHz sampling rate. Eight waveform ADC channels were used to record the H-channels from the RB26 side and the L-channels from both sides. The EISA card worked at 200 KHz and the signal spectrum was recorded for 10 ms (2000 counts) per channel. The AT card worked at 15 KHz and the recording time was 33.33 ms (500 counts) per channel. Both cards were triggered by the PC DAQ trigger described above. In order to have a complete record of high radiation spikes, both cards held some counts (1000 counts/5 ms for the EISA board and 150 counts/10 ms for the AT board) prior to the trigger. An example of a recorded radiation spike is shown in Figure 4.5. The signals from the H-channels on the RB24 side were recorded by the EISA board, and the others were recorded by the AT board. The red line in the H-channel plots indicated the equivalent radiation level of the lower threshold beam dump trigger, and that in the L-channel plot was the radiation dose rate of the higher threshold trigger. This event clearly satisfied the lower threshold trigger requirements and fired the LEP beam dump trigger. The plot shows that the LEP beam was dumped after about 2 ms. This event was recorded on July 19, 1999, during LEP beam acceleration. The high radiation level was due to a LEP power converter trip.

4.3 Hardware status

The L3 radiation monitor was first installed in 1993, and ran until the end of LEP in 2000. During this time, the hardware configuration was changed a few times. The following list gives a brief history of the hardware configuration [55, 56, 57, 58]:

- The L3 radiation monitor was installed before the LEP running period in 1993. It operated as a monitoring device during that year. The L3 online cluster read signals from the V-channels only. The H and the L-channel signals were recorded by the PC DAQ system.
- Before LEP running in 1994, the H and L-channels were upgraded with voltage/frequency converters, and the L3 online cluster was able to record all RM channels.
- Also in spring 1994, the lower threshold beam dump trigger for LEP machine was installed. This trigger was designed to protect the SMD coupling capacitors, and required the SMD bias to be 'ON' in the trigger logic.
- In September 1994, the higher threshold beam dump trigger was installed. This was to protect the L3 SMD and other detectors from extremely high radiation spikes during the extensive LEP machine development runs. It was in this year that LEP started boosting its energy from 91 GeV. This trigger did not require the L3 SMD bias to be 'ON.'
- In July 1997, the higher threshold beam dump trigger was removed, due to a hardware shortage (part of the lower threshold trigger was broken) and the fact that this trigger rarely fired after its

installation in the end of 1994. The impact of removing this trigger will be discussed in Section 4.4.1.

- Also in July 1997, the trigger of the PC DAQ system was slightly modified so that both the original PC DAQ trigger and the LEP beam dump trigger would start the waveform recording. This was due to the fact that the original PC DAQ trigger took the four H-channels from the RB24 side. In some rare cases, the radiation level on the RB24 and the RB26 sides was extremely asymmetric. If the radiation level on the RB26 side was high enough to trigger the beam dump but that on the RB24 side was too low to trigger the PC DAQ, the waveform of the radiation spike was not recorded even if it dumped the LEP beam. This modification was to make sure that at least the beam dump events were recorded.

- On July 24, 1997, the radiation level threshold for the lower threshold beam dump trigger was changed from 21 $krad/hr$ to 42 $krad/hr$, by adding attenuators to lower the H-channel input signals. This was due to the high radiation level of the LEP Z^0 run during July, 1997. The original threshold caused too frequent beam dumps. After installing the attenuators, the beam dump trigger stopped firing even a single trigger.

- On September 11, 1997, the power supply of the trigger electronics was replaced due to a problem with the 6 V output.

- On August 31, 1998, the attenuators were removed from the beam dump trigger system, and the original trigger threshold of 21 $krad/s$ was restored. This was due to a suspicious behavior of the beam dump trigger: it didn't fire a single trigger since the attenuators were installed. A later test showed that there was a problem with the attenuators; their output could never reach the threshold of the trigger discriminators no matter what the input, and they thus killed all beam dump triggers. The trigger worked well after the attenuators were removed. The first beam dump trigger after removing the attenuators fired on September 3, 1998.

- On July 16, 1999, the power supply of the trigger electronics was replaced again, due to a problem with 6 V output. There was a 50 Hz component in the 6 V DC output, which caused modules to give fake triggers.

- One channel on a LRS365AL (4-fold logic unit) module used as a 4/1 coincidence in the trigger electronic was broken. It randomly lost 20% output signals. The function of this channel was replaced by a LeCroy 622 module on May 17, 2000.

- The other channel on the same LRS365AL module was broken, and it randomly generated beam dump triggers. It was replaced on August 8, 2000.

In summary, except for a few trigger module and power supply failures, the L3 radiation monitor system, both the sensors and triggers, worked reliably to protect the vertex detectors and to monitor the radiation dose throughout LEP running.

4.4 Results

Besides the fast beam dump trigger, which provided the L3 vertex detectors real time protection, the radiation monitor system also provided continuous monitoring of the radiation level in the vertex region and detailed tracking of high radiation level spikes, including every spike that caused a LEP beam dump. The daily radiation dose, integrated radiation dose for the year and the waveforms recorded by the PC DAQ system for high radiation spikes, were published on the web every week during LEP running in 1999 and 2000.

4.4.1 Beam dump triggers

The beam dump trigger was installed before the 1994 LEP running. The beam dump trigger events during LEP running from 1994 to 2000 are summarized bellow [56, 57, 58, 59].

The beam dump triggers can be divided into four categories:

- category **a** and **a***: events involving a catastrophic beam loss in the vicinity of the L3 detectors are denoted as category **a**. Among category **a** events, those that had high enough instantaneous radiation level to trigger the high threshold beam dump trigger are further denoted as **a***. The beams were already lost by the time when the dump trigger fired, so the trigger could not be used to protect L3 in this case, and the radiation dose is usually high in these events. Due to the beam being totally lost, the instantaneous radiation level was the highest among all categories, and was usually the only category that might be seen by L-channels. A typical category **a** event is shown in Figure 4.6, and this is also an **a*** event.
- category **b**: events involving decaying beam conditions over a few milliseconds. The radiation dose rate increased rather slowly in this kind of event, and the beam dump trigger usually fired

during the build-up of the radiation spike, and thus was able to prevent potential damage of the detectors. This class of events was what the original design of RM aimed at. A typical category **b** event is shown in Figure 4.7.

- category **c**: events involving relatively short (about $1-2\,ms$) radiation spikes. These events could be due to unsuccessful injection or instabilities during a fill. The high radiation level caused by the spikes normally lasted no more than 2 ms. Since the time delay between the moment the radiation level crossed the trigger threshold and the actual beam dump occurred was about 2 ms, the spike was usually finished by the time of the actual beam dump. Due to the fact that this kind of spike often came in groups spaced by only a few milliseconds' interval, the beam dump was effectively able to reduce the radiation dose received. The radiation level and dose of these spikes were normally small, but occasionally caused a visible signal in the L-channel. A typical category **c** event is shown in Figure 4.8.
- category **d**: fake beam dump triggers. Fake triggers had two sources. One was the spikes in the DC power supply of the crate which hosted the trigger electronics. This happened a few times when the crate was turned on or turned off. After noticing this effect, fake triggers from this source were totally prevented. The other source was trigger hardware failure, which happened only a few times during 7 years of running.

The beam dump trigger events in each year are shown in Table 4.1, with the events sorted into the categories described above. Since a detailed record in 1997 is not available, events in that year are not sorted.

If we sort the high radiation level events (those that triggered PC DAQ or beam dump) by the

Year	beam dump events	category **a** (**a***)	category **b**	category **c**	category **d**
1994	3	1 (1)	0	1	1
1995	30	10 (3)	4	14	2
1996	19	1 (1)	10	7	0
1997	30	- (-)	-	-	-
1998	3	1 (1)	2	0	0
1999	14	5 (2)	7	1	1
2000	10	4 (1)	0	5	1

Table 4.1: Beam dump events during 7 years of running of the L3 radiation monitor.

LEP status, we find that they occurred during LEP filling, acceleration/RF adjustment and physics (colliding beam). And the problems that caused these high radiation level events included RF power converter trip, bending magnet ripple, quadrupole quench, beam kicker magnet fault and L3 support tube motion, etc. A breakdown of the recorded events according to LEP status is shown in Table 4.2, for 1999 and 2000.

There is another way to describe the LEP running status: according to its running purpose. In this way, LEP2 running had three modes in each year: Z^0 run, physics run and machine development. Z^0 runs provided calibrations for both the LEP machine and all the LEP detectors, so all the detectors took data during this mode. Physics runs were the main data taking period at high energies. Machine development was reserved for LEP machine study, all detectors were turned off during this mode. So the bias voltage of the L3 SMD was always on during Z^0 runs and physics runs, and was always off during machine development periods. This was crucial to understand the impact of removing the high threshold beam dump trigger in 1997.

If we compare the trigger logics of the high and low threshold trigger, their differences are as follows: first, the threshold, and second, the requirement on the SMD bias voltage. The low threshold trigger required the SMD bias to be on, while the high threshold trigger did not. So the low threshold trigger covered all the high threshold triggers when the SMD bias was on, and missed all the high threshold trigger events when the bias was off. We can conclude that during LEP Z^0 runs and physics runs, removing the high threshold trigger did not have any impact: all high threshold trigger events were also triggered by the low threshold. These are the $\mathbf{a}^*$ events among those in category **a**. We missed some triggers during machine development after removing the high threshold trigger, but we still knew what we missed from the PC DAQ record. Fortunately, there was only one such event recorded, during the LEP machine study (131/90 degree optics) on September 7, 1998. The peak radiation dose rate reached 10^7 rad/hr.

Year	events	filling LEP	acceleration	physics
1999	16	2	6	8
2000	20	15	5	0

Table 4.2: High radiation level events: breakdown according to LEP status.

4.4.2 Daily and yearly integrated radiation dose

The daily and yearly radiation doses received by the L3 central detectors were published on the Web every week during LEP running. The integration was done on the L3 online cluster by using information from the L, H, and V channels of the radiation monitor. The integration sampling interval was 10 seconds. Figures 4.9 and 4.10 show the daily radiation dose during 1999 and 2000 LEP running, and the total integrated dose of the year as a function of the number of running days. The high daily rates came both from very high radiation level spikes, and integration of rather low radiation dose rates that lasted for hours.

Figure 4.11 shows the yearly integrated radiation dose as a function of LEP running days, for all years after the installation of the L3 radiation monitor.

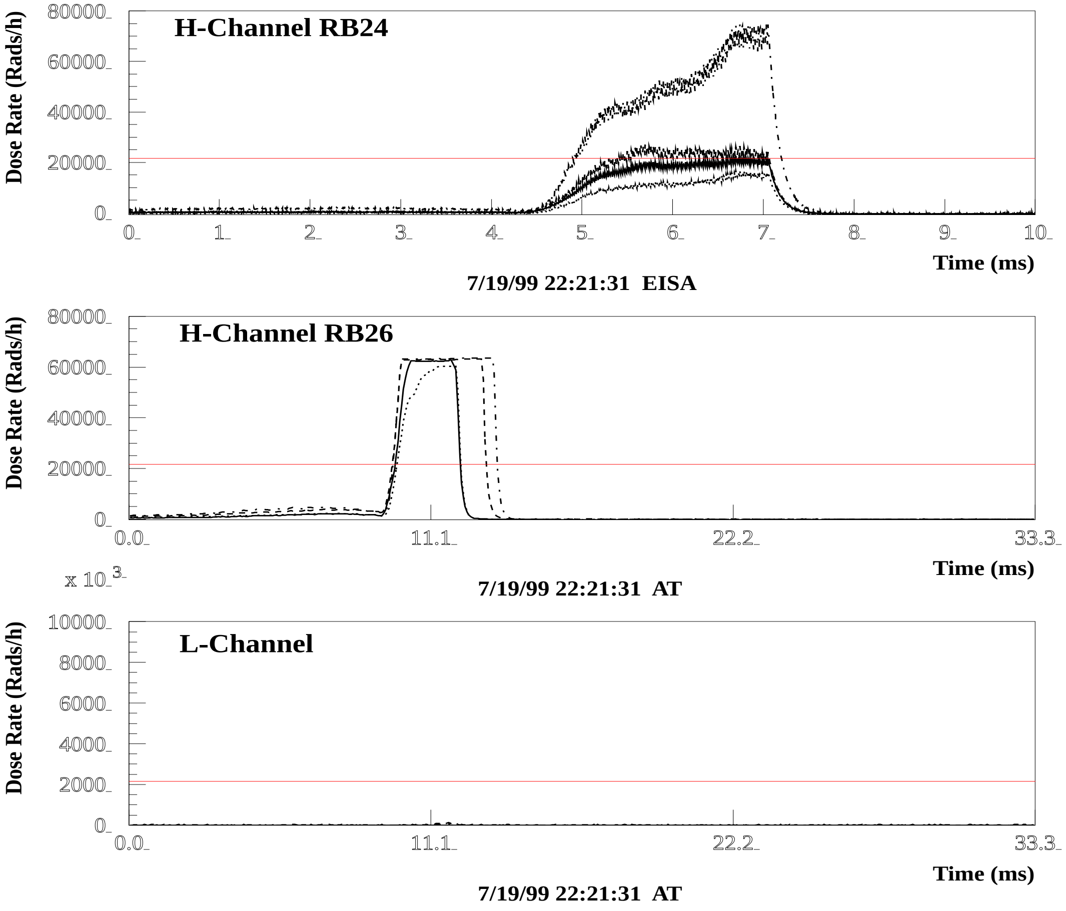

Figure 4.5: A high radiation level spike recorded by the PC DAQ system. The H-channels from the RB24 side were recorded by the EISA card, which recorded a 10 ms waveform including 5 ms pre-sampling. The H-channels from the RB26 side and L-channels from both sides were recorded by the AT card, which recorded 33.33 ms of data including 10 ms pre-sampling.

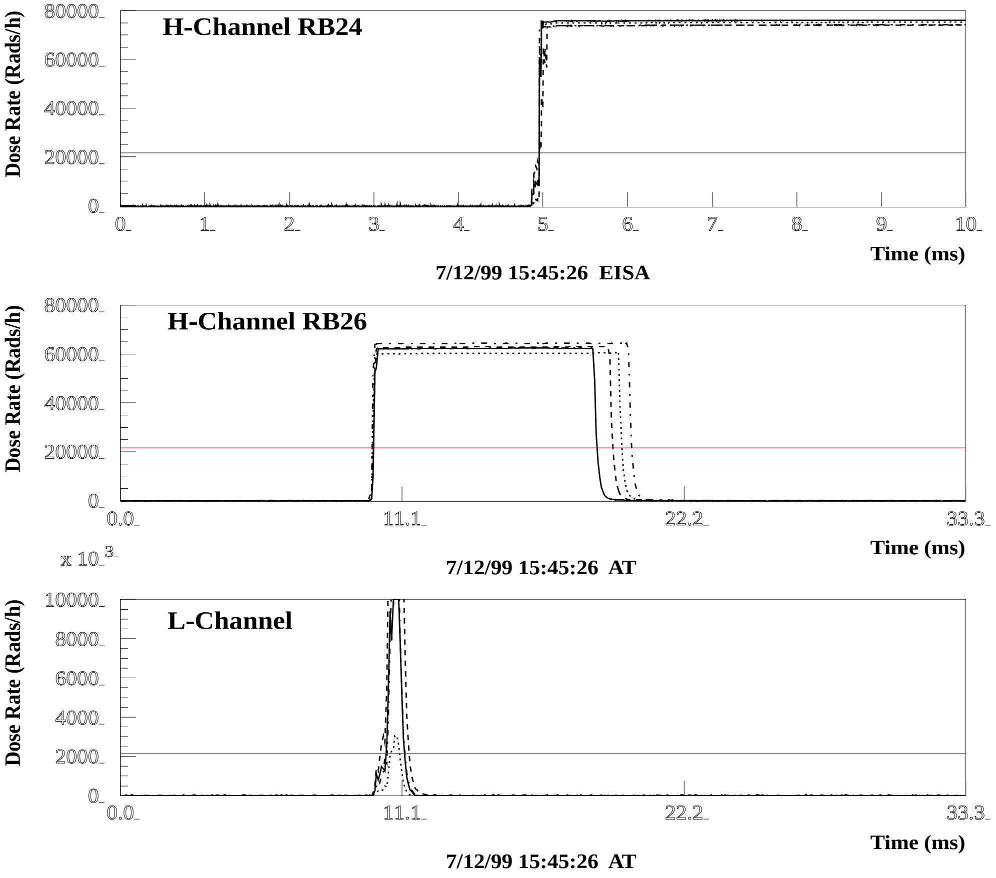

7/12/99 15:45:26 EISA

7/12/99 15:45:26 AT

7/12/99 15:45:26 AT

Figure 4.6: The waveform of a typical category **a** event (this is also an **a*** event).

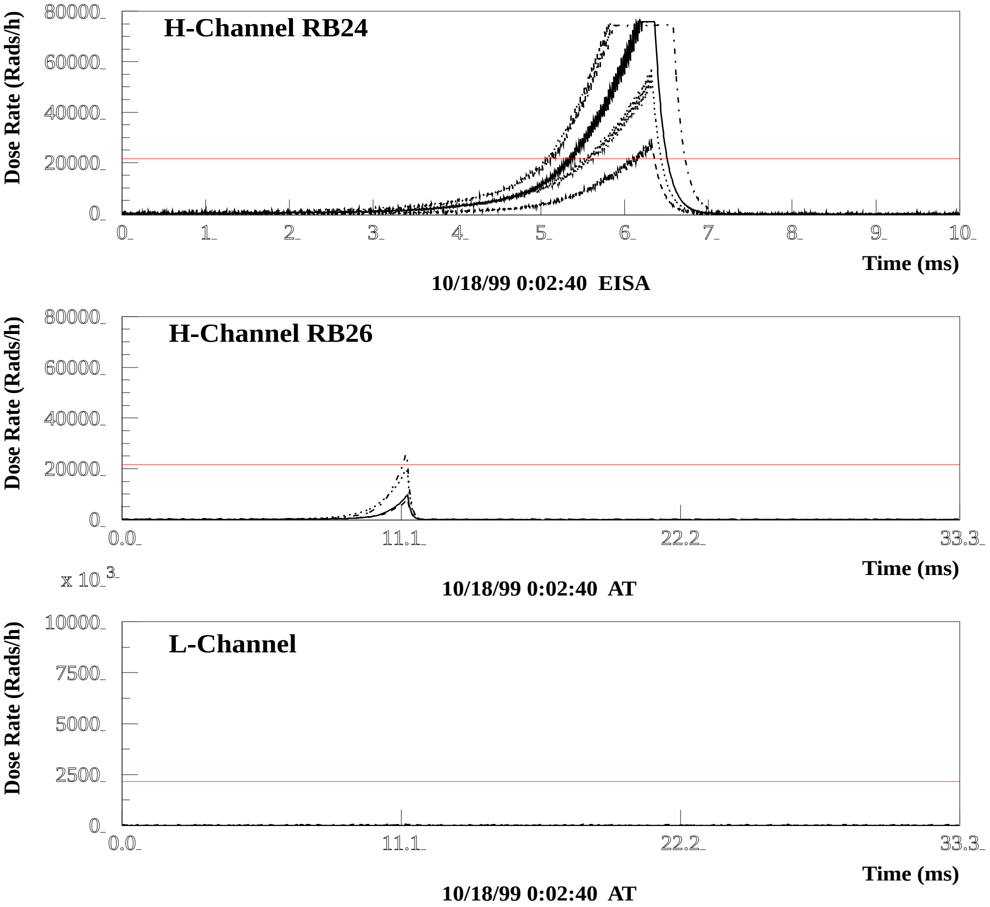

Figure 4.7: The waveform of a typical category **b** event.

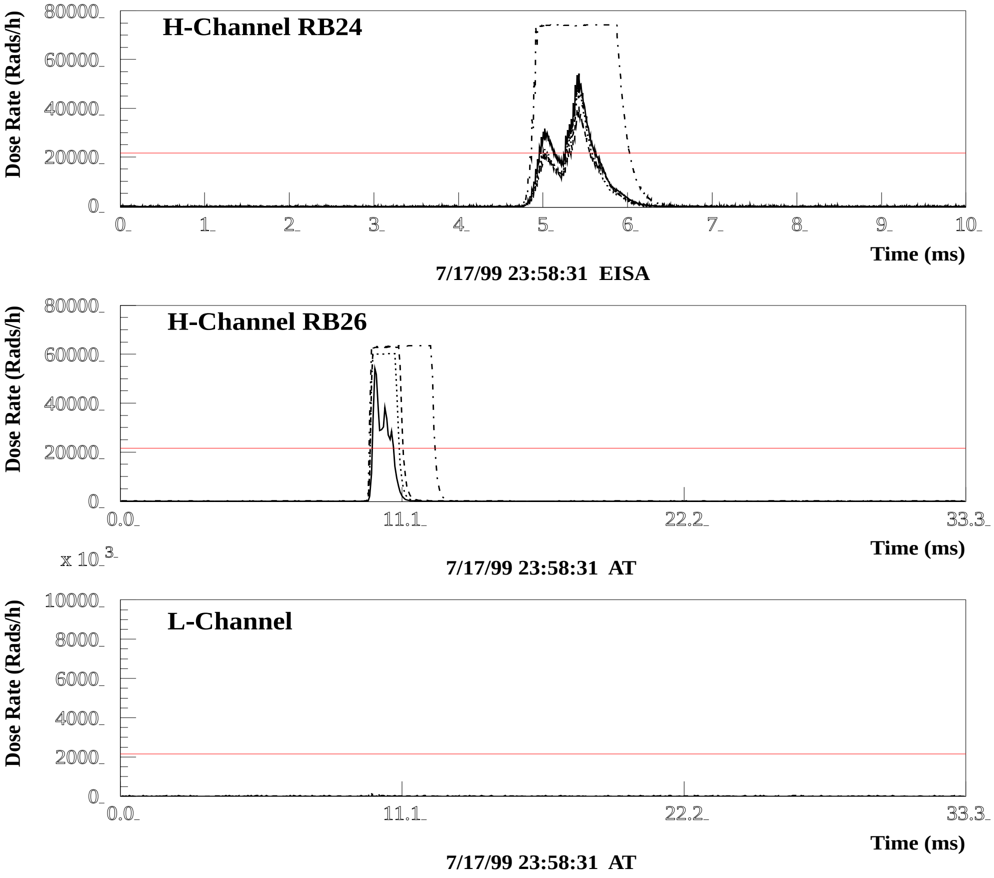

Figure 4.8: The waveform of a typical category **c** event.

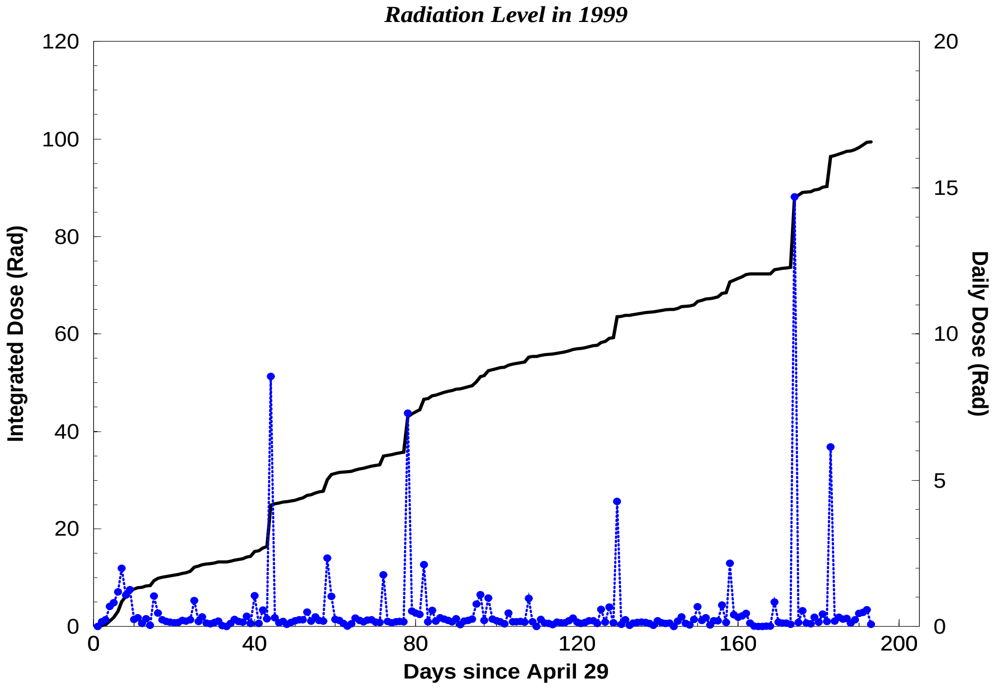

Figure 4.9: Daily and integrated radiation dose received by the L3 central detectors, during the 1999 LEP running.

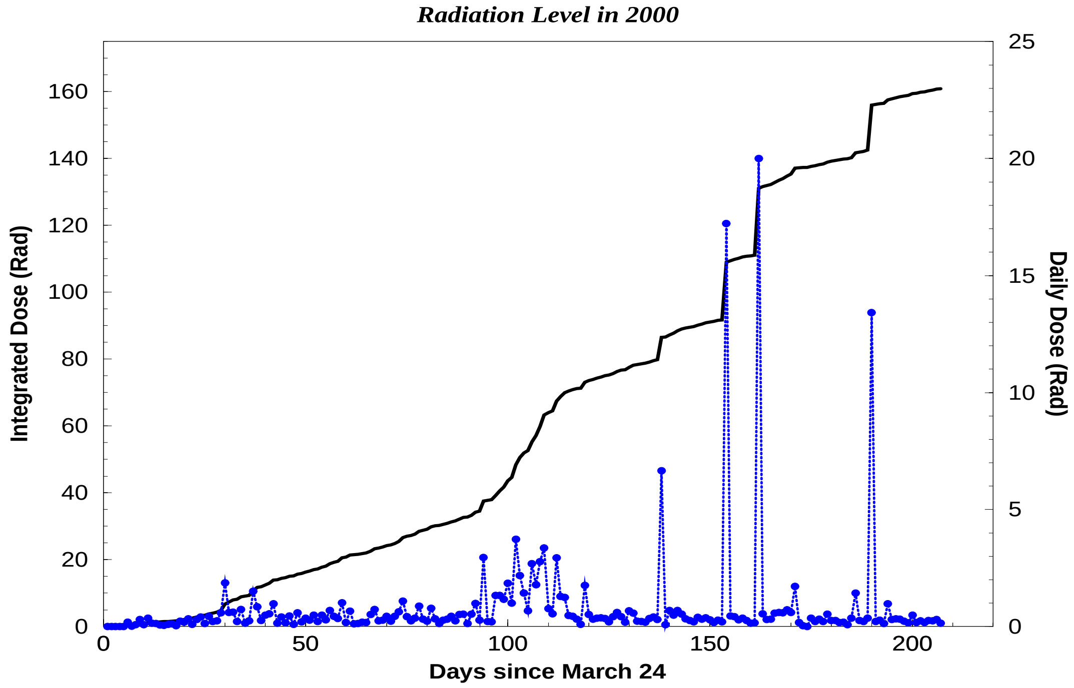

Figure 4.10: Daily and integrated radiation dose received by the L3 central detectors, during the 2000 LEP running.

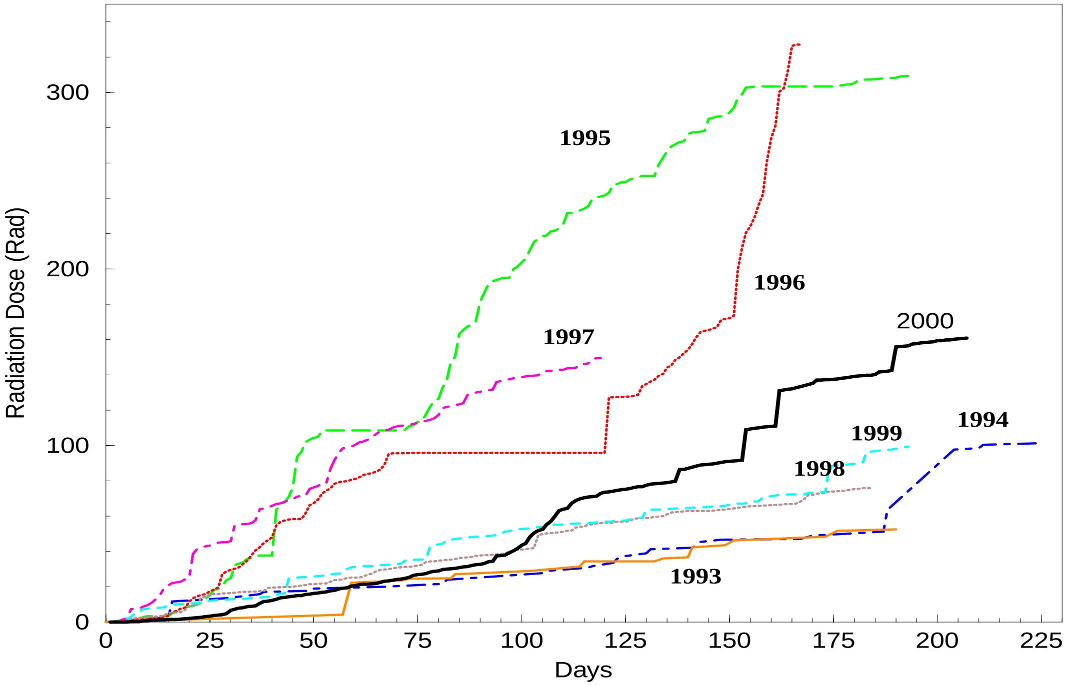

Figure 4.11: Yearly integrated radiation doses for the entire running period of the L3 radiation monitor.

5. Monte Carlo Simulation and Event Reconstruction in L3 Analysis

This chapter discusses the data processing and Monte Carlo simulation procedures in the L3 experiment, with special emphasis on those issues that concern the scalar lepton searches. To handle the possible long-lived scalar leptons, some improvements on the standard L3 simulation and reconstruction program have been done. Section 5.1 gives an overview of the L3 offline analysis, Section 5.2 discusses the simulation of charged particles with visible decay length, and Section 5.3 addresses the dE/dx simulation problem in the L3 TEC that was solved in the course of my analysis.

5.1 Introduction

The data processing and Monte Carlo event generation are controlled by a dedicated production group, using pre-developed L3 standard program packages. All the data goes through a reconstruction program, which converts the recorded detector signals into physics quantities that are useful for analysis. Monte Carlo events are produced as sets of four vectors by generators of various physics processes, based on theoretical calculations. The generated events are passed to a simulation program based on the CERN Geant package [63]. The simulation program then traces all the particles in the event and simulates the detector response along the paths of the particles. The Monte Carlo events are then digitised and are subsequently treated just like real data, and passed to the reconstruction program [60].

Processing of L3 data

Formal processing of L3 data follows these steps:

- Reading and decoding the recorded data from the L3 online data acquisition system.
- Reconstruction at sub-detector level. Individual objects in sub-detectors, such as TEC tracks, calorimeter bumps[1], muon tracks, etc., are constructed from individual hits.

---

[1] Localized maxima in the energy deposition pattern in the calorimeters.

- Global reconstruction using the individual objects from the previous step, to represent as accurately as possible the individual particles that pass through the L3 detector, and to calculate physics quantities.

REL3 is the L3 standard software package that takes care of all the phases of event reconstruction. It decodes all the data from the L3 detectors and stores them in the form of ZEBRA banks. The individual data objects at this stage are digitized 'hits' in different sub-detector components. Calibration corrections are also applied at this phase, using information stored in the DBL3 database.

After decoding the raw data, reconstruction in the L3 sub-detectors takes place. At this stage, information on hits in the active elements in each sub-detector is combined under the control of REL3, and the higher level data objects are constructed. The program divides the L3 detector into several parts, namely the TEC, scintillators, BGO, HCAL, MUCH, etc. The data objects produced at this phase are clusters of energy deposits in the calorimeters and tracks in the tracking chambers.

These data objects from sub-detectors are further combined in a global reconstruction by the AXL3 package, still under the control of REL3. In this level of reconstruction, the relationship among sub-detector objects is established. BGO bumps and HCAL clusters are matched according to their angular position, and matched TEC/SMD tracks are also associated. Characteristic MIPs (minimum ionizing particles) in the HCAL are also identified, and associated with matched muon tracks. At this stage, the globally reconstructed objects are individual particles 'seen' with their finite resolution.

Processing of L3 Monte Carlo events

The processing of L3 Monte Carlo events follows these steps:

- Generation of the four vectors arising from physics processes in e^+e^- collisions, using theoretically calculated event generators.

- Tracking the particles in generated events, and simulating the detector response to these particles along their paths.

- Simulating the L3 data acquisition system, digitizing the detector response and producing records for Monte Carlo events in the same format as real data.

- Reconstruction of the Monte Carlo events, performed using exactly the same programs and steps of processing as real data.

Monte Carlo events are generated process by process, using one of many generators written for an individual process, or a class of physics processes, in e^+e^- collisions. Many generators are based on theoretical calculations of real physics processes with the help of measurements in previous experiments to resolve some issues, while there are some other generators that try to produce possible new physics processes distributed according to theoretical predictions. The generated events are stored in a standard format, no matter which generator was used, so that they can be passed to the L3 simulation program easily.

The standard L3 detector simulation program is called SIL3, and is based on the GEANT package. SIL3 tracks all the particles in an event produced by the generator as they go through each sub-detector layer of L3, simulates the detector response, digitizes the detector hits, and produces raw data records just as the L3 DAQ system does. The data format is exactly the same as the real data taken during LEP running.

Simulated Monte Carlo events are then passed to REL3 for reconstruction. This process is done in exactly the same way as for real data, except some information is saved about the event at the generator level, for convenience in checking some aspects of the data analysis. For historical reasons, a very small part of the detector simulation code which was developed separately was embedded into REL3, instead of SIL3. One such simulation is the pulse height of the TEC wires which provides a measure of the ionization of tracks, and is used to calculate the dE/dx of TEC tracks.

Although the simulation and reconstruction programs, SIL3 and REL3, have proven to be efficient and effective for physics processes from the Standard Model, as well as for a wide range of processes predicted by hypothesized new theories, there are still processes that they cannot handle. In this case, a careful study and upgrade of the programs is necessary. In Sections 5.2 and 5.3, two problems with the simulation and reconstruction of new physics processes that occurred in this analysis are discussed, and my solution is presented.

5.2 Simulation of particles with long lifetime

The SIL3 program tracks all the particles in a generated event through the L3 detector until one of the following happens: the particle flies out of the L3 detector, the particle stops in the detector, or the particle decays in the detector. When the particle decays, SIL3 then tracks all the decay products. Particle decay is an important issue here during particle tracking. It is a convention that the Monte Carlo generators handle all the particles with short lifetime, calculating the secondary vertex, determining the decay mode and generating the decay kinematics, and leave stable and long lived particles to the simulation program. Here particles with short lifetime refer to those which decay well before they reach any detectors, such as $W^{\pm}$, Z^0, $\tau^{\pm}$, etc. Excluding these particles, SIL3 was designed to handle only known (Standard Model) stable particles and those with long lifetime, namely photons, electrons, muons, neutral hadrons and charged hadrons.

This scheme works well for all known (Standard Model) particles, but a problem arises when new particles are introduced. Here "new particle" refers to those predicted by theory but not yet found, such as SUSY particles. The reason for the problem is twofold. On one hand, since various theories predicted many interesting new particles, it is not practical to implement all of them in the simulation program. So these particles are handled by each individual generator, which takes care of all the new particle decays, no matter if it is short lived or long lived. On the other hand, SIL3 expects that all generator level particle decays have very short decay length, and so it does not track the decaying particles at this level. So the generator and simulation programs together would lose the signals from the decaying new particles, even though they should be visible for the detectors.

To understand this problem, we first discuss the details of particle tracking in SIL3, and then a few possible solutions will be mentioned here. In particular, the solution for long lived $\tilde{\tau}$ simulation, which is crucial for the analysis described in this thesis, is discussed in more detail.

5.2.1 Particle tracking in SIL3

The particle tracking in the SIL3 program is shown in the flow diagram in Figure 5.1. The SIL3 program starts with an initialization process, and then starts reading in the generated Monte Carlo events from generators. The output file of the generators has a standard format, and we call it an EGL3 file since it has the file extension '.egl3'. The EGL3 files give a list in each event of all particles that appear in the event, including beam particles (e^+e^-), intermediate particles (such as γ, Z^0 in Bhabha scattering) and final state particles. The record for each particle includes its type, 4-momentum, and the coordinates of the vertex where this particle was generated. The subroutine GTREVE controls the whole process of reading in Monte Carlo events from an EGL3 file and performing the simulation. It loops through all of the event, calls the routine GLTRAC to get all the particle information in a particular event, and calls the routine GUTREV to trace all the particles and do the simulation.

The subroutine GLTRAC is called for each event by GTREVE. It loops through all the particles of that event. The records of the particles are stored in a stack structure, named JSTAK. GLTRAC reads

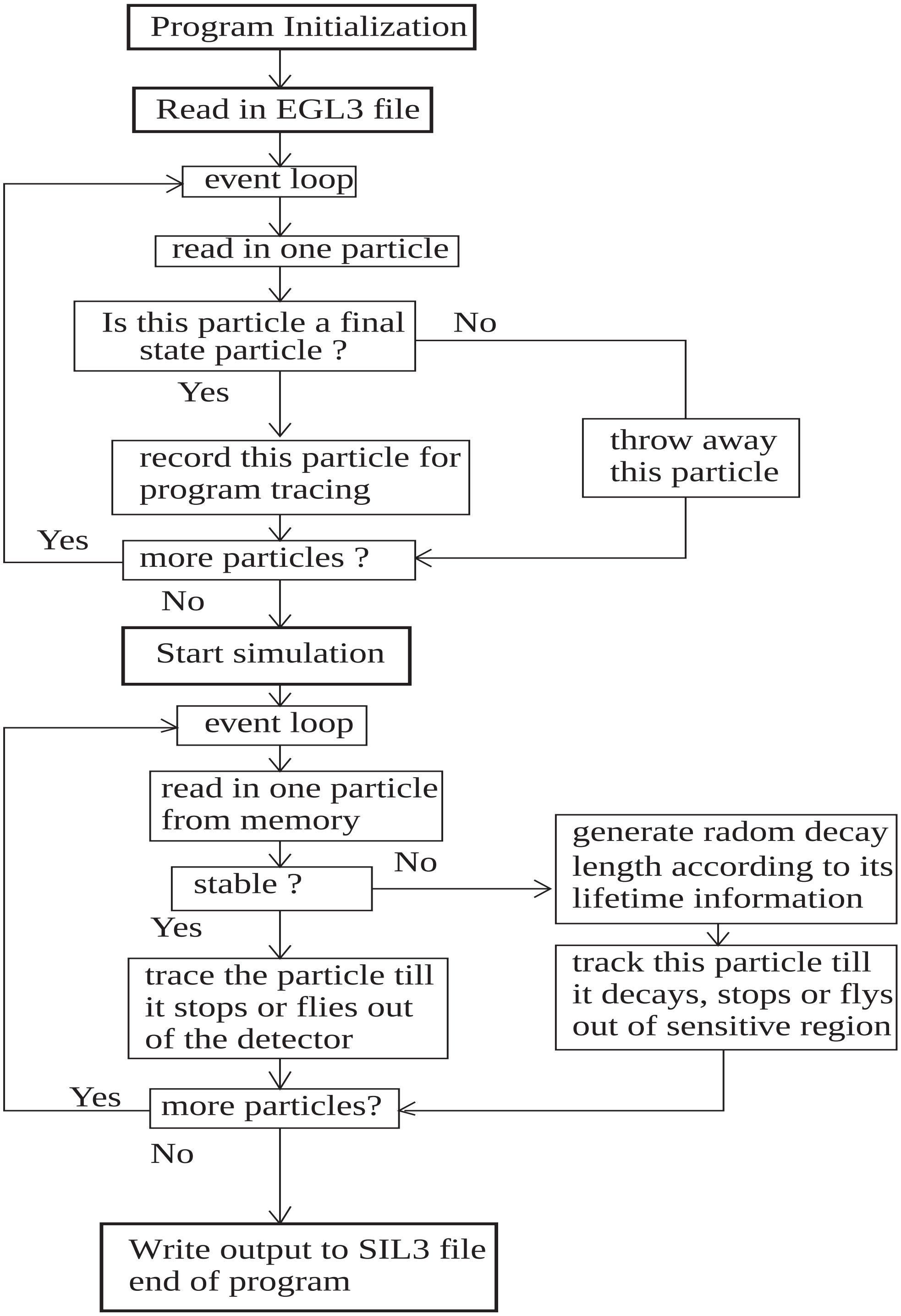

Figure 5.1: Flow diagram of the SIL3 package.

in records from the stack, calculates the kinematics of the particle and stores appropriate information into several common blocks (GCTRAK, GCKINE and GCVOLU). These common blocks are used by the routine GUTREV during the simulation phase. GLTRAC does not store all the particles in an event. It throws away all beam particles and intermediate particles. Based on the convention that only fast decaying particles are decayed by the generator, GLTRAC also throws away mother particles in these decays and keeps only their children. So if a new particle is decayed by the generator, its record will be lost here, and it won't be passed to the tracking routines.

The subroutine GUTREV is called by GTREVE for particle simulation in an event. It then calls the routine GTRAK to trace all the particles. Since all the fast decaying particles decayed at generator level, GTRAK handles only 5 types of particles: photons, electrons(positrons), muons, neutral hadrons and charged hadrons. It calls 5 particular routines to handle these 5 kinds of particles: GTGAMA, GTELEC, GTMUON, GTNEUT, and GTHADR. When tracking a particle, it first decides if the particle is decaying according to its type, if yes, it calculates a random decay length from its lifetime and energy. When the decay length is reached, it provides the decay mode and kinematics and continues to track the decay products. As expected, it handles only the decays from the 5 kinds of particles mentioned above, in particular, not including particles like τ. This is a key point when considering possible solutions for the new particle tracking problem mentioned above, especially when the new particle has a rather complicated decay.

After tracking all the particles, SIL3 writes out the detector response to a standard format file, with the file extension '.sil3'. This file is used in the reconstruction phase as data input.

5.2.2 New particle interface in SIL3

Knowing the problem with new particle decays, it is possible to create an interface to define new particles and their decay modes in SIL3, so that the program will recognize the new particles, know how to trace them and handle their decays. This interface was first done by Gerald Grenier for his analysis searching for Chargino production [61]. The lightest chargino will have a rather long lifetime if it is almost mass degenerate with the Lightest Supersymmetric Particle (LSP). The procedure of creating such an interface is summarized here [62]:

1. Turn off the new particle decay at the generator level. Usually one can either turn off a switch in the generator program, or assign the particle an infinitely long lifetime.

2. Define the new particles needed in routine UTPART in file utl3.car which is part of the standard

L3 analysis package. The way to define particles is provided by the GEANT package, in two routines, GSPART and GSDK. The first routine defines a particle by providing the identification number, name, tracking method, mass, charge, lifetime and a few user defined parameters. The second defines the decay mode for a particular particle ID by giving the branching ratios and decay modes in two arrays. For details on these routines, one can look up the GEANT manual [63].

3. Define the translation between the two particle identification conventions: the PDG code (used in the generator output) and the GEANT code (used in the simulation program, including the new ID defined by GSPART in step 2), in routine UTPCOD of utl3.car.

4. Define the datacards in routine SIDATU of sil3.car, so that one can change the properties of the newly defined particle by supplying a datacard at run time.

5. Re-compile the REL3 package with the updated sil3.car and utl3.car routines.

However, this interface has two problems:

- It cannot handle complicated decays, for example, many-body decays (the GSDK routine can only define up to 3-body decays). And it is not practical if the number of possible decay channels is too large.

- It cannot handle cascade decays if both the mother and the child are unknown to the program and need to be defined by GSPART and GSDK. This seems to be an intrinsic problem of the program.

Our $\tilde{\tau}$ analysis encounters both of the above problems: both $\tilde{\tau}$ and its decay product τ ($\tilde{\tau} \to \tau\tilde{\chi}_1^0$) are not recognized by SIL3, and τ has very complicated decays[2]. So I had to develop a new way to solve the problem with long-lived new particles and their definition in the SIL3 package.

5.2.3 Solution to long-lived particle with complicated decay modes

Given the complications discussed above, it is impossible to solve the problem for $\tilde{\tau}$ by using a program interface alone, one has to get into the details of the tracking program. If we go through the flow

---

[2] Although a standard τ decay library routine is available, which can solve one of the two problems, we cannot use it simply due to the other problem that the SIL3 package cannot handle cascade decays for user defined particles. On the other hand, the interface to implement such a decay library would also be tricky.

diagram in Section 5.2.1 (Figure 5.1), we can see that the $\tilde{\tau}$ will not be tracked by SIL3 since it is identified as a mother particle in a decay at generator level, and is then removed from the tracing list. So if we try to keep $\tilde{\tau}$ in this list and save its decay information from the generator, it is possible to track $\tilde{\tau}$ through the L3 detector using available programs, and to stop the tracking process at the correct position so that it can match the starting point of its decay products.

To get the $\tilde{\tau}$ simulation correct, I made several modifications to SIL3. The modified program is shown in the flow diagram in Figure 5.2. The $\tilde{\tau}$ decay occurs at generator level. The EGL3 file records all the information concerning the decay, both on the children and on the mother of the decay. When SIL3 tries to read the EGL3 file and prepare the particle list for the tracking routines, it first makes a decision if this particle is a scalar lepton. If yes, the particle is put into the tracking list directly. In addition to the standard kinematics recorded in the common blocks GCTRAK, GCKINE and GCVOLU for any particle in the tracking list, the modified SIL3 program also keeps the decay length information for scalar leptons calculated at generator level. When SIL3 starts its tracking phase, it reads through the tracking list and simulates the particle's interactions with detectors along its path. If SIL3 determines the particle being tracked is a decaying particle, it tries to generate the decay length first so that tracking steps won't go beyond that. In the modified version, SIL3 will not calculate the decay length for a particle if it is identified as a scalar lepton, and it will use the recorded decay length from the generator instead. This makes sure that the end point of a scalar lepton exactly matches the starting point of its decay products, which are also produced by generator. Some more changes are made in the program to get this work, including the following:

1. Defining the scalar lepton and its decay mode using the GSPART and GSDK routine, in UTPART of utl3.car. The tracing program for the scalar lepton is a slightly modified GTMUON. The decay mode of the scalar lepton is defined such that its decay products are invisible to the detectors, otherwise there will be two sets of decay products, one from the generator and the other from SIL3. It is not necessary to have a physically meaningful decay mode, but for $\tilde{\tau}$, it is a good choice to use $\tilde{\tau} \rightarrow \tau\tilde{\chi}_1^0$, since $\tilde{\chi}_1^0$ is weakly interacting and τ is not recognized by SIL3 and will simply be ignored.
2. Defining the translation between the PDG code and the GEANT code for particle identification.
3. Defining datacards in the routine SIDATU of sil3.car to pass on the new particle properties.

After these modifications, the correct simulation of a scalar lepton with rather long lifetime has been achieved for the first time in L3. Obviously, this procedure doesn't only apply to the scalar lepton

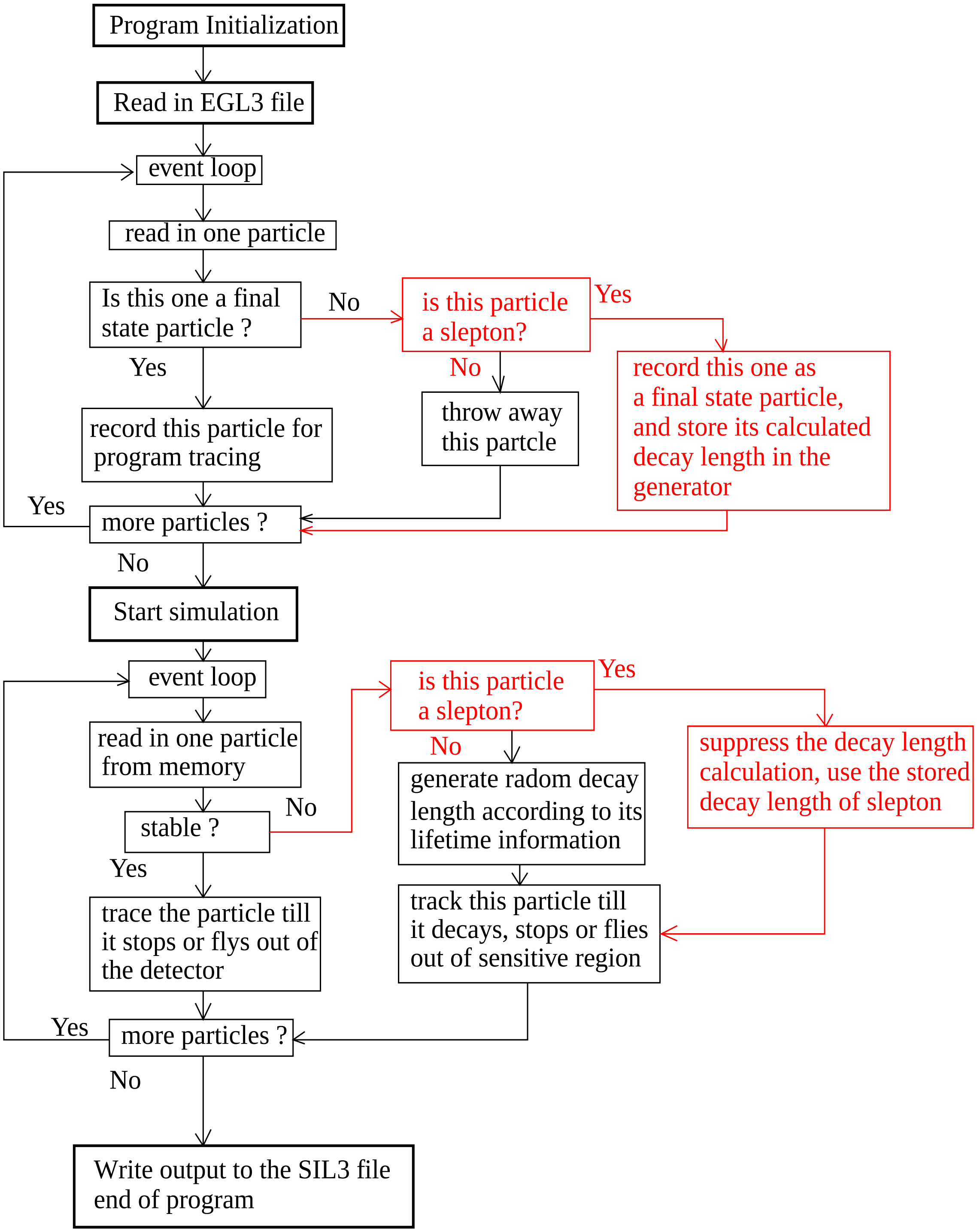

Figure 5.2: Flow diagram of the modified SIL3 package, to get the $\tilde{\tau}$ simulation correct.

case. In fact, any new particle can be embedded into SIL3 in this way, simply by substituting the scalar lepton with any new particle of interest.

5.3 L3 TEC dE/dx simulation

The L3 TEC is a rather small tracking chamber compared to other LEP experiments, due to the limited space available inside the high precision BGO electromagnetic calorimeter. It has a radius of 457 *mm* and 62 sense wires (8 in the inner TEC, 54 in the outer TEC) positioned along the radius. The innermost sense wire is placed at ~ 11 *cm* from the interaction point, and the outer most is at ~ 43 *cm*, so the total sensitive length in the radial direction is only ~ 32 *cm*.

- **ALEPH:** has an Inner Track Chamber(ITC) which covers the radius from 12.8 *cm* to 28.8 *cm* with 8 layers of sense wires, and an outer Time Projection Chamber (TPC) which covers the radius from 31 *cm* to 180 *cm* with 3-d readout. The dE/dx resolution is 4.5% for Bhabha electrons.
- **DELPHI:** has an Inner detector which consists of a JET chamber (24 sense wires in each sector) and 5 trigger layers, and covers the radius from 13 *cm* to 29 *cm*, and a Time Projection Chamber (TPC) which covers the radius from 29 *cm* to 122 *cm*.
- **OPAL:** has a Central Vertex Detector which is a drift chamber of 23.5 *cm* radius, and a jet chamber that covers the radial range from 25 *cm* to 185 *cm* by 24 identical sectors with a plane of 159 sense wires in each sector.

The L3 TEC still provides reasonably good vertex resolution(together with the SMD), tracking efficiency and momentum resolution at low momenta. Although it suffers from relatively low dE/dx resolution, the L3 TEC can still provide useful information about the ionization of charged tracks for particle identification. This is especially true for heavy charged stable particle searches, such as the $\tilde{\tau}$ searched for in this analysis with long lifetime. However, a practical version of the L3 TEC dE/dx simulation was not available until 1997, and that was mainly for particle identification in 2-photon physics events, i.e., for particles with rather low momentum.

The L3 TEC dE/dx simulation is not based on a full detector simulation, but on a fit to the single wire signal distribution, normalized by the Bethe-Bloch formula. The parameters of the Bethe-Bloch formula are calculated from the measured dE/dx values for different particles in various $\beta\gamma$ regions.

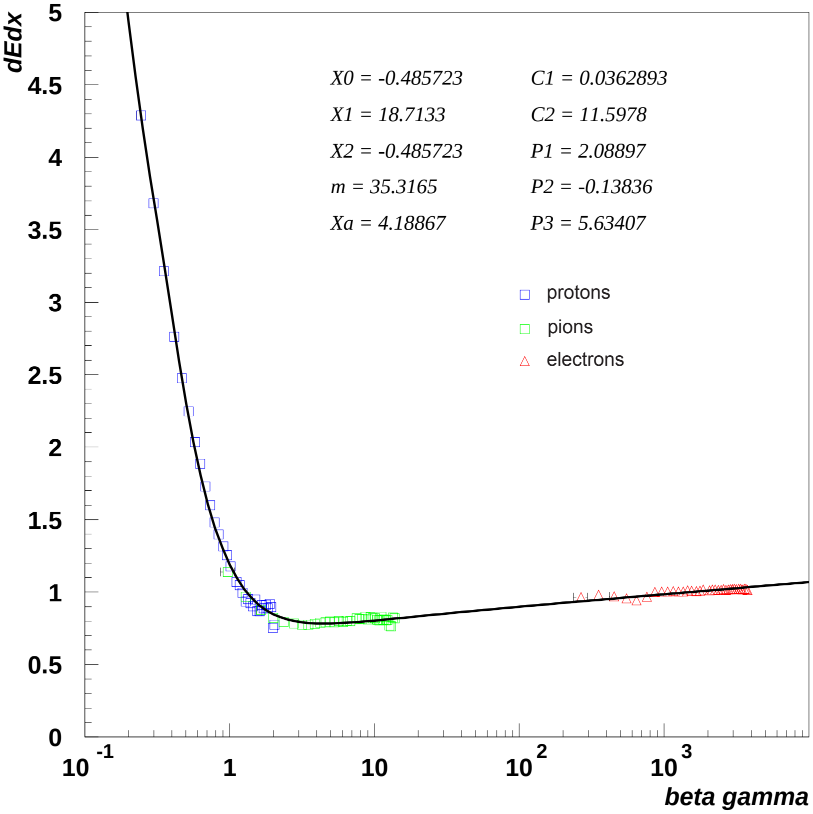

Figure 5.3: Fit of the Bethe-Bloch formula using proton, pion and electron samples in the old L3 TEC dE/dx simulation [64].

Figure 5.3 shows the fitted Bethe-Bloch formula together with the measured points from proton, pion and electron samples, in the old simulation.

The 1997 version of the simulation works reasonably well for particles with rather low momentum ($p \leq 10\,GeV$), which is sufficient for 2-photon physics. However, when it comes to an analysis searching for heavy charged stable particles, such as a $\tilde{\tau}$ with long lifetime, several problems appear:

1. In the simulation code, the $\beta\gamma$ value should be calculated from the particle's real momentum, which is the one produced by the generator. In the 1997 version of the L3 code, it was the TEC measured momentum that was used to calculate $\beta\gamma$ and dE/dx. This introduced an unwanted extra uncertainty from the momentum measurement, which is a very serious problem when the

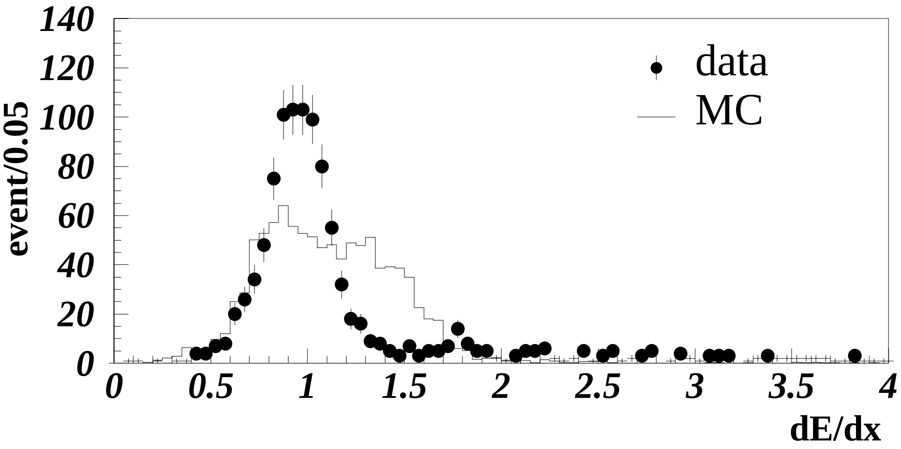

Figure 5.4: Data and MC simulation agreement: old calculation.

particle has a rather large momentum ($p = 20\ GeV$ or larger).

2. Using the 1997 version of the dE/dx simulation, one can observe a systematic deviation of dE/dx in the high $\beta\gamma$ range from the measured values. This is mainly due to a wrong fit of the Bethe-Bloch formula in Figure 5.3, in which the fit used a wrong dE/dx sample (electron sample) in the high $\beta\gamma$ region that doesn't follow the Bethe-Bloch formula at all. This wrong fit led to a wrong calculation of the dE/dx for particles that follow the Bethe-Bloch formula.
3. Obviously the dE/dx calculation for electrons from the fitted Bethe-Bloch formula was also wrong. The electron doesn't obey the Bethe-Bloch formula, and should have a separate calculation.
4. Although the 1997 simulation considered the hit pattern of TEC wires of a particular track, it didn't consider the performance of bad wires. Some wires had decreased performance after several years' running.
5. The single wire signal distribution used in the 1997 simulation does not agree with all types of TEC sense wires. A more careful fit of the distribution for each type is necessary.

As a result of these problems, the dE/dx distribution of Monte Carlo events has a large deviation from the measured data distribution. Figure 5.4 shows the agreement between the data and the Monte Carlo simulation of dE/dx for selected events with two back to back tracks and a visible energy between 1/10 and 1/2 of the center of mass energy. To solve these problems, it was necessary to rewrite the whole dE/dx simulation code. Section 5.3.1 discusses the whole procedure of the dE/dx simulation, and Section 5.3.2 presents how it was realized.

5.3.1 Method of dE/dx Simulation for the L3 TEC

The dE/dx simulation consists of two parts: the generation of the single wire signal distributions, and the calculation of particle ionization energy loss which acts as a scaling factor on the wire signal. Here I present the method of their calculation.

Calculation of the single wire signal distribution

The energy loss by ionization of a charged particle in a thin layer of matter has strong fluctuations. It was first theoretically described by Landau [65], and gave rise to an asymmetric probability density distribution with a narrow peak and a long tail towards the positive end, which is due to a small probability of losing a relatively large energy in a small number of collisions. The mathematical definition of the Landau distribution is

$$\phi(\lambda) = \frac{1}{2\pi i}\int_{c-i\infty}^{c+i\infty} e^{\lambda s + s ln s} ds \ , \tag{5.1}$$

where λ is a dimensionless number and is proportional to the energy loss, and c is any real positive number. The general CERN program library, CERNLIB [66], provided convenient functions to calculate the Landau possibility density distribution, as well as its integral, moment, and the inverse of integration which could be used to generate Landau distributed random numbers [67]. A closed analytic form of the probability density function is often used too for its simplicity [68]:

$$\Psi(\lambda) = (\frac{e^{-(\lambda+e^{-\lambda})}}{2\pi})^{\frac{1}{2}}, \quad \text{where } \lambda = \frac{(E-E_0)}{\Omega} \ . \tag{5.2}$$

Here E is the energy lost, E_0 is the most probable value, and Ω is a constant depending on the absorber. This distribution also has an asymmetric feature, however it has a much shorter tail compared to the Landau distribution. In reality, none of the above distributions can perfectly fit the single wire signal for all types of TEC sense wires. A combination of the two was used to fit the TEC wire signal distributions.

Calculation of particle ionization energy loss: the Bethe-Bloch formula

Moderately relativistic charged particles other than electrons lose energy in matter primarily by ionization. The mean rate of energy loss is given by the Bethe-Bloch equation [69]. In practice, we use measured data for different particles in various $\beta\gamma$ regions to fit the Bethe-Bloch formula, and use it to calculate the dE/dx of a certain particle at a particular momentum. This dE/dx value is proportional to the most probable value of the single wire signal distribution and it was used as a scaling factor to generate the wire signal distributions. A parametrized form of the Bethe-Bloch formula is given by [70],

$$\frac{dE}{dx} = \frac{c_1}{\beta^2}[c_2 + log\beta^2\gamma^2 - \beta^2 - \frac{\delta}{2}] \tag{5.3}$$

$$\text{with} \quad \frac{\delta}{2}(x) = \begin{cases} 0, & X < X_0; \\ X_b(X - X_a) + X_b(X_a - X_0)[\frac{X_1 - X}{X_1 - X_0}]^m, & X_0 < X < X_1; \\ X_b(X - X_a), & X_1 < X. \end{cases}$$

$$\text{where} \quad X = log_{10}\beta\gamma = log_{10}\frac{p}{M} \quad ,$$

in which, c_1, c_2, X_0, X_1, X_a and m are parameters that are obtained from actual measurement, and X_b has a fixed value of 4.606 [70]. In practice, to avoid complexity in fitting and a possible deviation from the Bethe-Bloch formula at low $\beta\gamma$ due to atomic binding effect, a simple polynomial form is chosen in the low $\beta\gamma$ region,

$$\frac{dE}{dx} = P_1 + P_2 \times X + P_3 \times X^2, \quad \text{for} \quad X < X_2 \leq X_0 \ , \tag{5.4}$$

which brings in four more parameters, P_1, P_2, P_3 and X_2. In total there are 10 parameters to be obtained from the data fit.

Since the Bethe-Bloch formula is not suitable for calculating the ionization loss of electrons and positrons, a simple analytic form has been chosen, to reflect the fact that the ionization energy loss of an electron or positron saturates quickly after its momentum exceeds a few GeV:

$$dE/dx = 1 - e^{-ap^b} \ , \tag{5.5}$$

where p is the momentum of the electron (positron), and a, b are fitting parameters. The fit of the measured dE/dx from data produces not only the central value of dE/dx as a function of $\beta\gamma$ for different particles, but also the width of dE/dx ($\sigma_{dE/dx}$), which reflects the dE/dx resolution of the TEC.

Calculation of dE/dx

Given the TEC single wire signal distribution and the parametrized formula to calculate the ionization energy loss for various particles, dE/dx is then calculated from the generated wire signals with proper scaling, by following the reconstruction procedure for real data.

The single wire signal distribution is usually obtained by fitting the signal from one kind of particle that is easily separated from others. This distribution, when used to generate wire signals for other particles, is scaled in both its width and peak position. The calculated ionization energy loss is the scaling factor for the peak, and the measured width of dE/dx for different particles is the scaling factor for the width of the wire signal. At this stage, we also take into account the hit pattern of TEC wires. We generate the hit pattern (fired and unfired wires) for every TEC track according to the statistics of the TEC tracks in data, and keep the wire signals from fired TEC wires only.

After generating the wire signals for a particular charged particle in a Monte Carlo event, we then follow the real data processing procedure to get the simulated dE/dx. The dE/dx value of a track is the truncated mean of all available wire signals. For the L3 TEC, we truncate the 20% highest signals, and take the mean value of the remaining 80% of the wire signals as the measured dE/dx.

5.3.2 New TEC dE/dx Simulation

To realize the simulation method described in Section 5.3.1, we performed the TEC single wire signal fit by using data from $e^+e^- \to \mu^+\mu^-$ or e^+e^- at the Z^0 peak. We fit the Bethe-Bloch formula using selected samples of K, π, p, and μ, and fit separately a formula for electrons.

TEC single wire signal distribution fit

Originally, there were four types of sense wires among the 62 sense wires along the radial direction in TEC: inner TEC normal wires (6 in total, type 1), inner TEC z-wires (2, type 2), outer TEC normal wires (45, type 3) and outer TEC z-wires (9, type 4). After many years of LEP running, bad wires appeared and became type 5. Figure 5.5 shows the signal distribution from a typical good wire, and Figure 5.6 shows a typical bad wire. The shapes of the distributions are quite different, and need a separate fit. Since the majority of wires were type 3, only bad wires in type 3 were considered. The fraction of bad wires was estimated to be 10 out of 45 (~22%).

The signal distribution for the five types of wires are fitted separately, using a combination of the Landau distribution (with long tail) and the simplified Landau form (without long tail), as discussed in Section 5.3.1:

$$\psi \;=\; \left(\frac{e^{-(y+e^{-y})}}{2\pi}\right)^{\frac{1}{2}} + c \times DENLAN(y), \quad \text{where} \quad y = \frac{(x-x_0)}{\Omega}\;, \tag{5.6}$$

in which DENLAN(y) is the Landau distribution function provided by CERNLIB, x is the wire signal, and x_0, Ω and c are fitting parameters. ‘c’ reflects the ‘tail’ in the distribution. We performed the single wire signal fit using the wire signal data from processes $e^+e^- \to \mu^+\mu^-$ or e^+e^- at Z^0 peak, provided by Saverio Braccini. The result of the fit is shown in Table 5.1. It seems that only the two types of

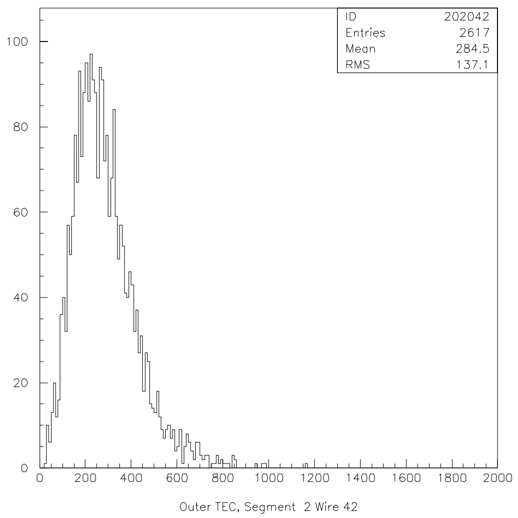

Figure 5.5: Single wire signal distribution for a typical good sense wire.

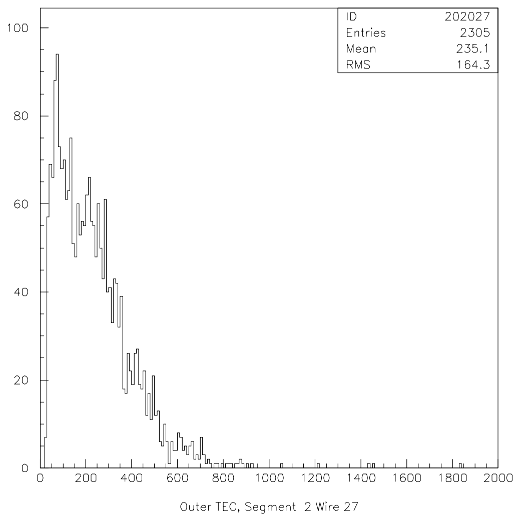

Figure 5.6: Single wire signal distribution for a typical bad sense wire.

inner TEC sense wires had a long tail component in their signal distribution. Figure 5.7 shows the fitted curve together with the wire signal data distribution for each type of wire.

Type of wires	Ω	x_0	c
1	42.1	107.3	0.253
2	55.3	302.5	1.857
3	70.5	220.5	0.
4	137.2	513.2	0.
5	69.9	158.6	0.

Table 5.1: Parameters for single wire signal distributions, fitted from data.

K, π, p, and μ sample selection

To fit the Bethe-Bloch formula, we need to select rather pure particle samples with a relatively precise knowledge of their momentum, in order to cover all of the useful $\beta\gamma$ (= p/m) region. In the high $\beta\gamma$ region, to have a sample with high momentum resolution, the only choice is a muon with its momentum measured by the L3 precision muon chamber system, while in the low $\beta\gamma$ region, we have quite some choices, including K, π, p, etc. The momentum measured by the L3 TEC has acceptable precision at low momentum. We selected all these particles to cover as much of a $\beta\gamma$ region as possible, and we also

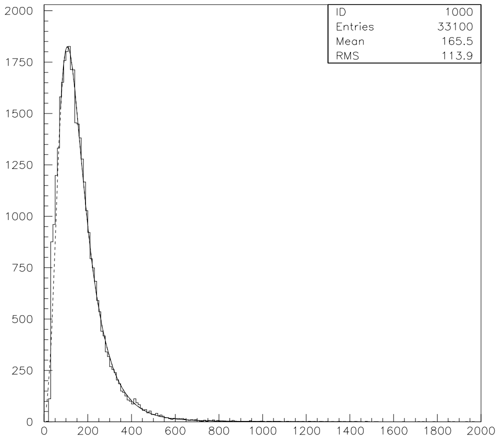

Type 1: Inner TEC normal sense wire

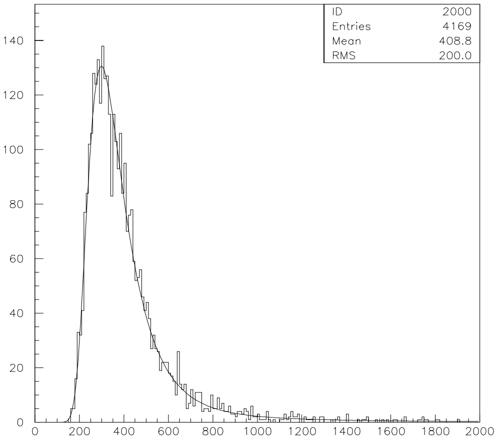

Type 2: Inner TEC Z wire

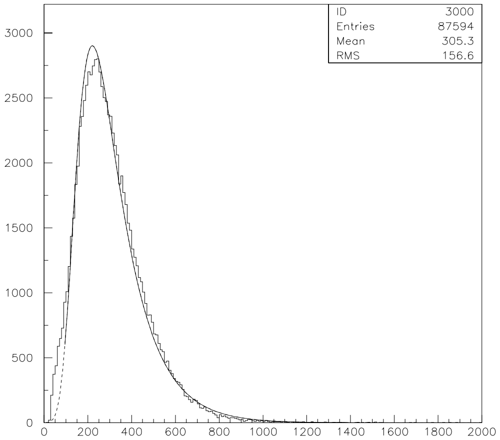

Type 3: Outer TEC normal sense wire

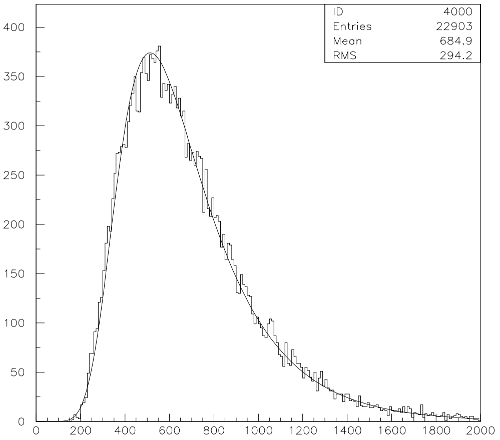

Type 4: Outer TEC Z wire

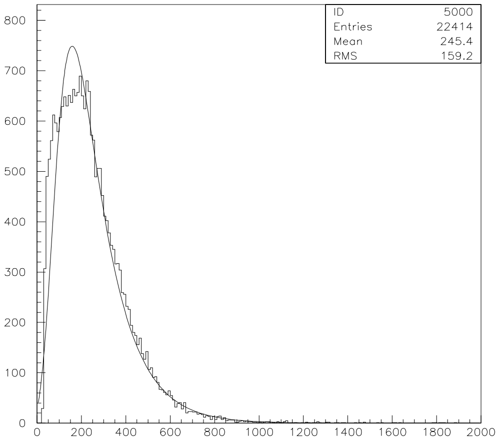

Type 5: Bad wire

Figure 5.7: Fits of TEC single wire signal distributions for 5 different wire types.

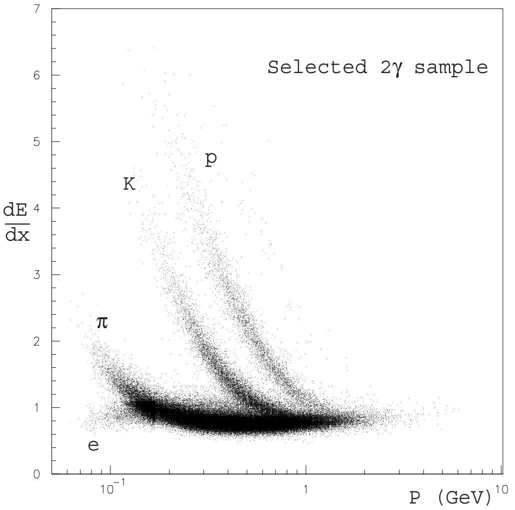

Figure 5.8: Selected sample of events for two-photon interactions, in which we have rich π, K and p subsamples, used to perform the dE/dx fit.

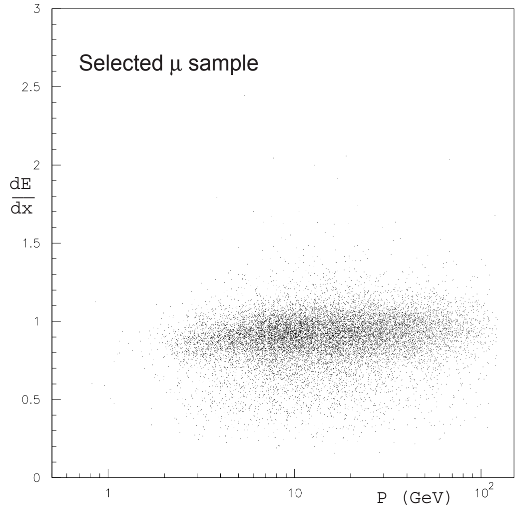

Figure 5.9: Selected μ sample for the dE/dx fit, which is the only sample that can cover the high $\beta\gamma$ region with a precise knowledge of the particle momentum.

checked the validity of this fit by using overlapping regions for different particles.

Two photon samples are rich in pions, kaons and protons. In particular, a pure pion sample can be easily selected from the process $e^+e^- \to e^+e^-\rho\rho$ [71], since ρ decays into two pions ($\rho \to \pi\pi$) almost 100% of the time. Including measured dE/dx information, we can also separate out kaon and proton samples easily. Muons can be easily identified by well measured tracks in the L3 muon chamber system. Here, we list the selection criteria for these particles:

- Two-photon sample: the selection criteria are listed below in Table 5.2. The key point is requiring low visible mass and missing momentum pointing along the beam pipe. The measured dE/dx as a function of the measured particle momentum is shown as a scatter plot in Figure 5.8, in which we can clearly identify the bands for π, k and p, as well as some electrons at low momentum. By applying some additional requirements, one can easily separate out each individual particle.
    - π **samples:** in addition to the requirements above for the 2-photon event sample, we require that each event has exactly 4 good tracks. Good tracks are defined as having at least 40 hits and a DCA smaller than 5 mm. The selected π sample is shown in Figure 5.10. Although residual K and p bands are quite visible in this scatter plot, we can see from Figure 5.11, which is a narrow slice taken from a narrow interval of particle momentum in Figure 5.10,

Variables	Selection criteria
$M_{visible}$	$<\ 10\ GeV$
$\theta(P_{missing})$	$< 0.09\ rad$ or $> 3.05\ rad$
$E_{visible}$	$<\ 50\ GeV$
N_{tracks}	$>\ 2\ and\ <\ 6$
DCA_{best}	$<\ 3\ mm$
$E_{ALR+Lumi}$	$<\ 10\ GeV$

Table 5.2: Selection criteria for 2-photon samples.

that the purity of this π sample is better than 95%.

- K **and** p **samples:** no additional cut was applied, except some direct cut on the dE/dx–P plot to extract the obvious bands of K and p.

- Muon sample: muons can be easily identified at L3, using the precise muon chambers. We required a good muon track with momentum of at least 3 GeV, and DCA of the muon track less than 100 mm in both the $R-\phi$ plane and along the beam direction. In addition, a good TEC track must match the muon track measured by the muon chambers. Figure 5.9 shows the selected muon sample in the dE/dx–P plane.

Fitting the Bethe-Bloch Formula

Once the particle samples are separated out, fitting the Bethe-Bloch formula is straightforward. By taking a small bin of particle momentum, we can fit the dE/dx distribution of this sub-sample of identified particles by a Gaussian. The mean and width of dE/dx from the Gaussian fit are then assigned to the mean value of the momentum ($\bar{P}$) of this bin. By creating a large number of bins for each particle sample we have, we can then create a sufficient number of sample points (dE/dx, $\bar{P}$) throughout the $\beta\gamma$ region in which we are interested. We then fit these sample points with the parametrization of the Bethe-Bloch formula described by Equation 5.3.

The result of the dE/dx fit is shown in Tables 5.4, 5.5, 5.6 and 5.7, for π, K, p and μ, respectively. The width and average of the momentum bin are also shown, together with the fitted dE/dx mean value, the corresponding width, and their uncertainties.

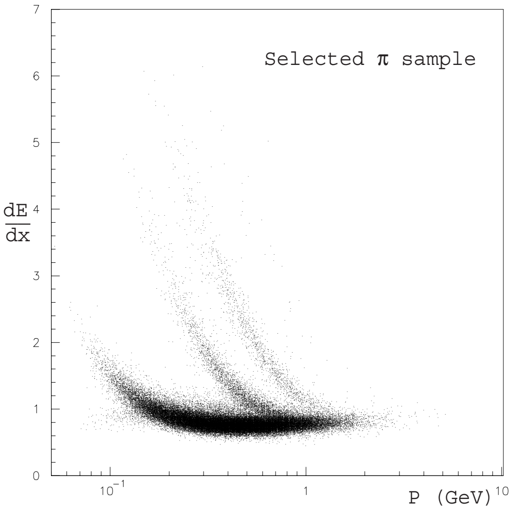

Figure 5.10: π sample selected from 2-photon events.

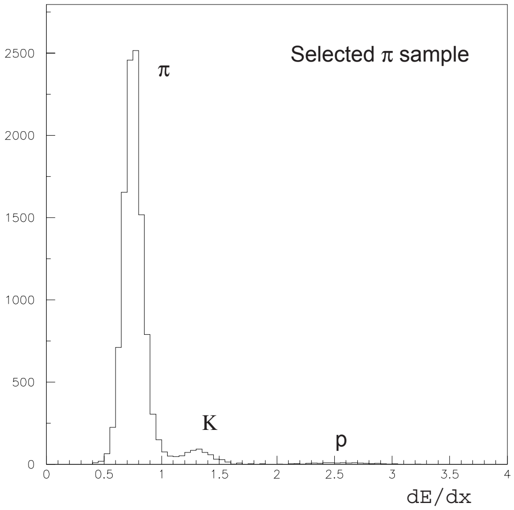

Figure 5.11: Purity of selected π sample, in which we can identify the remaining K and p content.

$\bar{P}$ (GeV)	ΔP (GeV)	dE/dx	$\Delta(dE/dx)$	$\sigma_{dE/dx}$	$\Delta(\sigma_{dE/dx})$
0.05	0.02	2.90	0.43	0.74	0.94
0.063	0.006	2.35	0.15	0.40	0.32
0.073	0.006	2.087	0.034	0.267	0.032
0.080	0.004	1.868	0.055	0.269	0.083
0.086	0.004	1.726	0.023	0.192	0.029
0.094	0.004	1.574	0.016	0.181	0.016
0.102	0.004	1.447	0.013	0.161	0.014
0.116	0.004	1.3027	0.0081	0.1405	0.0083
0.130	0.004	1.1695	0.0093	0.1398	0.0093
0.144	0.004	1.0692	0.0058	0.1265	0.0057
0.158	0.004	1.0069	0.0048	0.1100	0.0047
0.178	0.004	0.9552	0.0047	0.1006	0.0044
0.198	0.004	0.8925	0.0037	0.0918	0.0034
0.218	0.004	0.8646	0.0036	0.0977	0.0032
0.248	0.004	0.8213	0.0033	0.0892	0.0030

0.278	0.004	0.7988	0.0032	0.0839	0.0031
0.308	0.004	0.7718	0.0030	0.0812	0.0026
0.338	0.004	0.7649	0.0029	0.0802	0.0026
0.368	0.004	0.7532	0.0029	0.0726	0.0027
0.398	0.004	0.7528	0.0033	0.0802	0.0029
0.438	0.004	0.7491	0.0030	0.0756	0.0026
0.478	0.004	0.7448	0.0037	0.0809	0.0032
0.518	0.006	0.7475	0.0028	0.0734	0.0023
0.558	0.006	0.7463	0.0032	0.0761	0.0033
0.598	0.006	0.7516	0.0031	0.0740	0.0030
0.638	0.006	0.7492	0.0035	0.0718	0.0029
0.678	0.006	0.7573	0.0032	0.0744	0.0026
0.72	0.008	0.7602	0.0034	0.0716	0.0026
0.77	0.008	0.7588	0.0046	0.0787	0.0048
0.82	0.01	0.7711	0.0045	0.0811	0.0040
0.87	0.01	0.7700	0.0045	0.0808	0.0042
0.92	0.01	0.7753	0.0039	0.0672	0.0034
0.98	0.02	0.7797	0.0033	0.0700	0.0032
1.04	0.02	0.7822	0.0033	0.0653	0.0027
1.11	0.04	0.7795	0.0031	0.0727	0.0025
1.18	0.04	0.7900	0.0039	0.0866	0.0038
1.30	0.06	0.7989	0.0037	0.0757	0.0036
1.40	0.06	0.7958	0.0045	0.0769	0.0041
1.55	0.08	0.8051	0.0056	0.0832	0.0056
1.75	0.1	0.8224	0.0076	0.0861	0.0080
2.0	0.2	0.8100	0.0074	0.0857	0.0078
2.4	0.2	0.832	0.054	0.176	0.086
2.8	0.4	0.841	0.048	0.163	0.076
3.5	1.0	0.843	0.091	0.22	0.19

Table 5.4: Results from the π sample fit: dE/dx and its width with their uncertainties in the Gaussian fit. The width of the momentum bin, and the average momentum of each bin are also shown.

$\bar{P}$ (GeV)	ΔP (GeV)	dE/dx	$\Delta(dE/dx)$	$\sigma_{dE/dx}$	$\Delta(\sigma_{dE/dx})$
0.11	0.02	4.52	0.62	1.1	1.2
0.13	0.02	4.33	0.13	0.59	0.20
0.15	0.02	3.80	0.11	0.54	0.16
0.17	0.02	3.389	0.046	0.346	0.075
0.195	0.01	2.874	0.059	0.384	0.056
0.215	0.01	2.711	0.034	0.287	0.045
0.235	0.01	2.497	0.023	0.227	0.021
0.265	0.01	2.191	0.016	0.194	0.013
0.295	0.01	1.912	0.014	0.183	0.012
0.325	0.01	1.743	0.012	0.168	0.013
0.355	0.01	1.5932	0.0100	0.1717	0.0097
0.38	0.02	1.4775	0.0083	0.1441	0.0093
0.42	0.02	1.3164	0.0076	0.1476	0.0082
0.45	0.02	1.2322	0.0081	0.1225	0.0089
0.48	0.02	1.142	0.015	0.144	0.012

Table 5.5: Results from the K sample fit: dE/dx and its width with their uncertainties in the Gaussian fit. The width of the momentum bin, and the average momentum of each bin are also shown.

Using the obtained (dE/dx, $\bar{P}$) value from all the particle samples, we fit the Bethe-Bloch formula and obtained the following value for the parameters:

X0=0.19334 XA=6.6113
X1=1.9146 X2=0.19334
C1=0.016751 P1=1.13433373
C2=36.110 P2=-2.40285325
M=1.5765 P3=5.0205

The fitted Bethe-Bloch curve with all the sample points is shown in Figure 5.12, together with the old Bethe-Bloch fit in previous dE/dx simulation for comparison. The new curve fits the data points better, especially in the minimum ionization region and in the large $\beta\gamma$ region.

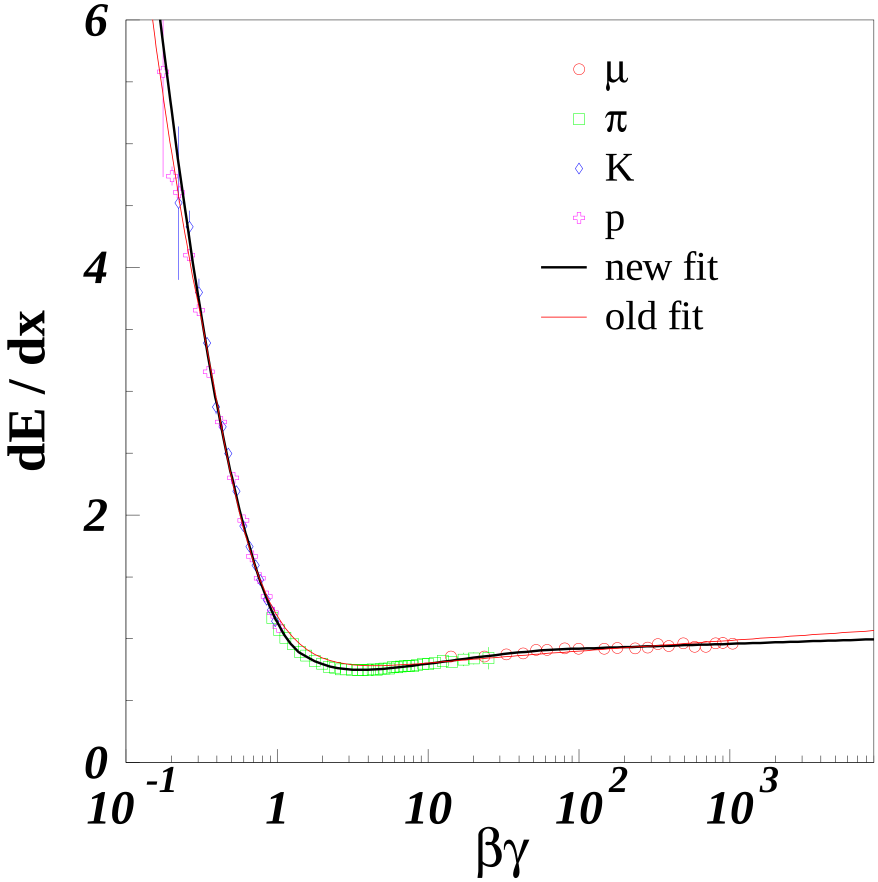

Figure 5.12: The fitted Bethe-Bloch formula with all the data sample points, compared with the Bethe-Bloch curves fitted using the old version of the simulation.

$\bar{P}$ (GeV)	ΔP (GeV)	dE/dx	$\Delta(dE/dx)$	$\sigma_{dE/dx}$	$\Delta(\sigma_{dE/dx})$
0.165	0.03	5.58	0.85	1.6	1.9
0.19	0.02	4.738	0.077	0.39	0.16
0.21	0.02	4.605	0.080	0.503	0.090
0.245	0.03	4.101	0.037	0.379	0.039
0.285	0.03	3.653	0.044	0.484	0.058
0.33	0.04	3.157	0.026	0.310	0.023
0.40	0.04	2.751	0.014	0.229	0.013
0.48	0.04	2.299	0.011	0.202	0.010
0.56	0.04	1.956	0.011	0.184	0.011
0.64	0.04	1.667	0.010	0.1521	0.0098
0.72	0.04	1.4902	0.0092	0.138	0.011
0.80	0.06	1.342	0.019	0.133	0.018
0.88	0.06	1.211	0.022	0.129	0.019
0.96	0.06	1.097	0.026	0.117	0.019

Table 5.6: Results from the p sample fit: dE/dx and its width with their uncertainties in the Gaussian fit. The width of the momentum bin, and the average momentum of each bin are also shown.

Fitting of Electrons

Using a procedure similar to that used in fitting the Bethe-Bloch formula, we first obtained a sample of electrons (positrons) and then fit them to the parametrized formula described by Equation 5.3.

Since the dE/dx measurements in the L3 TEC are normalized to the values for $e^{\pm}$ at the Z^0 peak, it is not necessary to get an electron sample with momentum higher than a few GeV — its dE/dx is stable above a few GeV and is always 1, by definition. However, electron samples at low momentum are also easy to obtain from two-photon event samples. By applying a dE/dx cut, one can take out the electron band in Figure 5.8. Following the same procedure for π, K, p and μ, we get the sample points (dE/dx, $\bar{P}$) for electrons too, which are listed in Table 5.8. Fitting Equation 5.3 is an easy task, and we get:

$$a = 14.5 \pm 2.2 \qquad b = 0.859 \pm 0.060$$

The fitted electron curve is shown in Figure 5.13, together with the data sample points. The old

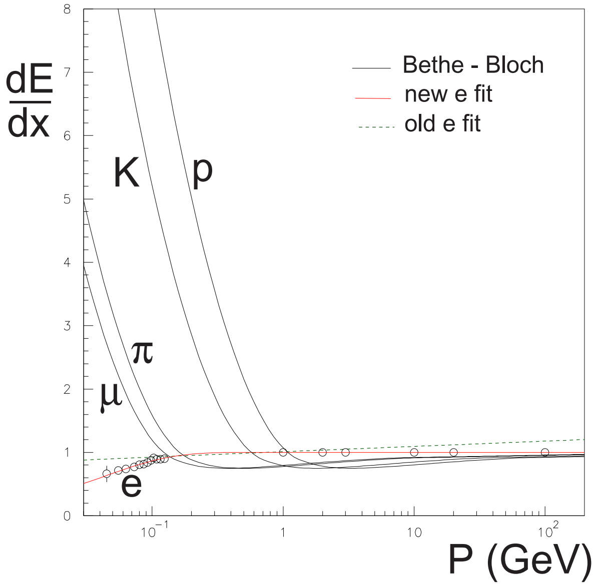

Figure 5.13: Electron fit: new fit curve with electron sample points, compared with the old fit. The new Bethe-Bloch curves are also shown.

dE/dx curve for electrons from the earlier version of the dE/dx simulation is shown as a dashed line for comparison. The difference is huge, and this is one of the main reasons for the failure of the old simulation. In this plot, the dE/dx values for π, K, p and μ calculated from the Bethe-Bloch formula are also shown.

Adjustment of Width

A byproduct of the above fit is the width σ of the measured dE/dx distribution for each particle, which reflects the resolution of the dE/dx measurement, $\Delta_{dE/dx} = \sigma_{dE/dx}/(\text{dE/dx})$. Taking the proper average for each particle sample, we get the following results for the dE/dx resolution $\Delta_{dE/dx}$ (we assume that the widths for e and μ are equal):

$$\begin{aligned}
\Delta_{dE/dx}(e,\mu) &= 0.1005 && \pm\, 0.0046 \\
\Delta_{dE/dx}(\pi) &= 0.1011 && \pm\, 0.0034 \\
\Delta_{dE/dx}(K) &= 0.101 && \pm\, 0.021 \\
\Delta_{dE/dx}(p) &= 0.0916 && \pm\, 0.0068\ ,
\end{aligned}$$

from which we get the dE/dx resolution of the L3 TEC is approximately 10.0%. Within the measurement uncertainty, it is independent of particle identity. This result is quite different from the old fit, where we had different dE/dx resolution for different particles.

In principle, this width measurement should have no impact on our dE/dx simulation, since the width there is taken into account from the single wire signal fit already. However, since the wire signal fit was carried out on the electron and muon samples at the Z^0 peak, taken in 1995, we do expect some changes from that time. We then simulated the pion sample to compare with the data measurement. Table 5.9 shows the comparison between data and Monte Carlo samples, in which we take exactly the same momentum binning, and compare the fitted dE/dx and its width. We observe:

- The fitted dE/dx values agree extremely well, which validates our Bethe-Bloch fit.
- The fitted width of dE/dx has a significant difference. It is likely to be the hardware changes from 1995 to 1999. We measured $\Delta_{dE/dx}$ from both data and Monte Carlo samples:

$$\begin{aligned} \Delta_{dE/dx}(data) &= 0.0997 \pm 0.0046 \\ \Delta_{dE/dx}(MC) &= 0.0687 \pm 0.0035 \end{aligned}$$

So the width measured from data is 1.451±0.099 times larger than the Monte Carlo simulation. We then included this 1.451 factor in our simulation to adjust the width of dE/dx.

5.3.3 Result of the New dE/dx Simulation

After our complete rewrite of the simulation program, we can look back at the distribution of dE/dx for back to back charged tracks. Figure 5.14 shows the data - Monte Carlo agreement using the new simulation. Compared to Figure 5.4, it is a considerable improvement. However, there are still non-negligible deviations between the measured values and that from the Monte Carlo simulation. The reasons are the following:

- Due to the limited data sample, the fit of the single wire signal was carried out using data from only one out of the 24 TEC sectors. The estimated number of bad wires and their signal behavior were also based on the knowledge of this TEC sector. The optimal method would be, if we had enough statistics, to fit each TEC wire individually and store the wire response in a database.
- The only available data for the TEC single wire signal was from 1995, and this dE/dx simulation is mainly for the Monte Carlo simulation of the 1999 and 2000 events. The TEC response changed in the mean time, as we have already seen from the dE/dx resolution.

- For this simulation, we studied good tracks only. But this is not a problem for our slepton analysis, since we use only good tracks there.
- A recent report [72] showed a dE/dx dependence on the θ coordinate of a track. This effect was not considered in our simulation.

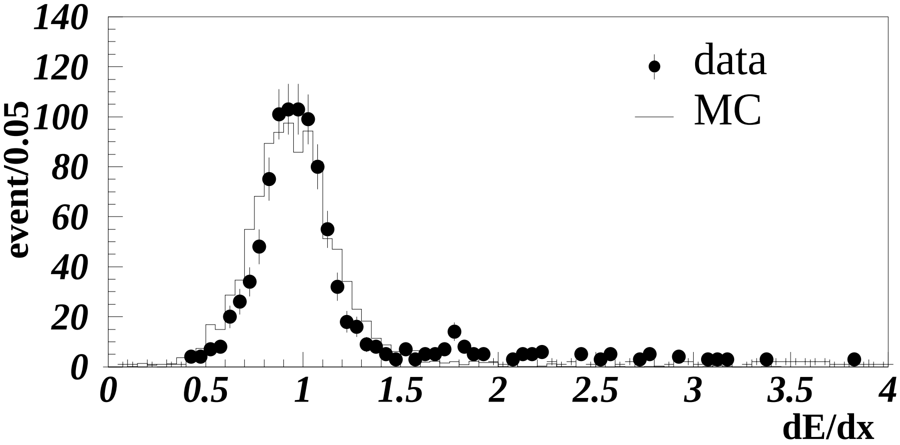

Figure 5.14: Data and MC simulation agreement: results of the new simulation.

$\bar{P}$ (GeV)	ΔP (GeV)	dE/dx	$\Delta(dE/dx)$	$\sigma_{dE/dx}$	$\Delta(\sigma_{dE/dx})$
1.5	1.	0.856	0.038	0.115	0.067
2.5	1.	0.8570	0.0049	0.0776	0.0047
3.5	1.	0.8739	0.0046	0.0875	0.0041
4.5	1.	0.8798	0.0042	0.0878	0.0041
5.5	1.	0.9091	0.0041	0.0848	0.0041
6.5	1.	0.9115	0.0050	0.0974	0.0055
8.5	1.	0.9229	0.0044	0.0871	0.0039
10.5	1.	0.9203	0.0054	0.092	0.005
15.5	1.	0.9193	0.0078	0.103	0.009
19.	2.	0.9246	0.0071	0.098	0.008
25.	2.	0.9245	0.0072	0.105	0.008
30.	2.	0.9276	0.0071	0.095	0.007
35.	2.	0.9552	0.0080	0.104	0.007
41.5	3.	0.942	0.011	0.121	0.011
52.	4.	0.962	0.010	0.103	0.017
62.	4.	0.936	0.021	0.142	0.032
73.	6.	0.935	0.040	0.189	0.055
85.	10.	0.962	0.039	0.183	0.059
95.	10.	0.965	0.047	0.179	0.074

Table 5.7: Results from the μ sample fit: dE/dx and its width with their uncertainties in the Gaussian fit. The width of the momentum bin, and the average momentum of each bin are also shown.

$\bar{P}$ (GeV)	ΔP (GeV)	dE/dx	$\Delta(dE/dx)$	$\sigma_{dE/dx}$	$\Delta(\sigma_{dE/dx})$
0.045	0.01	0.66	0.13	0.32	0.21
0.055	0.01	0.717	0.011	0.118	0.010
0.063	0.004	0.737	0.010	0.097	0.010
0.073	0.004	0.7688	0.0087	0.1060	0.0092
0.080	0.004	0.8074	0.0080	0.0930	0.0076
0.086	0.004	0.816	0.013	0.119	0.016
0.092	0.004	0.844	0.011	0.111	0.014
0.098	0.004	0.8719	0.0099	0.1061	0.0087
0.103	0.004	0.914	0.018	0.136	0.015
0.108	0.004	0.890	0.013	0.103	0.013
0.116	0.004	0.893	0.011	0.093	0.008
0.124	0.004	0.902	0.027	0.089	0.019

Table 5.8: Results from the e sample fit: dE/dx and its width with their uncertainties in the Gaussian fit. The width of the momentum bin, and the average momentum of each bin are also shown.

$\bar{P}$ (GeV)	ΔP (GeV)	dE/dx	$\Delta(dE/dx)$	$\sigma_{dE/dx}$	$\Delta(\sigma_{dE/dx})$
0.16	0.01	1.0015	0.0034	0.1018	0.0030
0.21	0.01	0.8777	0.0027	0.0919	0.0022
0.31	0.01	0.7761	0.0020	0.0796	0.0018
0.41	0.02	0.7559	0.0017	0.0783	0.0014
0.51	0.02	0.7523	0.0018	0.0726	0.0015
0.61	0.02	0.7452	0.0021	0.0687	0.0019
0.71	0.02	0.7649	0.0029	0.0748	0.0025
0.81	0.02	0.7750	0.0032	0.0738	0.0031
0.91	0.02	0.7673	0.0041	0.0694	0.0041

$\bar{P}$ (GeV)	ΔP (GeV)	dE/dx	$\Delta(dE/dx)$	$\sigma_{dE/dx}$	$\Delta(\sigma_{dE/dx})$
0.16	0.01	1.0113	0.0028	0.0688	0.0024
0.21	0.01	0.8726	0.0028	0.0602	0.0026
0.31	0.01	0.7729	0.0031	0.0527	0.0031
0.41	0.02	0.7502	0.0024	0.0500	0.0020
0.51	0.02	0.7540	0.0029	0.0514	0.0028
0.61	0.02	0.7543	0.0032	0.0528	0.0030
0.71	0.02	0.7620	0.0032	0.0542	0.0033
0.81	0.02	0.7610	0.0038	0.0543	0.0049
0.91	0.02	0.7683	0.0047	0.0579	0.0051

Table 5.9: Comparison between the measured dE/dx (top) and the simulated dE/dx (bottom) for π samples with exactly the same momentum binning. There was very good agreement in the dE/dx central value. The width, however, was different by a fixed factor within the uncertainty. The difference was due to the single wire signal fit in which we used old data sample from 1995. The width of the simulated dE/dx was corrected using this factor in the final simulation.

6. Search for Scalar Leptons in SUGRA

Assuming the $\tilde{\chi}_1^0$ is the lightest supersymmetric particle (LSP) and R parity is conserved, we expect scalar leptons ($\tilde{l}$, $l = e, \mu, \tau$) to have very short lifetimes in SUGRA [73]. The resulting signature in pair production would be two acoplanar leptons and large missing energy through the process:

$$e^+e^- \to \tilde{l}^+\tilde{l}^-, \quad \text{and each slepton} \quad \tilde{l} \to l\tilde{\chi}_1^0. \tag{6.1}$$

This chapter focuses on the analysis using events with this kind of signature. Section 6.1 discusses the event reconstruction and lepton/photon identification, as well as the new particle group ntuple as a general tool. Section 6.2 shows the selection issues, optimization of the selection, and the way to handle different signatures by a parametrized selection. Section 6.3 summarizes the results obtained in this analysis.

6.1 Event reconstruction and new particle group ntuple

The analysis in this thesis is carried out in the framework of new particle group ntuple [1]. This is a friendly environment that allows users to carry out their analysis efficiently from an established software package which takes care of the event reconstruction and the calculation of basic physics quantities in a controllable way. The reconstruction here means, given the reconstructed energy bumps and tracks in each sub-detector, to build meaningful objects and identify them as photons, leptons, or hadronic jets. This section discusses the reconstruction procedure and gives an overview of the structure of the new particle group ntuple.

6.1.1 Event reconstruction and particle identification

The event reconstruction starts from lepton/photon identification. This process starts with muons, which can be easily separated out using the measured tracks in the L3 muon chambers. After removing

---

[1] An ntuple is the basic type of data used in PAW, a physics analysis software package developed at CERN. It consists of a list of identical data structure, one for each event.

all the objects belonging to identified muons, the next most easily identified particles are electrons and photons. They are defined as electromagnetic bumps with and without associated TEC tracks. Electromagnetic bumps are identified by the shower shape measurement in the BGO. The next step is to identify taus, which are defined as a narrow jet with 1 to 3 associated tracks. The tau identification can recover some isolated muons missing a muon chamber track that leave the energy deposit profile of a MIP[2]. The remaining clusters and tracks are classified as hadrons. Jets are reconstructed with the Durham algorithm [74] forcing the reconstruction into two jets.

Lepton identification is important for this analysis, and thus is discussed in more detail. The new particle group ntuple provided a loose identification of leptons using very loose cuts, so that we can keep most of the possible lepton candidates and select the part that we want for any specific analysis by tightening one or more cuts. The tightened cuts are listed below, and are compared with the loose cuts used in the new particle ntuple.

Muon identification

Muons in the L3 detector are recognized by tracks in the muon chamber system. Only muons with a momemtum of 1.5 GeV or higher can pass through the inner detectors and reach the muon chambers. In this analysis, we require the momentum of a muon track to be greater than 3 GeV, and we associate to these muons the matched energy clusters in the ECAL and HCAL as well as the matched TEC tracks. In addition, we require an identified muon to have both the distance of closest approach in the $r-\phi$ plane (DCA) and the Z coordinate along the beam line (Z_0) of the measured muon chamber track to be less than 200 mm.

In Table 6.1, we listed the cuts for muon identification in this analysis, and the cut values in the new particle ntuple as well.

Cut Variable	Cut Value (this analysis)	Cut Value (NP ntuple)
P_μ	$> 3\ GeV$	$> 2\ GeV$
DCA	$< 200\ mm$	$< 500\ mm$
$\|Z_0\|$	$< 200\ mm$	$< 1000\ mm$

Table 6.1: Selection criteria for muon identification in this analysis, compared with the loose identification in the new particle group ntuple.

---

[2] Minimum ionizing particle.

Electron/Photon identification

Electrons and photons are defined as electromagnetic bumps with and without associated TEC tracks. Based on the fact that an electron (photon) produces a narrow electromagnetic shower in the ECAL with a large portion of the energy deposited in the single "hottest" crystal, the electromagnetic bumps are identified by requiring $\Sigma_9^c/\Sigma_{25}^c > 0.93$, $E_{HCAL}/E_{ECAL} < 0.1$ and $\chi^2_{EM} < 10$. Among the variables, Σ_9^c (Σ_{25}^c) is the energy deposited in a 3×3 (5×5) BGO crystal matrix in the ECAL around the most energetic crystal of the bump. E_{HCAL} (E_{ECAL}) is the partial energy of the bump deposited in the HCAL (ECAL). χ^2_{EM} is computed by fitting the lateral shower profile to what is expected from electrons according to test beam results. In addition, we require the energy of the electron/photon to be greater than 1 GeV.

In Table 6.2, we listed the cuts for electron/photon identification in this analysis, and the cut values in the new particle ntuple as well.

Cut Variable	Cut Value (this analysis)	Cut Value (NP ntuple)
Σ_9^c/Σ_{25}^c	> 0.93	> 0.93
E_{HCAL}/E_{ECAL}	< 0.1	< 0.2
χ^2_{EM}	< 10	—
E_e	$> 1\ GeV$	$> 1\ GeV$

Table 6.2: Selection criteria for electron/photon identification in this analysis, compared with the loose identification in the new particle group ntuple.

Tau identification

Based on the fact that most of the taus decay with either a one-prong decay mode (about 85%, one charged particle and other neutral ones in the final state), or a three-prong decay mode (about 15%, three charged particles and other neutral ones in the final state), the taus detected in the L3 detector are defined as narrow jets with low multiplicity (1 to 3 associated tracks and a small number of calorimeter clusters). We require the energy of the tau (defined as the energy of the clusters and tracks in a 10^o half opening angle cone) to be greater than 2 GeV, the number of clusters less than 8, and the ratio between the energy deposited in a 30^o cone excluding that from the tau and the tau energy to be less than 1.5.

The tau identification can recover some isolated muons missing a muon chamber track that leave the energy deposit profile of a MIP. In Table 6.3, we list the cuts for tau identification in this analysis, and the cut values in the new particle ntuple as well.

Cut Variable	Cut Value (this analysis)	Cut Value (NP ntuple)
N_{track}	$> 1, < 3$	$> 1, < 3$
$N_{cluster}$	< 8	< 8
E_{τ}	$> 2\ GeV$	$> 2\ GeV$
E_{10-30}/E_{10}	< 0.5	< 1.0

Table 6.3: Selection criteria for tau identification in this analysis, compared with the loose identification in the new particle group ntuple.

6.1.2 New particle group ntuple

The new particle ntuple set is routinely produced for each data sample of L3. The ntuple production runs through all the reconstruction procedure with a loose particle identification as described above, so that the users have the choice of selecting a tight particle identification whenever necessary.

In addition to the particle identification described above, this ntuple set also provides several other useful features:

- calculation of some important variables, such as visible energy, visible mass, etc. The visible energy takes into account the energy deposition in the calorimeters and the momentum measured by TEC and muon chambers. The algorithm [75] takes into account the difference between neutral and charged clusters (those associated with tracks) and has different calibration constants for each sub-detector;
- complete trigger information for data, and simulated trigger bits for Monte Carlo events;
- some useful generator level information for Monte Carlo events, such as the particle id's and their masses for the primary particles;
- B-tagging information;
- a varied set of jet reconstruction results, including forced into two jets without subtracting any leptons and photon; forced into two jets while subtracting only one identified lepton or photon (the subtraction running through all the identified leptons and photons), forced into two jets while

subtracting two identified lepton(s)/photon(s) (also running through all possible combinations among the identified leptons and photons), forced into four jets, forced into six jets, etc.;

- a dedicated block for single and multi-photon physics, which appeared in some versions.

In principle, the new particle group ntuple provides enough information for most physics analysis and significantly reduced the overall work load of carrying out an analysis. However, in some rare cases, as the analysis we will discuss in Chapter 7, additional information is needed to be included in a newly developed version.

6.2 Parametrized selection and optimization

For scalar leptons with prompt decay, the signature is simple since most of the time the final state is given by two acoplanar leptons of the same generation and large missing energy, as shown in Equation 6.1. To account for the three lepton types, three different selections are performed. While for scalar electrons and muons, two identified leptons are required in the event, scalar taus are selected as low multiplicity events with two leptons or narrow jets.

However, the total visible energy and the event configuration in the slepton production and decay process, $e^+e^- \to \tilde{l}^+\tilde{l}^-$ and $\tilde{l} \to l\tilde{\chi}_1^0$, largely depend on ΔM, the mass difference between the scalar lepton and the lightest neutralino ($M_{\tilde{l}} - M_{\tilde{\chi}_1^0}$), which is the available energy for scalar lepton decay. Figure 6.1 shows the distribution of the total visible energy of the scalar electron signal as a function of ΔM, compared with the same distribution from the data and the simulated Standard Model background processes. In the low ΔM region, most of the energy is taken away by the two undetectable neutralinos, and the event is left with two rather soft acoplanar leptons. The dominant background in this region is two-photon processes. On the other hand, in the high ΔM region, the total visible energy is quite high and the two acoplanar leptons are energetic, which is quite similar to the signature for leptonic W pair decay.

To account for the ΔM dependence, a parametrized selection has been developed, i.e., the cut values on the relevant physics variables are functions of ΔM and $M_{\tilde{l}}$. The parametrized cuts of each selection are a priori optimized using the Monte Carlo signal and background events. In this section, we will first discuss a loose pre-selection and Monte Carlo quality check, and then we focus on the optimization of the parametrized selection.

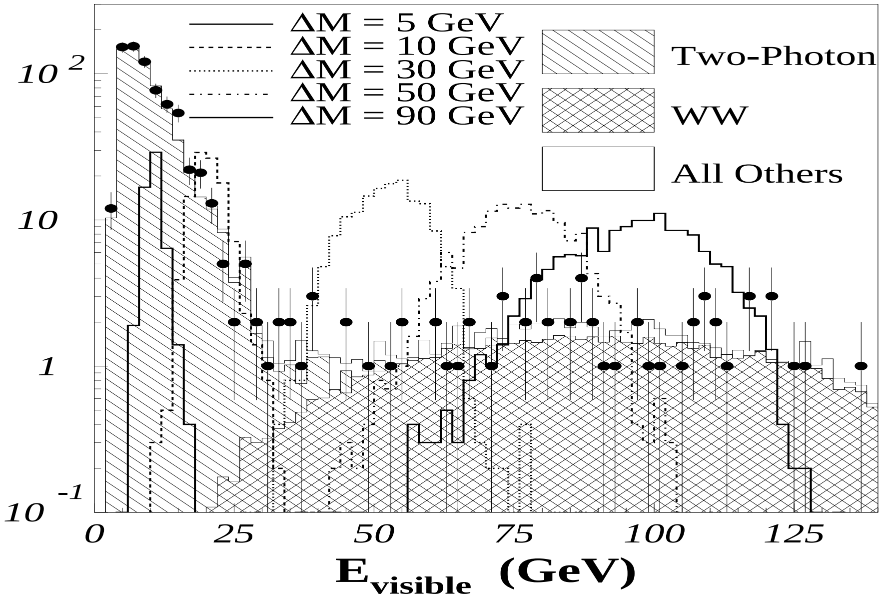

Figure 6.1: Distribution of the total visible energy of a scalar electron signal ($M_{\tilde{e}} = 80\ GeV$), as a function of ΔM, compared with the same distribution from the data and the simulated Standard Model background processes.

6.2.1 Event pre-selection

A loose pre-selection was applied for each scalar lepton flavor, with slightly different cut values. The pre-selection removed beam gas events, detector noise, tagged two-photon events, high multiplicity hadronic events, and selected a compact sample with large missing energy and unbalanced momentum. Since the pre-selection removed effects that are not simulated by Monte Carlo processes, such as the cosmic rays, beam gas events and low visible mass two-photon processes, etc., this was also an appropriate point to check the quality of the Monte Carlo simulation. The pre-selection cut variables and their values are listed bellow in Table 6.4.

The variables in the table are defined as follows:

- $E_{visible}$, the total visible energy of an event, taking into account the energies of all the calorimeter clusters, the momentum of the reconstructed TEC tracks, and the momentum of muon tracks, by a weighted sum of these quantities. The weights, called "g-factors," are optimized by minimizing the resolution of the visible energy. In this way, we avoided double counting of particle energy and used as much useful information as possible;

Cut Variable	$\tilde{e}$	$\tilde{\mu}$	$\tilde{\tau}$
$E_{visible}$	$< 95\%\sqrt{s}$		
$M_{visible}$	$> 3\ GeV, < 90\%\sqrt{s}$	$> 3\ GeV, < 90\%\sqrt{s}$	$> 3\ GeV, < 60\%\sqrt{s}$
P_t	$> 3\ GeV$		
$P_t/E_{visible}$	—	> 0.4	—
$P_{missing}$	—	$> 4\ GeV$	
N_{track}	$\geq 1,\ \leq 3$		$\geq 2,\ \leq 9$
$N_{cluster}$	$\geq 2,\ \leq 4$	$\geq 2,\ \leq 7$	$\geq 2,\ \leq 15$
N_{lepton}	$\geq 1,\ \leq 3$		
$N_{lepton+\gamma}$	≥ 2		
Veto: identified e	—	Yes	—
Veto: identified μ	Yes	—	—
Veto: identified τ	Yes	Yes	—
Acollinearity	$> 0.3\ rad$	$> 0.2\ rad$	—
Acoplanarity	$< 2.94\ rad$	$< 2.89\ rad$	$< 3.04\ rad$
$\sin(\theta(P_{missing}))$	> 0.4	> 0.3	—
E_{25}	$< 4\ GeV$	$< 10\ GeV$	$< 2\ GeV$
E_{ll}	$< 30\ GeV$	—	—
$E_{ALR+Lumi}$	$< 10\ GeV$		$< 5\ GeV$
DCA_{best}	$< 5\ mm$		
$T_{best\ scint\ hit}$	$> -5\ ns, < 5\ ns$		

Table 6.4: Cut variables and their values for pre-selection of scalar leptons: $\tilde{e}$, $\tilde{\mu}$ and $\tilde{\tau}$.

- $M_{visible}$, the visible mass;
- P_t, the total transverse momentum;
- $P_{missing}$, the missing momentum;
- N_{track}, the number of good tracks, which require at least 15 hits and have a span of at least 20 wires in the radial direction. Some other requirements on the transverse momentum, DCA and hit patterns are also applied;
- $N_{cluster}$, the number of calorimeter clusters with energy larger than 100 MeV;

- N_{lepton}, the number of identified leptons;
- $N_{lepton+\gamma}$, the total number of identified leptons and photons;
- Acollinearity, the space angle between the two most energetic leptons;
- Acoplanarity, the angle between the two most energetic leptons in the $r-\phi$ plane;
- $\theta(P_{missing})$, the polar angle with respect to the beam line of the missing momentum vector;
- E_{25}, the energy deposited in a cone of 25^o half opening angle around the missing momentum;
- E_{ll}, the visible energy other than the two most energetic lepton(s) and photon(s);
- $E_{ALR+Lumi}$, the sum of the energy deposited in the two small angle detectors, the active lead ring (ALR) and the luminosity monitor (LUMI);
- DCA_{best}, the best value (the one with the closest value to 0) of the distances of closest approach in the $r-\phi$ plane (DCA) for all good tracks;
- $T_{best\ scint\ hit}$, the best scintillator hit time. Here best means: closest to the beam crossing time plus the time of flight (the time to travel from the Interaction Point (I.P.) to the scintillator at light speed),

in which, the DCA_{best} and $T_{best\ scint\ hit}$ requirements remove all the cosmic contamination. The $E_{ALR+Lumi}$ cut removes tagged two-photon events. The P_t requirement removes beam gas events and a large number of two-photon events. Requiring $M_{visible}$ larger than 3 GeV in data is a must, since the Monte Carlo simulated two-photon processes have this cut at generator level. The N_{track} and $N_{cluster}$ requirements remove hadronic events and make sure that we have a leptonic final state. The N_{lepton}, $N_{lepton+\gamma}$ and veto cuts make sure that we have the correct number and flavor of identified leptons. In addition to these, the $E_{visible}$, $P_{missing}$, acollinearity and acoplanarity cuts help to select events with missing energy and unbalanced momentum.

The selected number of data and simulated events for all three scalar lepton flavors is listed in Table 6.5, for both 1999 and 2000. We observe good agreement between the selected data and the expected background level.

In addition, the distributions of the most important variables, i.e., those that will be used in the final selection, are further checked for their agreement between data and the Monte Carlo simulation. Figure 6.2 shows the variable distributions for $\tilde{e}$ after pre-selection, Figure 6.3 is for $\tilde{\mu}$ and Figure 6.4 is for $\tilde{\tau}$. In these figures, $E_{lepton1}$ is the energy of the most energetic lepton. The simulated scalar lepton

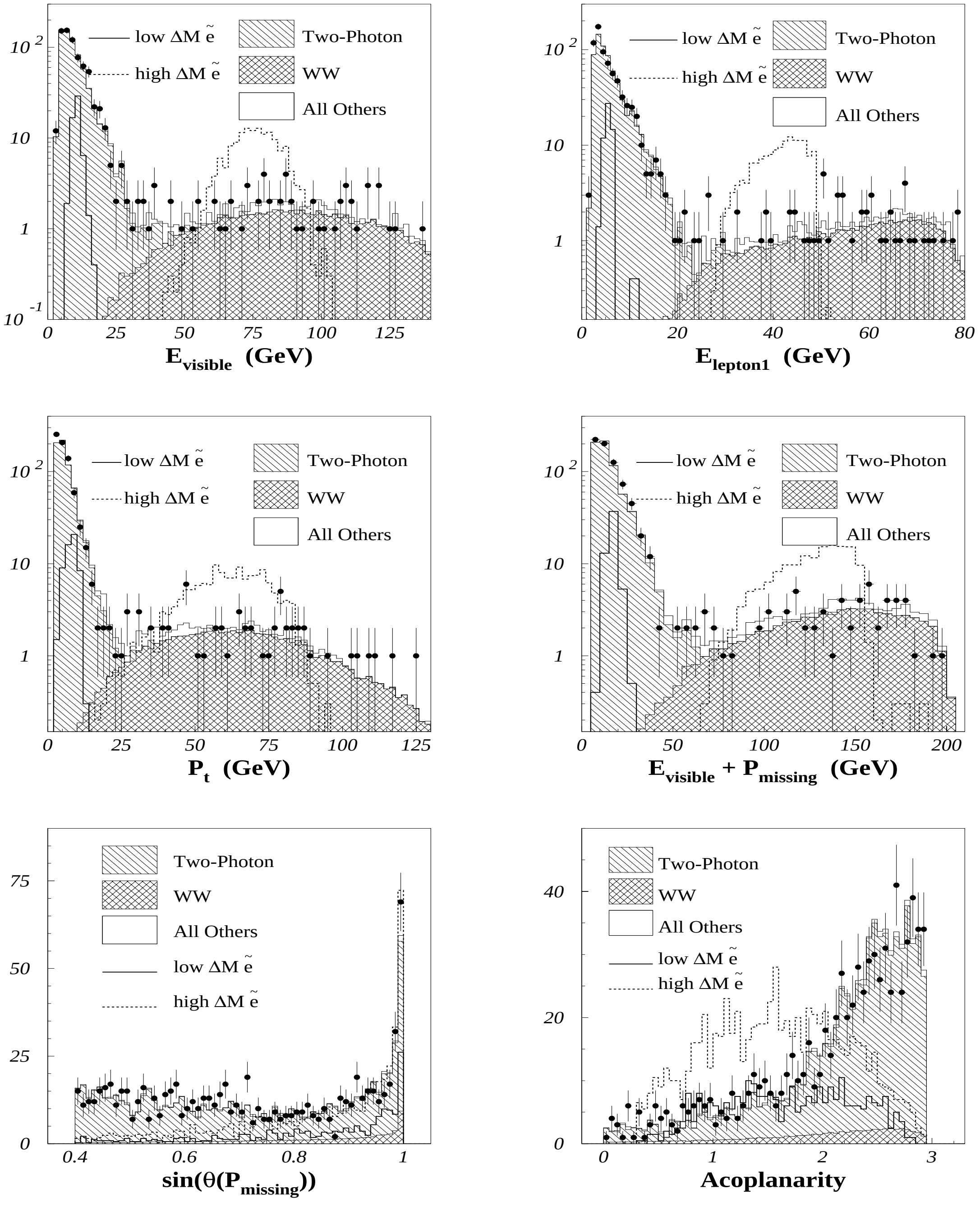

Figure 6.2: Data and Monte Carlo simulation agreement on important variables: after pre-selection for a scalar electron. Plots shown are for the data sample of 1999. The simulated $\tilde{e}$ signals with $M_{\tilde{e}} = 94\ GeV$ and $\Delta M = 5\ GeV$ (low), and with $\Delta M = 50\ GeV$ (high) are also shown.

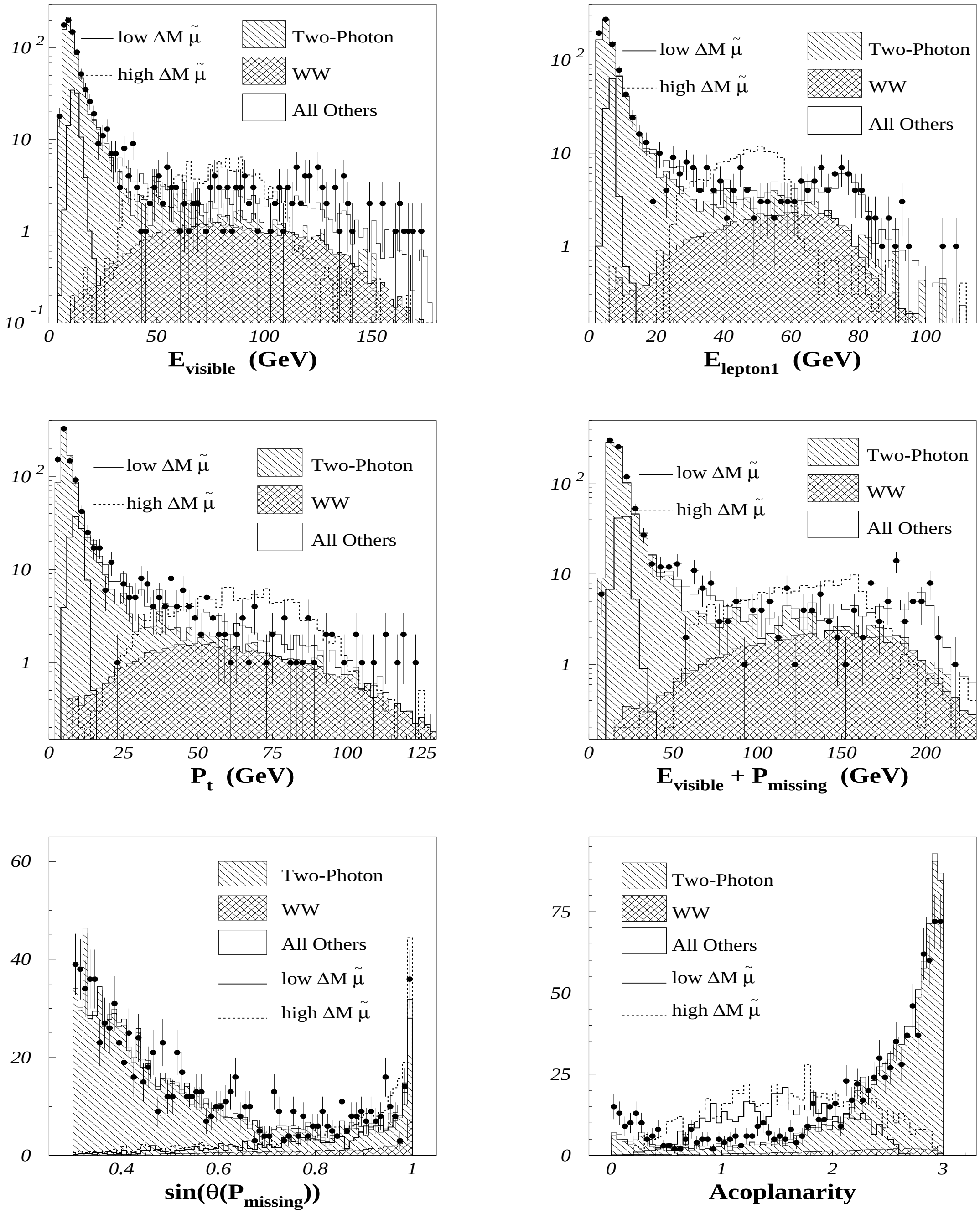

Figure 6.3: Data and Monte Carlo simulation agreement on important variables: after pre-selection for a scalar muon. Plots shown are for the data sample of 1999. The simulated $\tilde{\mu}$ signals with $M_{\tilde{\mu}} = 90\,GeV$ and $\Delta M = 5\ GeV$ (low), and with $\Delta M = 55\ GeV$ (high) are also shown.

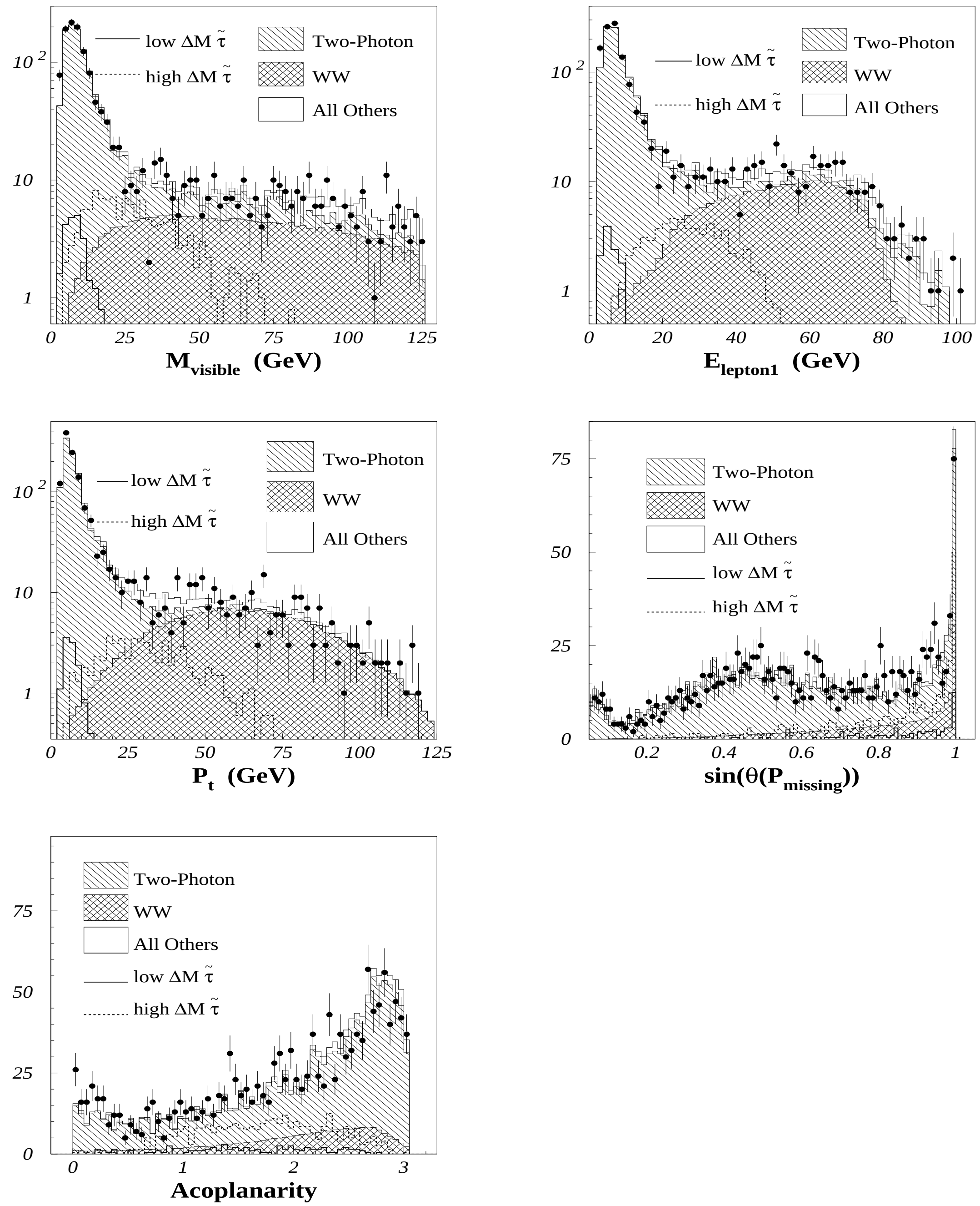

Figure 6.4: Data and Monte Carlo simulation agreement on important variables: after pre-selection for scalar a tau. Plots shown are for the data sample of 1999. The simulated $\tilde{\tau}$ signals with $M_{\tilde{\tau}} = 80\ GeV$ and $\Delta M = 6\ GeV$ (low), and with $\Delta M = 45\ GeV$ (high) are also shown.

Selection	$\tilde{e}$		$\tilde{\mu}$		$\tilde{\tau}$	
Year	N_{data}	N_{MC}	N_{data}	N_{MC}	N_{data}	N_{MC}
1999	771	755.2	963	929.8	1405	1391.2
2000	805	740.6	865	879.3	1202	1148.1

Table 6.5: Selected data and simulated background events after pre-selection for the three scalar leptons $\tilde{e}$, $\tilde{\mu}$ and $\tilde{\tau}$ using data from 1999 and 2000.

signals both in the low ΔM region and the high ΔM region with arbitrary normalization are also shown in these plots for comparison. The difference between the signature of a low ΔM signal and that of a high ΔM signal is quite obvious. All the distributions shown here are from the 1999 data sample. The distribution from the 2000 data sample gives similar results. We observe good agreement for all the variables studied, including those regions of the plots where the backgrounds would dominate even if scalar leptons were present, which suggests that we have well simulated Monte Carlo samples. We also observe that the dominant background is coming from two-photon processes and W-pair production, which is what we expected.

6.2.2 Selection optimization

The final selections are optimized for each scalar lepton flavor. The ΔM dependence of the final state signature is taken into account by a parametrized selection, which consists of a few parametrized cuts together with fixed cuts. The parameter used is defined as $Z = (\Delta M/M_{\tilde{l}}) \times E_{beam}$, to reflect the dependence on ΔM as well as $M_{\tilde{l}}$. The cut variables chosen for the final selections are listed in Table 6.6. Due to the difficulties of optimizing a parametrized selection, it is not possible to choose as many parametrized variables as a simple cut-based selection can do.

The parametrized cuts of each selection are optimized using Monte Carlo signal and background events. The optimization procedure selects a series of signal points with different ΔM and varies all cuts simultaneously to maximize the signal efficiency and the background rejection. We first discuss the optimization procedure in general, and then give details of the selection for each scalar lepton flavor.

Optimization procedure for parametrized selection

The parametrized selection is optimized with a series of Monte Carlo signal points at a fixed chosen $M_{\tilde{l}}$ with different ΔM values that cover the entire practical region from 3 GeV up to $M_{\tilde{l}} - 1\ GeV$. The $M_{\tilde{l}}$

Cut Variable	$\tilde{e}$	$\tilde{\mu}$	$\tilde{\tau}$
$M_{visible}$	—	—	parametrized
$E_{visible}$	parametrized	parametrized	—
E_{lepton_1}	parametrized	parametrized	parametrized
P_t	parametrized	parametrized	parametrized
$E_{visible} + P_{missing}$	parametrized	parametrized	—
$\sin(\theta(P_{missing}))$	> 0.40	> 0.45	> 0.70
Acollinearity	$< 2.80\ rad$	$< 2.80\ rad$	—
Acoplanarity	$< 2.84\ rad$	$< 2.84\ rad$	$> 0.30\ rad$
E_{25}	$< 2.0\ GeV$	$< 2.0\ GeV$	$< 2.0\ GeV$

Table 6.6: Cut variables chosen for the final selection of each scalar lepton flavor. The values of fixed cuts used for some of the variables are listed. Parametrized variables are denoted as 'parametrized,' as explained in this section.

for the optimization is chosen to be approximately the expected mass exclusion limit. The generated Monte Carlo signals also have the highest statistics for this mass and nearby regions, to make sure we have an accurate estimation of the signal efficiency as well as the best optimization in this region. The optimization mass chosen for $\tilde{e}$ is 94 GeV. For $\tilde{\mu}$ it is 90 GeV, and for $\tilde{\tau}$ it is 80 GeV.

To avoid biased optimization for a particular signal point ($M_{\tilde{l}}$, ΔM), signal events of nearby $M_{\tilde{l}}$ and ΔM are also included with a lower weight. In practice, we choose a central signal point ($M^c_{\tilde{l}}$, ΔM^c). The parameter Z is calculated from this central point $Z^c = (\Delta M^c / M^c_{\tilde{l}}) \times E_{beam}$. A small sample of events at ($M^c_{\tilde{l}}$, $\Delta M^c + \delta_1$) and ($M^c_{\tilde{l}} + \delta_2$, ΔM^c) is also included for the optimization by assigning it a small weight. We chose δ_1 to be $\pm(5\text{–}10)$ GeV, and δ_2 to be $+(5\text{–}10)$ GeV, $-(10\text{–}20)$ GeV. This specially prepared Monte Carlo signal sample is used to optimize the cut values together with the simulated background sample. After optimization, we get a series of cut values for each parameter value Z^c, we then fit the cut values as a function of the parameter Z^c, and thus get the parametrized selection. The details of the optimization and the fit of the parametrized selection are discussed below.

We optimize the signal efficiency and background rejection by minimizing the average cross section exclusion limit $\sigma_{95} = \bar{s}_{95}/(\epsilon\mathcal{L})$, for an infinite number of experiments, where $\mathcal{L}$ is the integrated luminosity of the data sample and ϵ is the selection efficiency of the signal. Since $\mathcal{L}$ is fixed, in practice we minimize $\kappa^{-1} = \bar{s}_{95}/\epsilon$. $\bar{s}_{95}$ is expressed mathematically by the following formula:

$$\bar{s}_{95} = \sum_{n=0}^{\infty} s_{95}(b,n)P(b,n), \tag{6.2}$$

in which, $s_{95}(b,n)$ is the 95% confidence level Bayesian upper limit, P(b,n) is the Poisson distribution for n events with an expected background of b events. $s_{95}(b,n)$ is determined from the following equation:

$$1 - C.L. = \sum_{i=0}^{n} \frac{(s+b)^i e^{-(s+b)}}{i!} / \sum_{i=0}^{n} \frac{b^i e^{-b}}{i!} \tag{6.3}$$

by setting $C.L. = 0.95$ (95% confidence level). In practice, we calculate $s_{95}(b,n)$ by solving the equation numerically.

The minimization process is controlled by the CERN MINUIT minimization package, which varies all the variables simultaneously and searches for the global minimum of a user defined function. However, it usually stops at a local minimum when the analytic properties of the function are poor.

Optimization for $\tilde{\mu}$

The signal Monte Carlo used for $\tilde{\mu}$ is at $M_{\tilde{\mu}} = 90\ GeV$, with twelve ΔM values: 3, 5, 10, 15, 25, 35, 45, 55, 65, 75, 85, and 89 GeV. As mentioned previously, the parameter Z is calculated using the central value of ($M_{\tilde{l}}^c = 90\ GeV$, ΔM^c), but we still take into account nearby signals.

The initial values for all the variables listed in Table 6.6 are set by comparing the distributions from background and corresponding signal. All variables are freely adjustable by MINUIT within a large enough range, except for the cut on E_{25} which has a fixed value. The results of the first optimization run showed that the cuts on three additional variables, $\sin(\theta(P_{missing}))$, Acollinearity, Acoplanarity, in addition to E_{25}, tend to have fixed values. The other four variables, however, change rapidly as ΔM gets larger. The values of these variables after the first optimization step are shown in Figure 6.5 as functions of the parameter Z. Although they have large fluctuations as Z gets larger, which prevents us from giving them a parametrization at this stage, we can see already that the cut values for some variables fall roughly on a curve, such as E_{lepton_1}, P_t and $E_{visible} + P_{missing}$. We then try to limit the range of cut values for one variable around a smooth curve, and see how the other optimal cut values change. Since there are correlations between these variables, we hope the values of other variables will get closer to forming smooth curves after the second stage of optimization.

Before we start the second optimization, we fix the values of the $\sin(\theta(P_{missing}))$, Acollinearity and Acoplanarity cuts at the values indicated by the first run. Then we give the variable P_t an initial value on a smooth curve roughly falling on the values we got from last run, and give them a smaller range

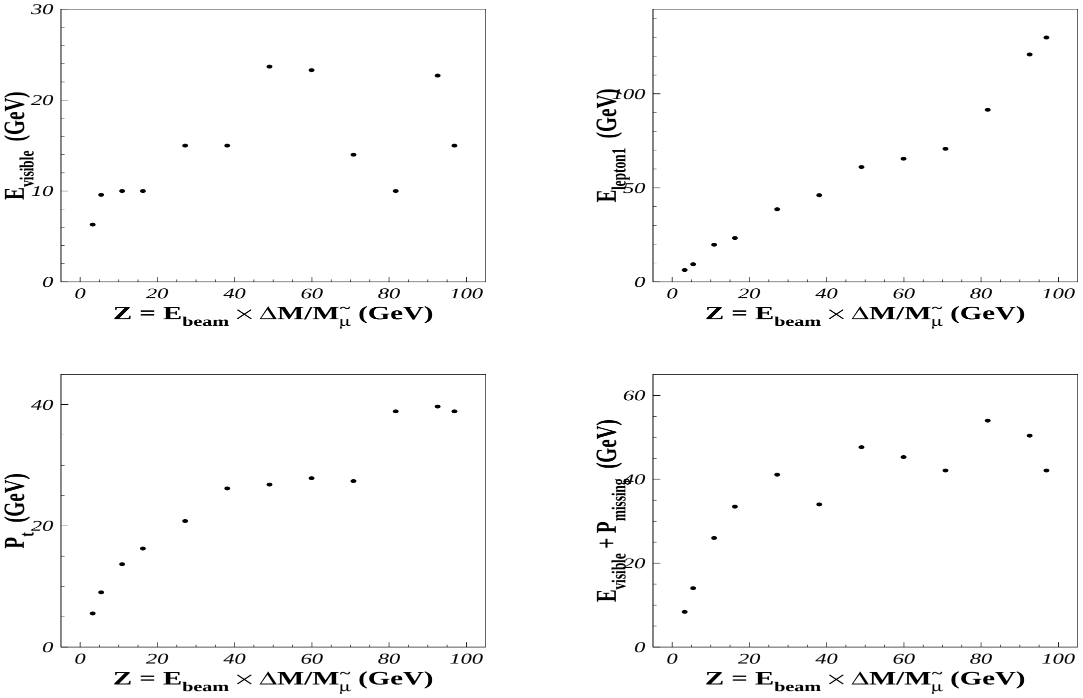

Figure 6.5: Value of the cut variables for $\tilde{\mu}$ selection, after the first optimization step. Each variable is shown as a function of the parameter Z.

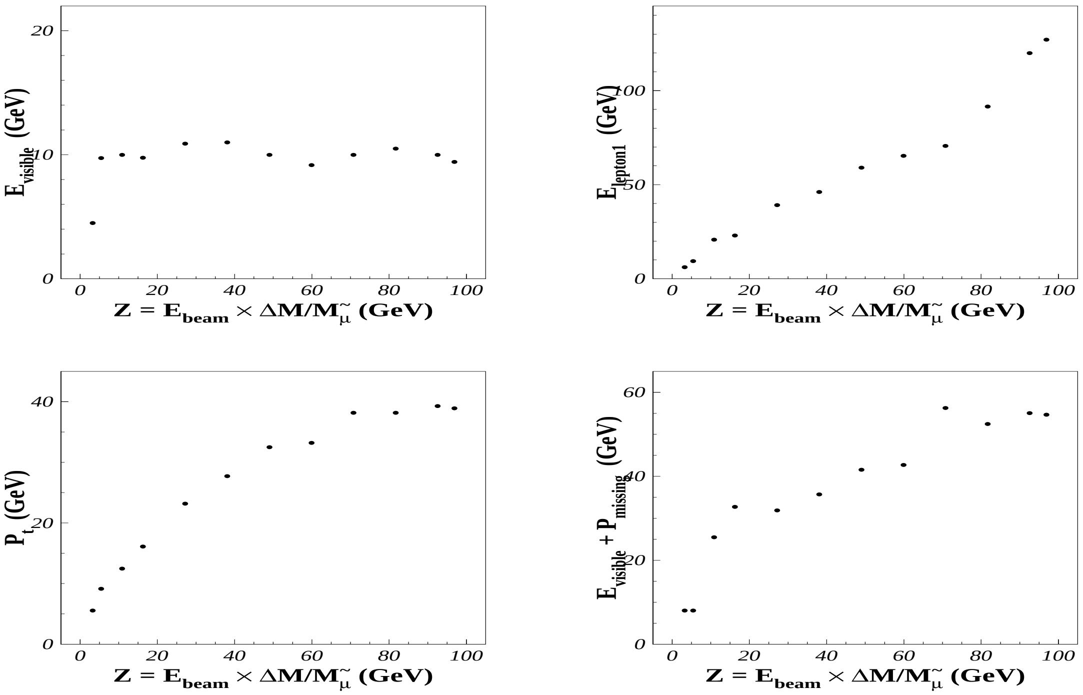

Figure 6.6: Value of the cut variables for $\tilde{\mu}$ selection, after the second optimization step. Each variable is shown as a function of the parameter Z.

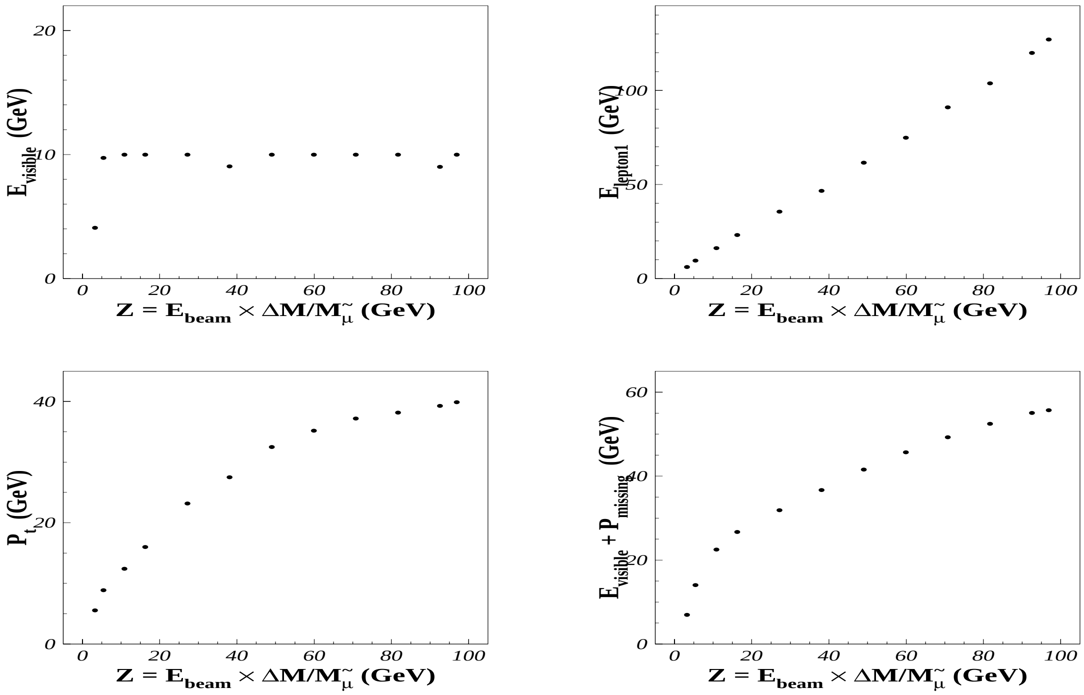

Figure 6.7: Value of the cut variables for $\tilde{\mu}$ selection, after the third optimization step. Each variable is shown as a function of the parameter Z.

for MINUIT to search for minimum. We also reduce the search range of the other variables, according to the results of the last run. The result of the second optimization is shown in Figure 6.6. This time, both the $E_{visible}$ and P_t values fall on a smooth curve, and the other two variables, E_{lepton_1} and $E_{visible} + P_{missing}$, also showed some improvement.

For the third optimization, we further reduce the range for $E_{visible}$ and P_t, and give E_{lepton_1} and $E_{visible}+P_{missing}$ initial cut values that fall on smooth curves that roughly fit the last results. The range of these variables are also reduced to a relatively small value. The result from the third optimization is shown in Figure 6.7. After the third optimization, all variables have cut values that fall on smooth curves.

Before we carry out the parametrization of the curves, we do a fourth optimization, where we use the results from the third run as the initial set of cut values, and give all the variables a little larger range (twice as large as that we used in the third run) to test if the result is robust. The result from this optimization is shown in Figure 6.8. No visible changes occur for any variable, which means we have achieved a quite stable result. The parametrization is then straightforward for all variables. We use

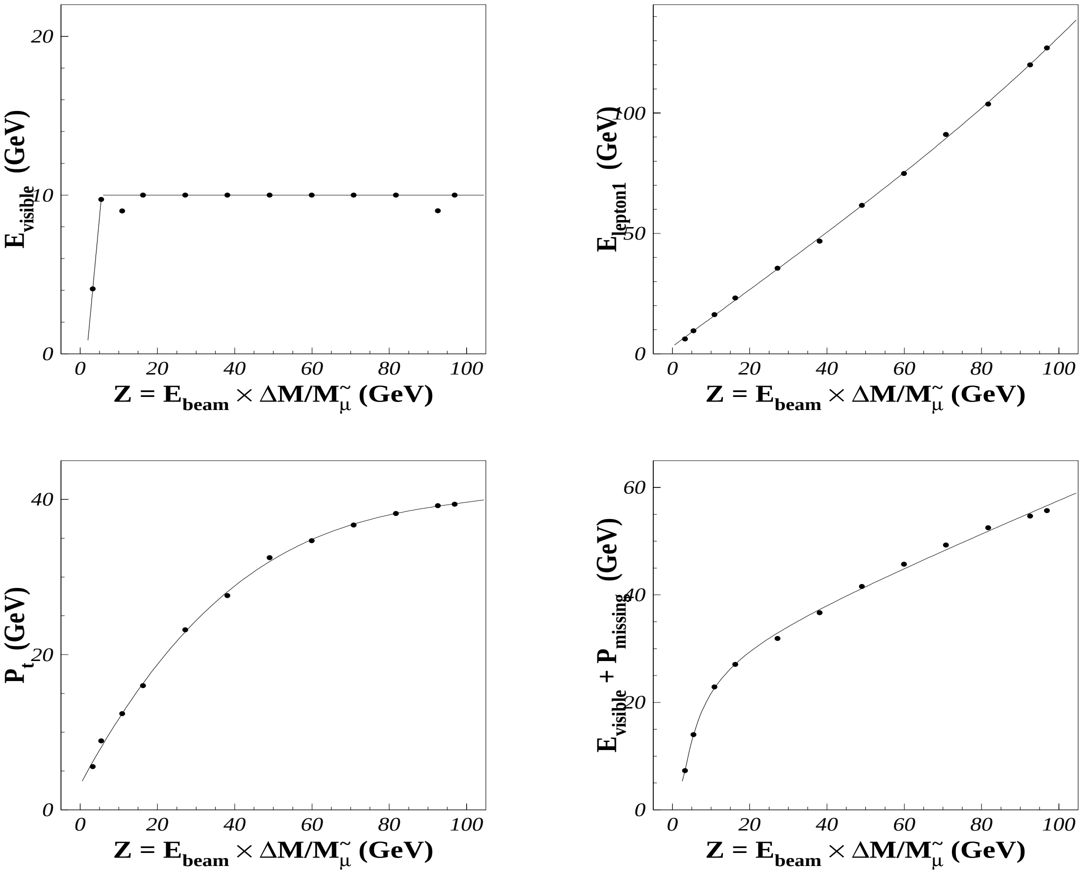

Figure 6.8: Value of the cut variables for $\tilde{\mu}$ selection, after the final optimization. Each variable is shown as a function of the parameter Z. The parametrization function for each variable is also shown in the plot.

smooth curves[3] for P_t, E_{lepton_1}, $E_{visible} + P_{missing}$, and use two joined straight lines for $E_{visible}$. The result of the parametrization is given in Table 6.7. These curves are also shown in Figure 6.8, together with the optimization result from the fourth run.

One question may arise after all these optimization and parametrization processes: did we sacrifice selection sensitivity by forcing the cut values onto a smooth curve? The answer is in Table 6.8, in which we show the values of the sensitivity function $\bar{s}_{95}/\epsilon$ we minimize, after each optimization. We didn't observe any significant loss in selection sensitivity, and we even observed a small gain in sensitivity for signals at a few ΔM values. This shows that

---

[3] For simplicity, we only considered the functional form $\sum_n c_n(Z^c)^n$, in which the c_n's are coefficients obtained from the fit. Usually we considered integer n, with $|n| \leq 3$, but occasionally, we also considered $n = \pm 1/2$.

final selection for $\tilde{\mu}$		
Cut Variable		Cut Value
$E_{visible}$	$>$	$-4.384 + 2.595Z$ (if $Z < 5.44$); 10.0 (if $Z > 5.44$) (GeV)
E_{lepton_1}	$<$	$3.033 + 1.193Z - 8.541 \times 10^{-4}Z^2 + 1.778 \times 10^{-5}Z^3$ (GeV)
P_t	$>$	$3.226 + 0.9325Z - 8.376 \times 10^{-3}Z^2 + 2.692 \times 10^{-5}Z^3$ (GeV)
$E_{visible} + P_{missing}$	$>$	$135.9Z^{-2} - 115.1Z^{-1} + 28.82 + 0.2989Z$ (GeV)
$\sin(\theta(P_{missing}))$	$>$	0.45
Acollinearity	$<$	2.80 rad
Acoplanarity	$<$	2.84 rad
E_{25}	$<$	2.0 GeV

Table 6.7: Cut variables and their parameterizations/values for the final selection used in searching for scalar muons.

- The global minimum of the selection sensitivity function is quite broad. We can move the selection in the nearby regions without losing significant sensitivity.

- In some ΔM regions, the parametrized selection is not the global minimum. This is mainly due to the limited Monte Carlo statistics for signal as well as background. The former affects the analytic property of the selection efficiency ϵ, while the later affects the average Bayesian upper limit $\bar{s}_{95}$.

The value of the sensitivity function cannot be turned into average cross section limit directly due to the fact that the Monte Carlo signal sample we used for the optimization contains a small fraction of events from nearby regions of the central point ($M^c_{\tilde{l}}$, ΔM^c) in the parameter space.

We summarize the results of our determination of an optimal parametrized selection below. In principle, we can always implement a parametrized selection for signals that vary according to one or more parameters. However, optimizing such a selection is not trivial due to the fact that usually we have only limited statistics for signal and background. In addition, since the cuts are generally not independent of each other, we cannot parametrize a lot of cut variables together in one selection. We tried in our selections for scalar leptons to use five or more parametrized cut variables, and it became very difficult to optimize due to increasing correlations between variables. We didn't lose selection sensitivity by forcing parametrized cut values, and found that this is mainly due to the nature of signal and the broad bottom near the minimum of the sensitivity function. By a parametrized selection, we

Runs		Value of sensitivity function $\bar{s}_{95}/\epsilon$ after optimization											
	ΔM (GeV)	3.	5.	10.	15.	25.	35.	45.	55.	65.	75.	85.	89.
	Z (GeV)	3.3	5.4	10.9	16.3	27.2	38.1	49.0	59.9	70.8	81.7	92.6	96.9
1st		107.5	48.6	16.9	15.2	18.5	21.0	23.8	25.6	27.6	27.7	26.8	27.2
2nd		105.8	48.7	17.0	15.0	18.7	20.9	24.0	25.7	27.8	27.6	26.7	27.2
3rd		105.5	48.1	18.6	15.3	18.9	21.0	24.0	27.1	28.7	27.6	26.7	27.3
4th		105.5	48.1	18.6	15.3	18.9	21.0	24.0	27.1	28.7	27.6	26.7	27.3

Table 6.8: Evolution of selection sensitivity for the four optimizations.

now have good sensitivity for any signals within the parameter space we are interested in.

Given the detailed optimization procedure and the results for scalar muon selection, we will only present the results of the optimization for scalar electron and scalar tau selection, since they follow the same procedure.

Optimization for $\tilde{e}$

The signal Monte Carlo used for $\tilde{e}$ selection optimization is at $M_{\tilde{e}} = 94\,GeV$ with $\Delta M = 3$, 5, 10, 20, 30, 40, 50, 60, 70, 80, 90, and 93 GeV. The optimization procedure is the same as we described before for the scalar muon, and it takes three optimization runs to reach the final cut values for parametrization. Four parametrized cut variables are chosen together with four other fixed cuts. The final optimized values for the parametrized cut variables are shown in Figure 6.9, together with the parametrized curves. The parameterizations/values of all cut variables are also listed in Table 6.9.

Optimization for $\tilde{\tau}$

The signal Monte Carlo used for $\tilde{\tau}$ selection optimization is at $M_{\tilde{\tau}} = 80\,GeV$ with $\Delta M = 3$, 4, 6, 10, 15, 25, 35, 45, 55, 65, 75, and 79 GeV. The optimization procedure is the same as we described before for the scalar muon, and it takes four optimization runs to reach the final cut values for parametrization. Three parametrized cut variables are chosen together with three other fixed cuts. The final optimized values for the parametrized cut variables are shown in Figure 6.10, together with the parametrized curves. The parameterizations/values of all cut variables are also listed in Table 6.10.

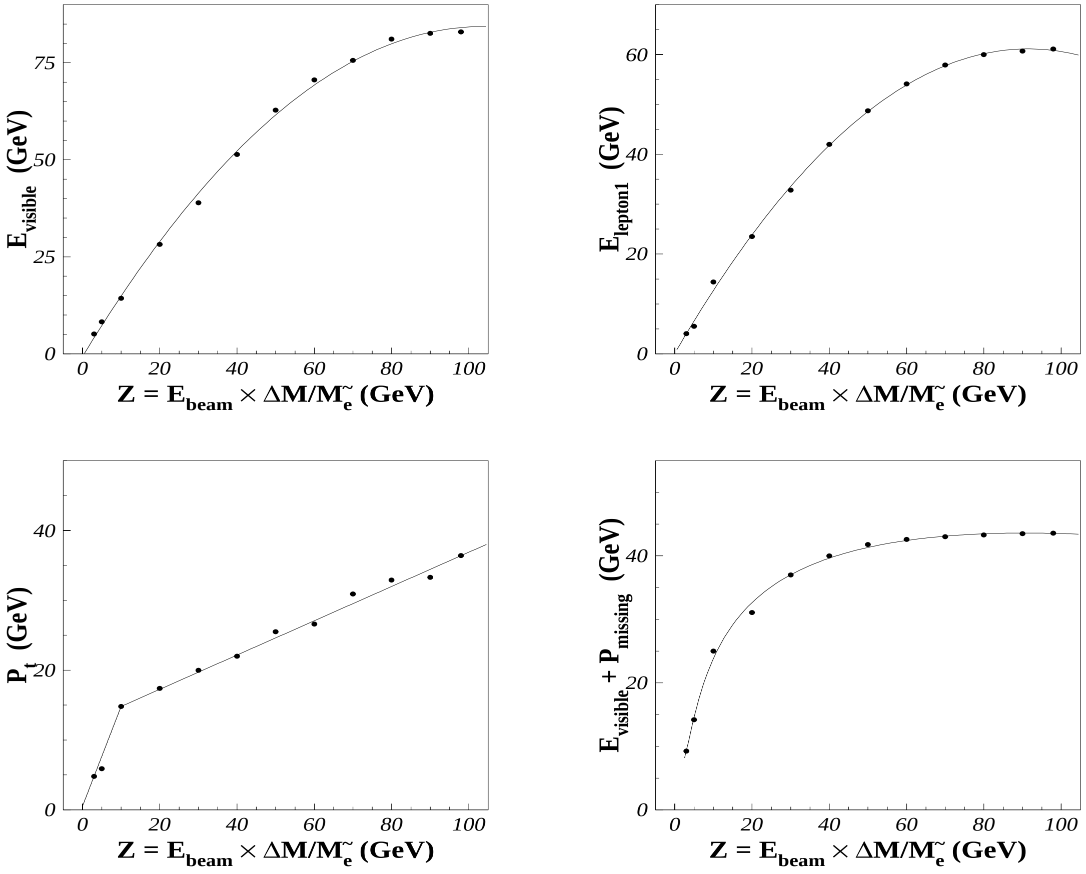

Figure 6.9: Value of the cut variables for $\tilde{e}$ selection, after final optimization. Each variable is shown as a function of the parameter Z. The parametrization function for each variable is also shown in the plot.

6.2.3 Parametrized selection

We apply the optimal parametrized selection for scalar leptons to the data samples obtained in the L3 detector during 1999 and 2000. For any $M_{\tilde{l}}$, we now have available selections for all ΔM by varying the parameter Z from 0 GeV to $M_{\tilde{l}}$. The selection efficiency is estimated by a series of Monte Carlo sample points in the parameter space. The $M_{\tilde{l}}$ interval between the generated signal points in this space is 10 GeV, and $M_{\tilde{l}}$ ranges from 45 GeV to the kinematic limit. The mass region below 45 GeV was excluded by LEP I data at the Z^0 peak already. The ΔM interval varies from $2-5$ GeV at low ΔM to $10-20$ GeV at medium and high ΔM, and ΔM ranges from 3 GeV to $M_{\tilde{l}} - 1$ GeV. The signal efficiency at each simulated point is calculated by applying the corresponding parametrized selection. The efficiency at any other point is calculated using linear extrapolation.

The number of selected events remaining after the cuts are shown in Figure 6.11 as we vary the

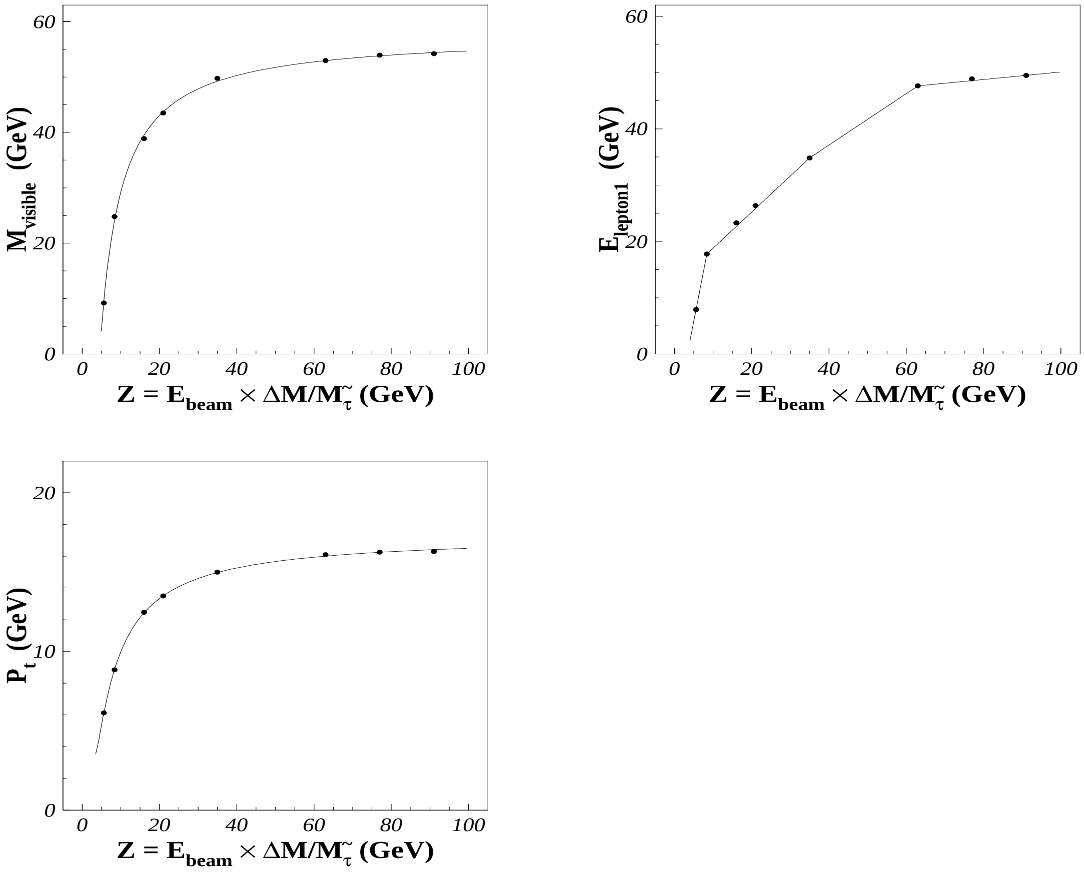

Figure 6.10: Value of the cut variables for $\tilde{\tau}$ selection, after final optimization. Each variable is shown as a function of the parameter Z. The parametrization function for each variable is also shown in the plot.

		final selection for $\tilde{e}$
Cut Variable		Cut Value
$E_{visible}$	$>$	$-0.7403 \ + \ 1.6420Z \ - \ 7.923 \times 10^{-3}Z^2 \ (GeV)$
E_{lepton_1}	$<$	$9.164 \times 10^{-2} \ + \ 1.334Z \ - \ 7.290 \times 10^{-3}Z^2 \ (GeV)$
P_t	$>$	$0.5143 \ + \ 1.429Z$ (if $Z < 10$); $12.35 \ + \ 0.2455Z$ (if $Z > 10$) (GeV)
$E_{visible} + P_{missing}$	$>$	$114.7Z^{-1} \ - \ 158.5Z^{-0.5} \ + \ 62.52 \ - \ 4.308 \times 10^{-4}Z^2 \ (GeV)$
$\sin(\theta(P_{missing}))$	$>$	0.40
Acollinearity	$<$	2.80 rad
Acoplanarity	$<$	2.84 rad
E_{25}	$<$	2.0 GeV

Table 6.9: Cut variables and their parameterizations/values for the final selection used in the search for scalar electrons.

parameter Z from 0 GeV to E_{beam} for each parametrized selection for the three scalar lepton flavors: $\tilde{e}$, $\tilde{\mu}$, and $\tilde{\tau}$, together with expected background level from Standard Model processes. The results from both 1999 and 2000 are shown. All of the three selections have consistent results between 1999 and 2000, and the selected number of data events is in good agreement with the Standard Model expectation. In the low ΔM region, the main background is from two-photon processes, while at high ΔM, W-pair production dominates.

The number of selected data and expected background events in each ΔM region are also summarized in Table 6.11. The three ΔM regions are defined using the selection parameter Z: low ΔM, $Z < 10 \, GeV$; medium ΔM, $10 \, GeV < Z < 30 \, GeV$; high ΔM, $Z > 30 \, GeV$. Typical signal efficiency is shown in Table 6.12. No significant indication of scalar lepton production has been observed.

6.3 Results

Having the selection and the result from the 1999 and 2000 data, as well as that from all previous years' LEP2 running, we didn't observe any excess of events or any significant indication of scalar lepton production. We now turn our results into various exclusion limits. All the limits presented in the following represent the combined result from all the data samples from LEP2 running taken at L3 whenever possible. The limits are always calculated at 95% confidence level. The calculation is carried out using the likelihood ratio method [76]. Use of this methodology automatically takes care of problems such as multi-sample combination and error propagation, but also requires generating large amount of Monte Carlo test experiments. In all cases, we generated enough events so that the results are unaffected by the Monte Carlo statistics of the test experiments.

6.3.1 Model independent cross section limit

Since no significant excess of events is observed in our search, we set upper limits on the scalar lepton production cross sections. Exclusion limits at 95% C.L. are derived taking into account the background contributions.

Traditionally, there are two approaches to obtain this limit. One takes the data sample as a whole, and calculates the cross section limit according to the total number of selected events, the expected background level and the total integrated luminosity, ignoring the different cross sections at different center-of-mass energies. The limit from this approach can be treated as a luminosity weighted average absolute upper limit on a certain process, and thus, is model independent. The other approach uses a cross section scaled luminosity, or as we did here, for any particular signal point ($M_{\tilde{l}}$, ΔM), we keep the ratio of the cross sections at the different center-of-mass energies ($\sigma_{\sqrt{s}_1} : \sigma_{\sqrt{s}_2} : ... : \sigma_{\sqrt{s}_n}$) and let the likelihood ratio method take care of the combination of several data samples. In this way, we search for a scaling factor α, by which a scalar lepton production process with cross sections ($\alpha{\cdot}\sigma_{\sqrt{s}_1}, \alpha{\cdot}\sigma_{\sqrt{s}_2}, ..., \alpha{\cdot}\sigma_{\sqrt{s}_n}$) at center-of-mass energies ($\sqrt{s}_1, \sqrt{s}_2, ..., \sqrt{s}_n$) is excluded at 95% confidence level. To this extent, we also call it a model independent limit.

Assuming a branching fraction for $\tilde{l}^{\pm} \to \tilde{\chi}_1^0 l^{\pm}$ of 100%, upper limits are set on the pair production cross sections at $\sqrt{s} = 205\ GeV$ of scalar electrons, muons and taus in the $M_{\tilde{\chi}_1^0}$ versus $M_{\tilde{l}}$ plane, as shown in Figure 6.12.

6.3.2 Scalar Lepton mass exclusion limit

We interpret our analysis result in the framework of the CMSSM with Grand Unification assumptions [77]. We investigate the following MSSM parameter space:

$$\begin{array}{rcl rcl} 1 \leq & tan\beta & \leq 60, & 0\,GeV \leq & M_2 & \leq 2000\,GeV, \\ -2000\,GeV \leq & \mu & \leq 2000\,GeV, & 0\,GeV \leq & m_0 & \leq 500\,GeV. \end{array}$$

The interpretation of the search result presented here does not depend on the value of A_0. We then translate the limits on the cross sections previously shown and the SUGRA interpretation into exclusion regions in the MSSM parameter space.

In general, the SUSY partners of the right-handed leptons ($\tilde{l}_R$) are expected to be lighter than their counterparts for left-handed leptons. We show in Figure 6.13 the excluded region at the 95% confidence level, in the $M_{\tilde{\chi}_1^0} - M_{\tilde{l}}$ plane considering only the reaction $e^+e^- \to \tilde{l}_R^+\tilde{l}_R^-$ with decay mode $\tilde{l} \to l\tilde{\chi}_1^0$, at $\mu = -200\ GeV$ and $tan\beta = 2.0$. These exclusion limits hold also for higher $tan\beta$ and $|\mu|$ values. For smaller $|\mu|$ values, the t-channel contribution to the scalar electron cross section is reduced, thus reducing the scalar electron limit by approximately $2 - 3\ GeV$.

For large enough ΔM, we observe

$$M_{\tilde{e}_R} > 97\ GeV \quad (\textit{expected}\ 97\ GeV) \tag{6.4}$$

$$M_{\tilde{\mu}_R} > 86\ GeV \quad (\textit{expected}\ 86\ GeV) \tag{6.5}$$

$$M_{\tilde{\tau}_R} > 78\ GeV \quad (\textit{expected}\ 79\ GeV). \tag{6.6}$$

The expected limits are the average limits obtained from a large number of Monte Carlo experiments generated according to the probability density functions of all the possible results.

		final selection for $\tilde{\tau}$
Cut Variable		Cut Value
$M_{visible}$	$<$	$176.0Z^{-2} - 302.1Z^{-1} + 57.72$ (GeV)
E_{lepton_1}	$>$	$-11.84 + 3.525Z$ (if $Z < 8.4$); $12.38 + 0.6417Z$ (if $8.4 < Z < 35.0$); $18.85 + 0.4568Z$ (if $35.0 < Z < 63.0$); $43.42 + 6.679 \times 10^{-2}Z$ (if $Z > 63.0$) (GeV)
P_t	$>$	$136.7Z^{-2} - 87.43Z^{-1} + 17.36$ (GeV)
$\sin(\theta(P_{missing}))$	$>$	0.70
Acoplanarity	$>$	0.30 rad
E_{25}	$<$	2.0 GeV

Table 6.10: Cut variables and their parameterizations/values for the final selection used in the search for scalar taus.

Scalar Lepton	low ΔM		medium ΔM		high ΔM		combined	
Flavor	N_{data}	N_{MC}	N_{data}	N_{MC}	N_{data}	N_{MC}	N_{data}	N_{MC}
$\tilde{e}$	37	44.0	9	13.7	27	31.9	69	82.6
$\tilde{\mu}$	78	71.8	25	26.2	62	54.5	146	132.8
$\tilde{\tau}$	177	147.2	79	64.4	66	66.5	229	202.0

Scalar Lepton	low ΔM		medium ΔM		high ΔM		combined	
Flavor	N_{data}	N_{MC}	N_{data}	N_{MC}	N_{data}	N_{MC}	N_{data}	N_{MC}
$\tilde{e}$	42	40.6	10	13.7	23	24.6	68	71.3
$\tilde{\mu}$	73	66.2	21	21.6	46	50.6	123	120.6
$\tilde{\tau}$	140	123.1	67	60.0	56	56.9	181	169.1

Table 6.11: Results of scalar lepton analysis: the selected number of data events and the expected Standard Model background in each ΔM region and combined. Top: results from the 1999 data sample; bottom: results from the 2000 data sample.

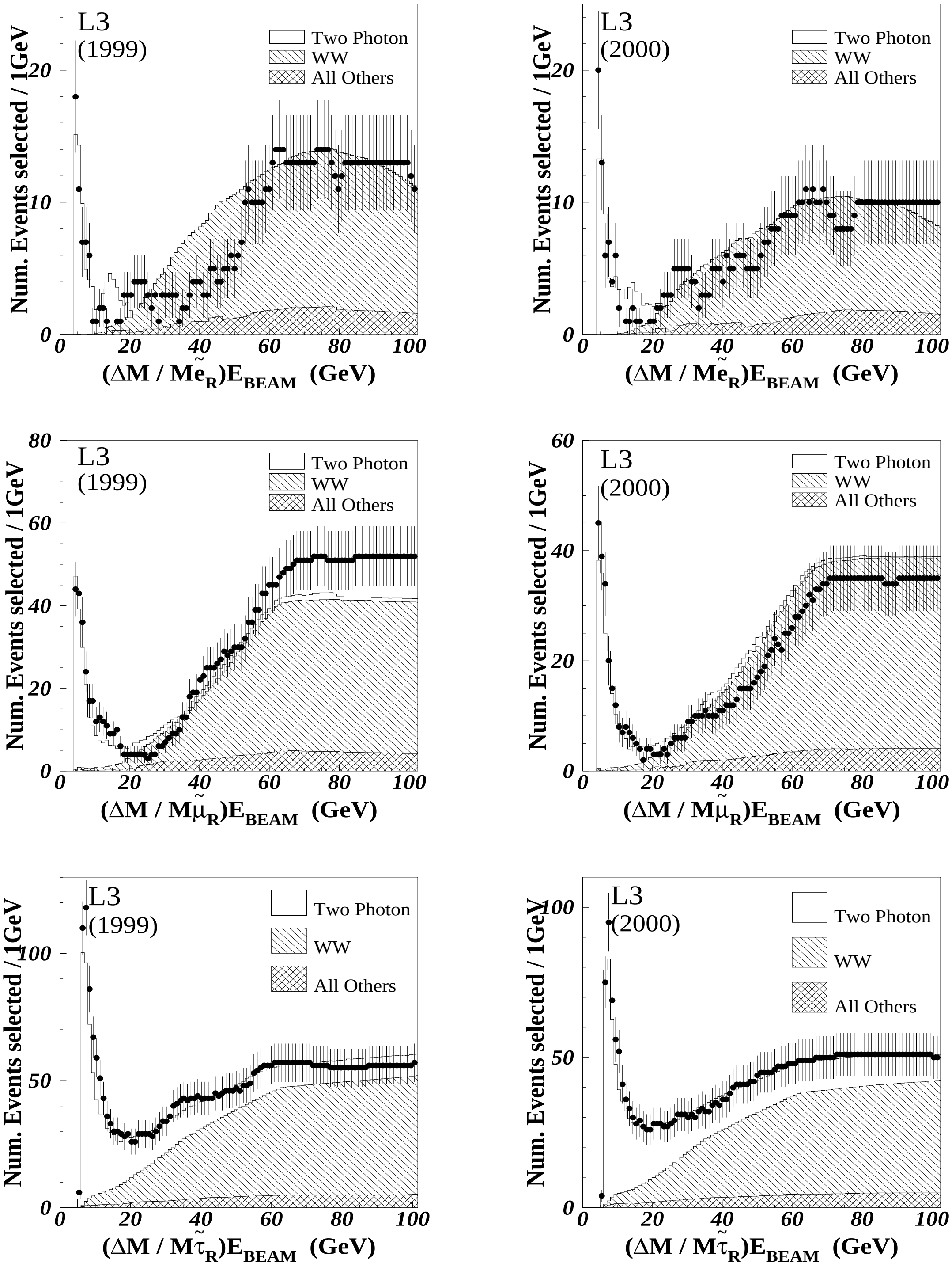

Figure 6.11: Selected data events and expected background level as a function of the parameter $Z = (\Delta M/M_{\tilde{l}}) \times E_{beam}$, for $\tilde{e}, \tilde{\mu}, \tilde{\tau}$ selection using data from 1999 and 2000.

$\sqrt{s} = 205\ GeV$			
ΔM	$\epsilon\ (M_{\tilde{e}} = 94\ GeV)\ \%$	$\epsilon\ ((M_{\tilde{\mu}} = 90\ GeV)\ \%$	$\epsilon\ ((M_{\tilde{\tau}} = 80\ GeV)\ \%$
3	4.4	10.0	0.0
4	7.4	22.7	0.5
5	10.3	29.5	2.7
7	13.8	41.7	5.0
10	22.3	50.9	11.0
20	44.4	50.9	23.5
30	44.8	52.4	29.2
40	43.6	54.6	30.4
50	42.9	55.6	30.3
60	37.9	56.3	29.1
70	34.6	57.0	29.2
80	31.6	56.0	—
90	29.4	—	—

Table 6.12: Typical selection efficiency for three scalar lepton flavors.

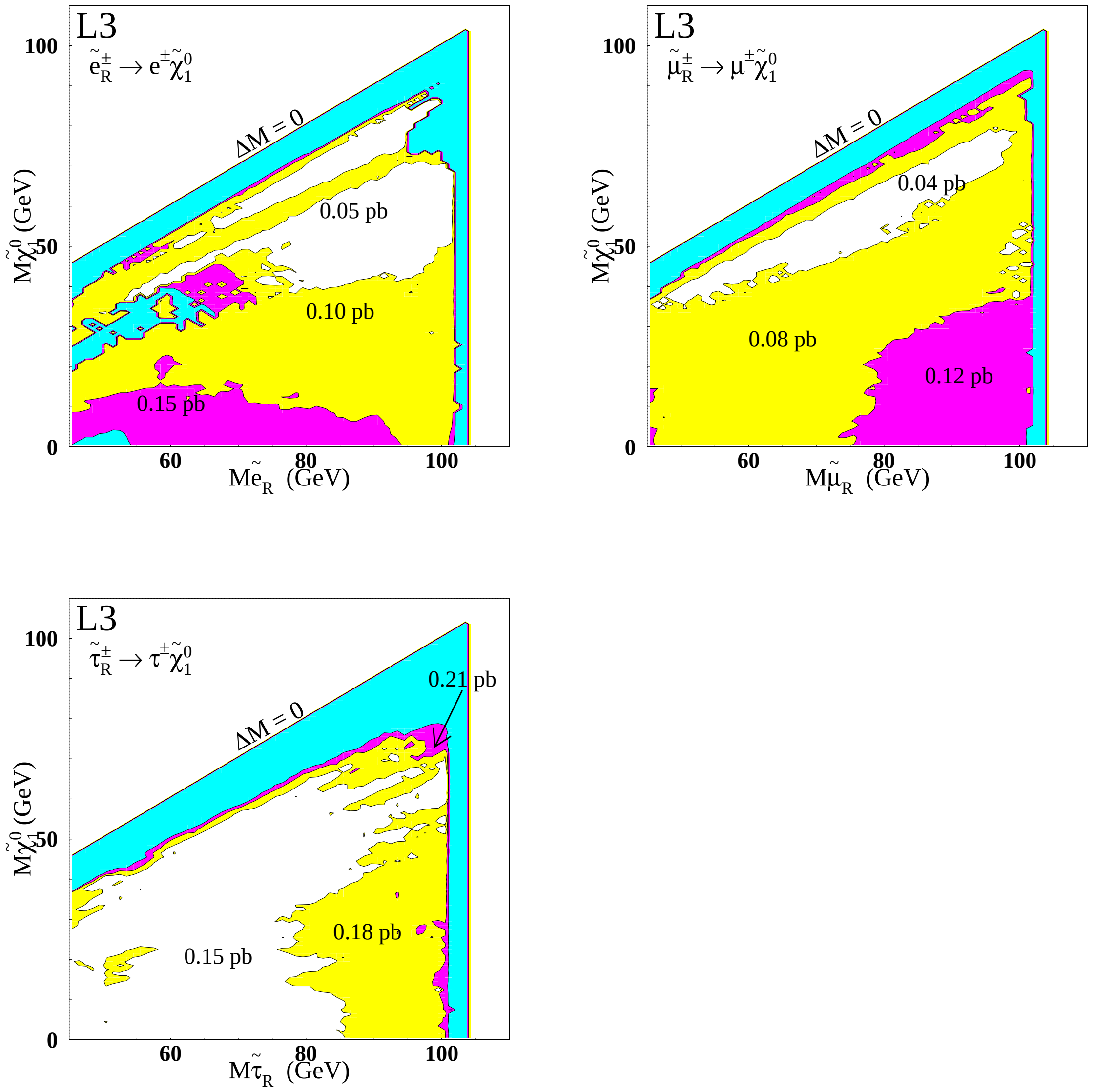

Figure 6.12: Model independent limit on the production cross section at $\sqrt{s} = 205\,GeV$, in the $M_{\tilde{\chi}^0_1} - M_{\tilde{l}}$ plane, for all three scalar lepton flavors.

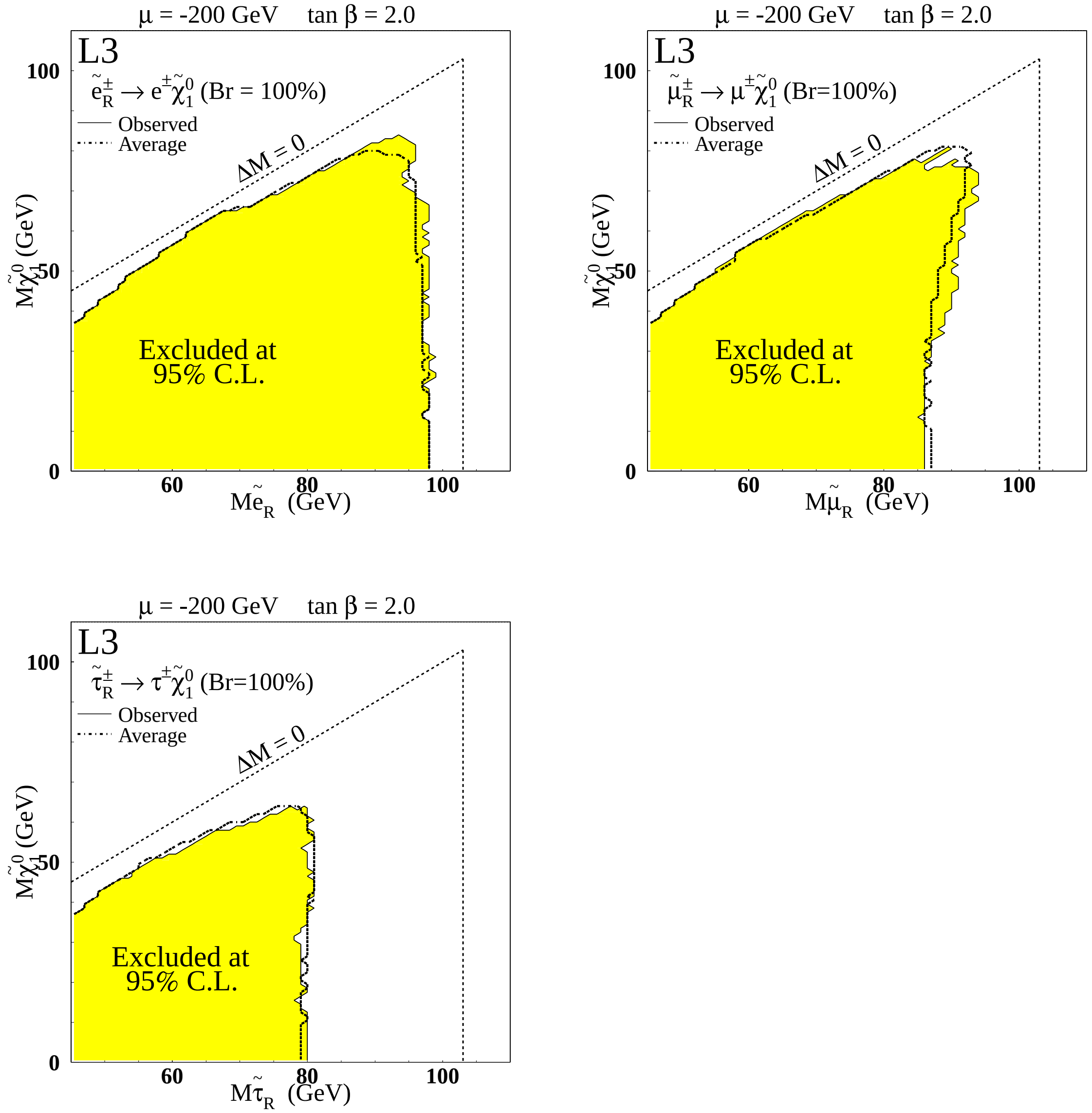

Figure 6.13: Excluded region at 95% C.L. in the $M_{\tilde{\chi}^0_1} - M_{\tilde{l}}$ plane, for three scalar lepton flavors.

7. Search for Scalar Taus in GMSB Models

Assuming the gravitino $\tilde{G}$ is the lightest supersymmetric particle (LSP), the event signature for scalar leptons in GMSB models depends strongly on its decay length. For a decay length less than $\sim 1\,mm$, there are two acoplanar leptons in the final state with missing energy from a pair of undetected gravitinos. This is exactly the same signature as the scalar leptons in gravity mediated SUSY breaking models, if we have $M_{\tilde{\chi}_1^0} \simeq 0$. For decay lengths ranging from $\sim 1\ mm$ to $\sim 1\ m$, we expect a large impact parameter and kinks. For even larger decay length, we search for a pair of back-to-back, heavy stable charged particles. In this analysis, 5 specific selections are optimized for the search for a scalar τ NLSP, in the cases of prompt decay (1 selection), short to medium decay length (2 selections), and long decay length (2 selections).

We have already solved some simulation issues in particle decays with long decay length, and in the TEC dE/dx Monte Carlo, as shown in Chapter 5. We present here a further technical issue, in the use of the new particle group ntuple, before we get to the analysis searching for scalar taus in GMSB models.

7.1 Upgraded new particle group ntuple

As we discussed in Section 6.1, the new particle group ntuple provides enough information for most physics analyses, and it significantly reduced the overall workload in carrying out an analysis. We encounter a special case, however, in the analysis of scalar taus in GMSB models. In this analysis, due to the possible long decay length, we need detailed information on every reconstructed track, as well as some more information about the scintillator hits and muon tracks. Since we have low multiplicity events, b-tagging variables simply cannot help us. An obvious solution, which I carried out as summarized below, was to upgrade the new particle group ntuple to a new version.

7.1.1 New particle group ntuple version 15

Unlike the L3 standard program packages which use CERN PATCHY as the source code management system, the production code for the new particle group ntuple uses CVS to manage the code and program version. CVS provides a more friendly environment for code development and handling, and the upgrade turned out to be straightforward, with just three data blocks added to the ntuple structure:

- block for TEC tracks: we list in this block the reconstructed TEC tracks up to the 10th most energetic one, including physics quantities for each track such as their signed momentum ($q \cdot P$), θ and ϕ angles, DCA (distance of closest approach in the $r - \phi$ plane), Z_0 (Z coordinate of the point on the track where the DCA in the $r - \phi$ plane is achieved), total number of hits, span of the hits, two words of hit pattern which record in their bits the fired wires (L3 TEC has 62 sense wires along radial direction), χ^2 of the track fit, as well as the dE/dx of the track[1], etc.;
- block for muon chamber tracks: list up to the 10 most energetic muon tracks, including their signed momentum, θ and ϕ angles, DCA, Z_0, and matched scintillator time, etc.;
- block for scintillator hits: list up to 15 scintillator hits with the time and the hit scintillator counter number of the hit.

This upgraded version of the new particle group ntuple is called version 15 (np15).

7.1.2 New particle group ntuple production for version 15

Since the standard production of a full data/Monte Carlo sample takes a rather long time and is basically out of the control of the physics analysis group, we decided to do the production run for the data/Monte Carlo samples for 1999 and 2000 by ourselves. To accelerate the production process, we utilized the fast rejection algorithm in the L3 reconstruction program which uses a small amount of information to decide whether to keep an event at the beginning of the whole reconstruction process. We rejected a large number of beam gas events and hadronic final states with high multiplicity through this mechanism, which saved a lot of running time.

However, the production process is still quite time consuming. It takes more than a month to run a complete data/Monte Carlo set of one year's LEP running, using 3 out of the 32 CPUs of the L3 batch job server and two dedicated PCs. Finally, we ran on the last two years' LEP data (1999 and 2000) at

---

[1] If it is a Monte Carlo event, values calculated from both the new and old versions of the dE/dx simulation are recorded.

high energy, ranging from $\sqrt{s} = 192\,GeV$ to $208\,GeV$, which is the most important data sample for this analysis.

7.2 Event selection and optimization

Due to the different signatures from the various possible decay lengths, it is impossible to have a single selection to cover all the cases, not even one at pre-selection level. So we developed dedicated selections for each decay length case, from pre-selection level to the final selection. All the final selections are optimized using the same method as we discussed in Section 6.2.2: we vary all the cut variables simultaneously and try to minimize $\bar{s}_{95}/\epsilon$ which is proportional to the average cross section exclusion limit.

An important issue for the analysis of scalar taus in GMSB models is how to get the background from cosmics under control, especially when the decay length is visible. Usually one can easily remove cosmic rays from the data sample by applying a strict DCA cut and requiring in-time scintillator hit(s). However, it is not so easy for the current analysis since we have particles decaying from secondary vertices which means large DCA, as well as heavy stable charged particles which means they travel rather slowly and cannot get to the scintillator in time. This problem is solved in quite different ways in each decay length case.

The following sections discuss the selection details for each case. The selection for prompt decay is special compared to the others since it can use existing results from previous analysis. The selection for visible decay length consists of two similar selections for short and medium decay length, and will be discussed together. The long decay length case also contains two selections, one that uses kinematic cuts to cover the low $M_{\tilde{\tau}}$ region, and a second that uses TEC dE/dx information on the tracks that achieves high sensitivity in the high $M_{\tilde{\tau}}$ region.

7.2.1 Selection for scalar taus with prompt decay

For scalar taus in GMSB models, if the gravitino is very light ($m_{\tilde{G}}$ of order eV), the decay length of the scalar tau would be so short that the signature is indistinguishable from what we've studied in Chapter 6: a scalar tau in the $\tilde{\chi}_1^0$ LSP scenario when the mass of $\tilde{\chi}_1^0$ is close to 0. Thus, we don't need a new selection for scalar taus with prompt decay in GMSB models — the parametrized selection described in chapter 6 for scalar tau can do the job, by setting the parameter Z = E_{beam} ($M_{\tilde{\chi}_1^0} = 0\,GeV$,

$\Delta M = M_{\tilde{l}}$). However, we still need to know the exact performance of this selection on scalar tau signals with different decay lengths. A careful check of the efficiency at a series of simulated decay lengths and $\tilde{\tau}$ masses has been done. The result is shown in Table 7.1 bellow:

efficiency %	Decay Length (mm)							
$M_{\tilde{\tau}}$ (GeV)	10^{-3}	10^{-2}	0.1	1.0	10.0	100.0	400.0	MSSM $\tilde{\tau}$ ($M_{\tilde{\chi}_1^0} \simeq 0$ GeV)
45	25.1	22.7	22.6	23.4	18.3	2.9	1.3	23.3
65	28.9	29.3	29.2	28.3	20.9	3.9	1.9	29.2
85	32.6	32.0	32.3	31.3	23.1	3.6	2.3	31.6

Table 7.1: Efficiency of the $\tilde{\tau}$ signal at different decay lengths and mass, when applying the established parametrized selection at $Z = E_{beam}$. The efficiency of the $\tilde{\tau}$ signal in the $\tilde{\chi}_1^0$ LSP scenario at $M_{\tilde{\chi}_1^0} \simeq 0$ GeV is also shown in the last column for comparison.

For a decay length less than ~ 1 mm, the difference in selection efficiency for $\tilde{\tau}$ in GMSB models at different decay length is consistent with statistical fluctuations. And within statistical uncertainty, these efficiencies are equal to that for the $\tilde{\tau}$ signal in the $\tilde{\chi}_1^0$ LSP scenario at $M_{\tilde{\chi}_1^0} \simeq 0$ GeV, using the same selection. Thus all the results obtained for the latter case are valid for the current analysis, provided the corresponding decay length is less than ~ 1 mm.

7.2.2 Selections for scalar taus with visible decay length

In this section we focus on the signals with visible but still not very long decay length, i.e., at least one scalar tau decays inside the sensitive region of the L3 TEC. We implemented two impact parameter based selections targeted at slightly different decay lengths, one for short, the other for medium decay length.

We also tried searching for secondary vertices due to long-lived particle decay, but this has very low signal efficiency for any decay length, and does not contribute to the overall sensitivity. This is mostly detector limited, instead of being a selection problem. Considering the compact size of the L3 TEC, which has an active region from r = 10.98 cm to r = 42.72 cm, and the fact that a recognizable secondary vertex should have at least two tracks with a minimum of 8 - 10 hits each, the actual detectable secondary vertex must be in the radial range of $r \simeq 14$ cm to 39 cm for 1-prong tau decay, or in a slightly larger range ($r \simeq 5$ cm to 33 cm) for 3-prong tau decays. This is illustrated schematically

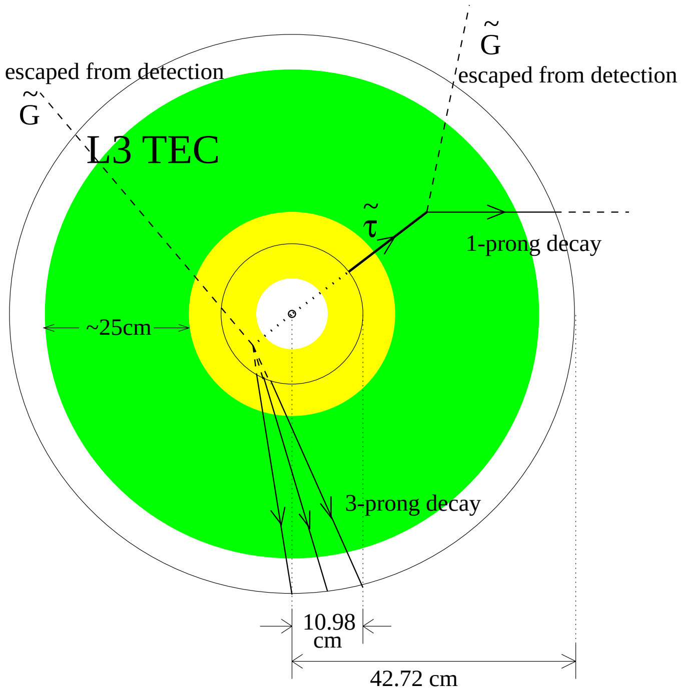

Figure 7.1: Detectable secondary vertexes are shown schematically. In the 1-prong decay mode the 2nd vertex must fall in the outer radial band, while in the 3-prong decay mode the 2nd vertex also may be detected in the inner band.

in Figure 7.1. Taking into account the fraction of scalar taus that can decay in this small range, the branching ratio and the detection efficiency for short tracks, the selection efficiency for finding a $\tilde{\tau}$ signal by requiring a secondary vertex does not exceed 15% for any particular $\tilde{\tau}$ signal. And in fact, the two selections based on the impact parameter can pick up most of these events.

In these selections, we do not depend on lepton identification due to possible large impact parameters and non-pointing calorimeter clusters. We use forced two-jet reconstruction instead to identify the two taus in the final state. So variables such as acollinearity and acoplanarity are calculated using the jet variables.

Pre-selections

Loose pre-selections are applied to two specific decay length regions. In the short decay length case, we focus on the small difference between tracks from the Interaction Point (IP) and those from a short lived particle decay. In this case, we can still apply tight cuts on the best DCA of the reconstructed tracks and the closest time from scintillator hits, to remove cosmic contamination. However, for the medium decay length case, this is no longer true and we applied some dedicated veto cuts to remove cosmic rays. The cuts for pre-selection are listed in Table 7.2. For the medium decay length selection, two additional veto cuts are applied. Events are rejected if

- $|DCA_{track1}| > 0.5\ mm$, $|DCA_{track2}| > 0.5\ mm$,
  and $|DCA_{track1} + DCA_{track2}|/(|DCA_{track1}| + |DCA_{track2}|) < 0.1$

- $DCA_{best} > 3\ mm$ and $T_{best\ scint} < -1\ ns$ or $> 2\ ns$,

in which track1 and track2 refer to the two most energetic tracks in the event. To understand the first veto cut, it is necessary to introduce the convention of signed DCA in L3 analysis, which is shown schematically in Figure 7.2. If a cosmic muon passes through the L3 central detector near the interaction point (IP) during a beam crossing, it will be detected by the L3 TEC and recognized as two charged particles flying out of the beam pipe, as shown in Figure 7.3. By definition in the L3 analysis, the two tracks will have two DCAs with similar magnitude but opposite sign. This is a typical signature for a cosmic muon [78], and if we plot the signed DCAs of the two most energetic tracks in a two-dimensional plane, the cosmics are sitting along a band around the line DCA(track1) + DCA(track2) = 0, as shown in Figure 7.4. Thus, the first veto cut can remove these events efficiently. The second veto cut is based on the fact that signal events from scalar tau either have short scintillator time but large best DCA (in case of relatively short decay length. Since decay products are light particles, they can reach the scintillator pretty fast), or have small best DCA but long scintillator time (in case of long decay length with primary scalar tau being detected). But for cosmics, this is not necessarily true. After these cuts, cosmic contaminations in our data sample can be neglected.

The number of selected data events and the expected background level from Standard Model processes for 1999 and 2000 are also shown at the bottom of Table 7.2. We also checked the distributions of all the important variables: Figure 7.5 shows the distributions after pre-selection for a scalar tau with short decay length, while Figure 7.6 shows the distributions after pre-selection for a scalar tau with medium decay length, in which the data and the simulated Monte Carlo distributions for the backgrounds agree very well.

Cut Variable	short decay length	medium decay length
DCA_{best}	$< 5\ mm$	—
$T_{best\ scint}$	$> -5\ ns,\ < 5\ ns$	$> -3\ ns,\ < 5\ ns$
Z_0	—	$< 40\ mm$
$N_{good\ tracks}$	≥ 2	≥ 2
$P_{most\ energetic\ track}$	$> 1.5\ GeV$	$> 4\ GeV$
$P_{2nd\ most\ energetic\ track}$	—	$> 1.5\ GeV$
$E_{visible}$	—	$> 18\ GeV$
$E_{visible} - P_{\mu(s)}$	—	$> 10\ GeV$
E_{25}	$< 2\ GeV$	—
$Acollinearity$	—	< 3.05
$Acoplanarity$	—	< 3.0
Width of jet	< 0.2	—
$E_{ALR+Lumi}$	$< 5\ GeV$	$< 5\ GeV$
additional veto cuts	No	Yes
year	selected N_{data} / N_{MC}	
1999	649/673.0	551/525.9
2000	635/602.2	443/451.3

Table 7.2: Cut variables and their values for the pre-selection of $\tilde{\tau}$ in GMSB models, with short and medium decay length.

Final selections

Final selections are optimized using signal and background simulations. The optimization procedure selects signal points with several decay lengths and varies all cuts simultaneously to maximize the signal efficiency and the background rejection. We optimized two selections focused on scalar taus with short and medium decay length. The cut variables and their optimized values are listed in Table 7.3. For a short decay length signal, we can reconstruct two good jets which reflect the acoplanar nature of the events. So we are able to put cuts on the acoplanarity and acollinearity of the jets. However, for a medium decay length, we may already observe the primary tracks from the scalar tau (before decay) which are back to back, and we are not sure about the jet reconstruction. In addition, we distinguish short and medium decay length mainly by one variable which is the average DCA from good tracks. We

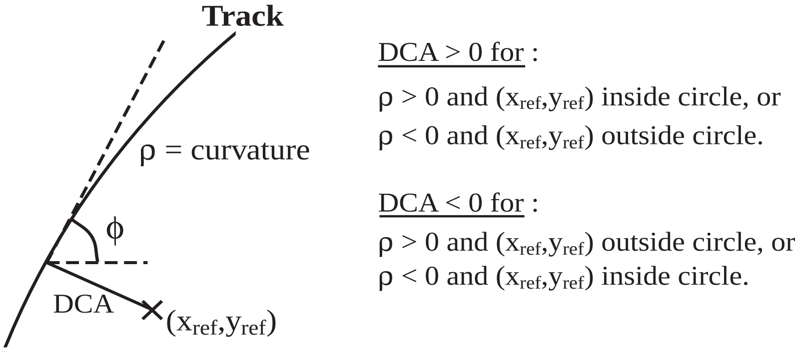

Figure 7.2: Definition of the sign of DCA, in the L3 analysis.

consider that the decay products of the tau in a signal event are in a very small cone along the direction of their mother particle due to the high momentum of the tau itself and the low energy available to the decay in its rest frame. The tracks from these particles will thus have similar (large) DCAs. Typical selection efficiencies are listed in Table 7.4, for different $\tilde{\tau}$ masses and decay lengths.

Cut Variable	short decay length	medium decay length
Average DCA	$> 0.326\ mm$	$> 2.96\ mm$
$E_{visible}$	$> 19.7\ GeV; < 91.7\ GeV$	$> 25.6\ GeV; < 95.6\ GeV$
$Acollinearity$	< 2.89	—
$Acoplanarity$	< 2.96	—
$cos(\theta_{thrust})$	< 0.69	< 0.85

Table 7.3: Cut variables and their values for optimized selection of $\tilde{\tau}$ in GMSB models with short and medium decay length.

7.2.3 Selections for scalar taus with long decay length

For $\tilde{\tau}$ with long decay length, information on the measured ionization of tracks (dE/dx) in the TEC is very important. A new simulation of dE/dx was developed, as discussed in Chapter 5, which solved many of the problems in the old version. Applying a dE/dx cut is very efficient for rather heavy $\tilde{\tau}$, however it loses its power for lighter $\tilde{\tau}$ ($M_{\tilde{\tau}} < 70\%\sqrt{s}$). Since we carry out this analysis for data samples in 1999 and 2000 only, which has center-of-mass energies ranging from 192 GeV to 208 GeV, we developed two analyses for $\tilde{\tau}$ with long decay length: one using a dE/dx cut for high $\tilde{\tau}$ mass, and one using kinematic cuts only for low $\tilde{\tau}$ mass.

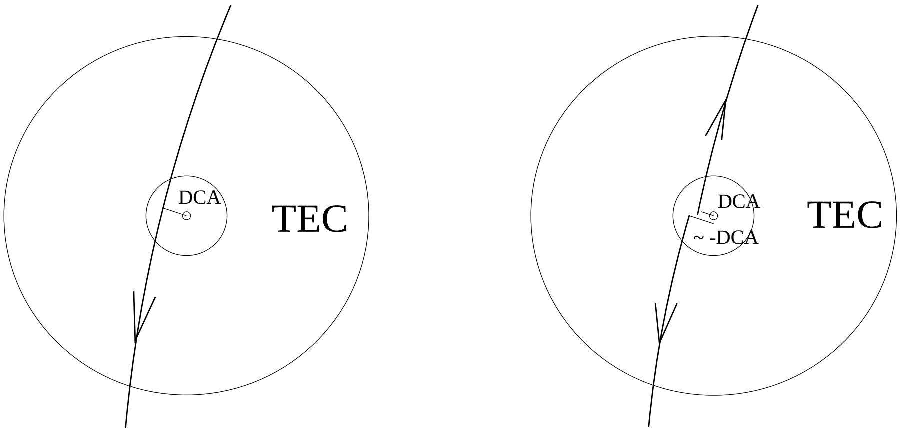

One cosmic muon goes through the TEC

Reconstructed as two back to back tracks with opposite signed DCA

Figure 7.3: Schematic view of a cosmic muon passing through the L3 TEC. Due to the reconstruction algorithm, the track is split into two sections, recognized as two outgoing particles with roughly equal $|DCA|$, but opposite sign.

Pre-selection

The two selections for long-lived scalar taus share the same pre-selection, with the cut variables and their values listed in Table 7.5. Basically, we require two back to back tracks with reasonable momentum and good DCA. Although we can apply a strict cut on the best DCA of tracks, we cannot require an in-time scintillator hit, since the scalar tau may be very heavy and travel at a low speed. We thus added an additional veto cut to remove any remaining cosmic muons: we reject events with $E_{visible} - P_{\mu(s)} < 10\ GeV$ and $E_{visible} < 30\ GeV$. The typical energy deposited by a cosmic muon in the L3 calorimeters is below 10 GeV. Requiring $E_{visible} < 30\ GeV$ is based on the fact that for scalar tau signals with this kind of low momentum, it cannot penetrate the L3 calorimeters and form tracks in the muon chambers.

The number of selected data events and the expected background level from Standard Model processes for 1999 and 2000 are shown in Table 7.6. We also checked the distributions of all the important variables. Figure 7.7 and Figure 7.8 show that the data distributions after pre-selection for a scalar tau with long decay length agree very well with the Monte Carlo distributions resulting from Standard Model backgrounds.

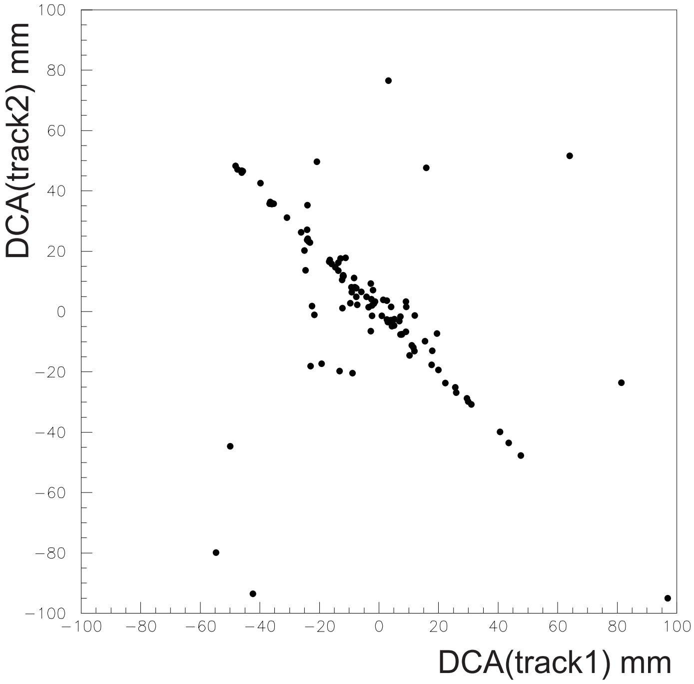

Figure 7.4: Since cosmic rays are recognized as two outgoing particles, they can be found along the band near DCA(track1)+DCA(track2)=0.

Final selections

The optimization of the final selection is straightforward. We used signal Monte Carlo samples from medium to very long decay length with different scalar tau masses for the two selections. The cut variables and optimized values for the final selections are listed in Table 7.7. To have a good overall coverage of possible scalar tau signals with any decay length, we always consider the case of one scalar tau decay inside of the L3 detector together with the two stable stau case, so that we won't leave any gap uncovered between the selections of medium decay length and long decay length.

The selection using kinematic cuts focuses on relatively low scalar tau mass, where we require two good back-to-back tracks with high momentum. The requirement on the ϕ angle difference between the two tracks is much stronger than that for the θ angle difference due to the higher resolution in the $r-\phi$ plane provided by the L3 TEC. We also require both tracks to be detected by the inner TEC chamber (most inner hit ≤ 8). The cut on θ_{thrust} actually selects events in the barrel region. For a scalar tau in this mass region, they always can reach the muon chambers and be recognized as energetic 'muons,' if

efficiency (short) %	Decay Length (cm)							
$M_{\tilde{\tau}}$ (GeV)	0.01	0.1	1.0	10.0	40.0	90.0	150.0	400.0
45	5.4	20.3	29.8	6.1	2.4	1.8	1.2	0.5
75	8.0	27.9	32.2	5.4	3.4	2.5	1.6	0.3

efficiency (medium) %	Decay Length (cm)							
$M_{\tilde{\tau}}$ (GeV)	0.01	0.1	1.0	10.0	40.0	90.0	150.0	400.0
45	0.4	0.5	16.1	38.1	31.6	23.6	16.4	5.6
85	1.3	1.5	36.9	49.0	43.6	29.9	20.8	8.8

Table 7.4: Efficiency of $\tilde{\tau}$ analysis from selections based on short and medium impact parameter.

they live long enough. However, we also take into account the case with one scalar tau decaying inside the L3 inner detectors, so we only cut on the visible energy other than the energy of the most energetic 'muon.' This energy could be from another 'muon,' or from the decay products of a scalar tau.

The selection using TEC dE/dx information is aimed at high scalar tau mass. In this case, the SUSY particle may or may not be able to pass through the calorimeters and reach the muon chambers. And we want to have good efficiency for events where one scalar tau decays early. So the final cuts used as much information from the TEC and calorimeters as possible, and avoided any cuts on detected muon tracks. We have a pretty strong cut on the dE/dx information which removes almost all the background, except those events with large fluctuations in dE/dx.

Typical selection efficiencies are listed in Table 7.8, for different $\tilde{\tau}$ mass and decay lengths.

7.3 Results

The results of all the selections obtained from the data samples of 1999 and 2000 are shown in Table 7.9, in which the selection for a scalar tau with prompt decay is obtained by the parametrized selection method described in Chapter 6 by setting the parameter Z = E_{beam}. No significant indication of $\tilde{\tau}$ production has been observed.

Following the procedure described in Section 6.3, we derived upper limits on the $\tilde{\tau}$ production cross

Cut Variable	long decay length
DCA_{best}	$< 5\ mm$
$T_{best\ scint}$	$> -3\ ns$
Z_0	$< 30\ mm$
$N_{good\ tracks}$	≥ 2
$P_{most\ energetic\ track}$	$> 7\ GeV$
$P_{2nd\ most\ energetic\ track}$	$> 7\ GeV$
$\Delta\theta(track1, track2)$	$< 1\ rad$
$\Delta\phi(track1, track2)$	$< 1\ rad$
$E_{ALR+Lumi}$	$< 5\ GeV$
additional veto cuts	Yes

Table 7.5: Cut variables and their values for the pre-selection of a $\tilde{\tau}$ in GMSB models with long decay length.

	long decay length	
year	N_{data}	N_{MC}
1999	683	690.2
2000	538	495.0

Table 7.6: Number of data events selected and the expected Standard Model background level after pre-selection for a scalar tau with long lifetime.

section at 95% C.L. for scalar tau production at $\sqrt{s} = 205\ GeV$, as a function of its mass and lifetime (see Figure 7.9), taking into account the background contributions. To derive the cross section limit, we combined the results from 1999 and 2000 from all the selections.

As we did in Section 6.3, we combine the most conservative production cross section estimation in the framework of the MSSM with gauge mediated SUSY breaking models with the production cross section limit we obtained in this analysis, and get the mass limit for a scalar tau. We show in Figure 7.10 the excluded region in the $M_{\tilde{\tau}}-$lifetime plane, at 95% C.L., obtained by using all the selections. The excluded region by prompt decay selection takes into account all the available LEP2 data, while the other selections combined results from 1999 and 2000 only. For the selections of short, medium and long decay length, we also take into account the possible combinations among them to achieve the best

Cut Variable	kinematic cuts	using dE/dx
$E_{visible}$	—	$> 10.2\ GeV; < 115.0\ GeV$
$E_{visible} - P_{\mu_1}$	$> 19.5\ GeV; < 77.7\ GeV$	—
P_t	$> 5.5\ GeV$	—
$cos(\theta_{thrust})$	< 0.66	< 0.74
$\Delta\phi(track1, track2)$	$< 0.005\ rad$	—
$\Delta\theta(track1, track2)$	$< 0.43\ rad$	—
P_{track1}	$> 20.0\ GeV$	—
Wire No. of inner most hit of track1	≤ 8	—
P_{track2}	$> 19.2\ GeV$	—
Wire No. of inner most hit of track2	≤ 8	—
$(dE/dx)_{track1} \times (dE/dx)_{track2}$	—	> 1.539

Table 7.7: Cut variables and their values for the optimized selection of a $\tilde{\tau}$ in GMSB models with long decay length, using kinematic cuts only, and using dE/dx information.

exclusion. From this analysis, we obtain an absolute limit on the $\tilde{\tau}$ mass, regardless of its lifetime:

$$M_{\tilde{\tau}} \ > \ 80\ GeV \quad (expected\ 79\ GeV). \tag{7.1}$$

The expected limit is an average limit obtained from a large number of Monte Carlo experiments generated according to the probability density function of all the possible results.

efficiency (long 1) %	Decay Length (cm)							
$M_{\tilde{\tau}}$ (GeV)	0.1	1.0	10.0	40.0	90.0	150.0	400.0	1000.
45	0	0	0.2	6.5	16.1	20.3	19.0	19.8
75	0	0	0.1	8.8	20.1	25.4	23.0	23.2

efficiency (long 2) %	Decay Length (cm)							
$M_{\tilde{\tau}}$ (GeV)	0.1	1.0	10.0	40.0	90.0	150.0	400.0	1000.
45	0	0	0	0	0	0	0	0
75	0	0	0.3	7.5	13.5	14.8	17.8	18.2
95	0	0	1.5	23.5	39.6	46.6	47.9	47.3

Table 7.8: Efficiency of $\tilde{\tau}$ analysis from each selection. Long 1 refers to the selection with kinematic cuts only, while long 2 refers to that also uses dE/dx information.

data	prompt		short		medium		long (1)		long (2)	
sample	N_{data}	N_{MC}	N_{data}	N_{MC}	N_{data}	N_{MC}	N_{data}	N_{MC}	N_{data}	N_{MC}
1999	57	60.5	8	7.1	3	1.1	6	4.8	1	0.2
2000	50	51.0	13	6.9	2	2.6	9	4.9	0	0.2

Table 7.9: Results of $\tilde{\tau}$ analysis: the number of selected data events and expected Standard Model background in each selection. Long (1) refers to the selection with kinematic cuts only, while long (2) refers to that also uses dE/dx information.

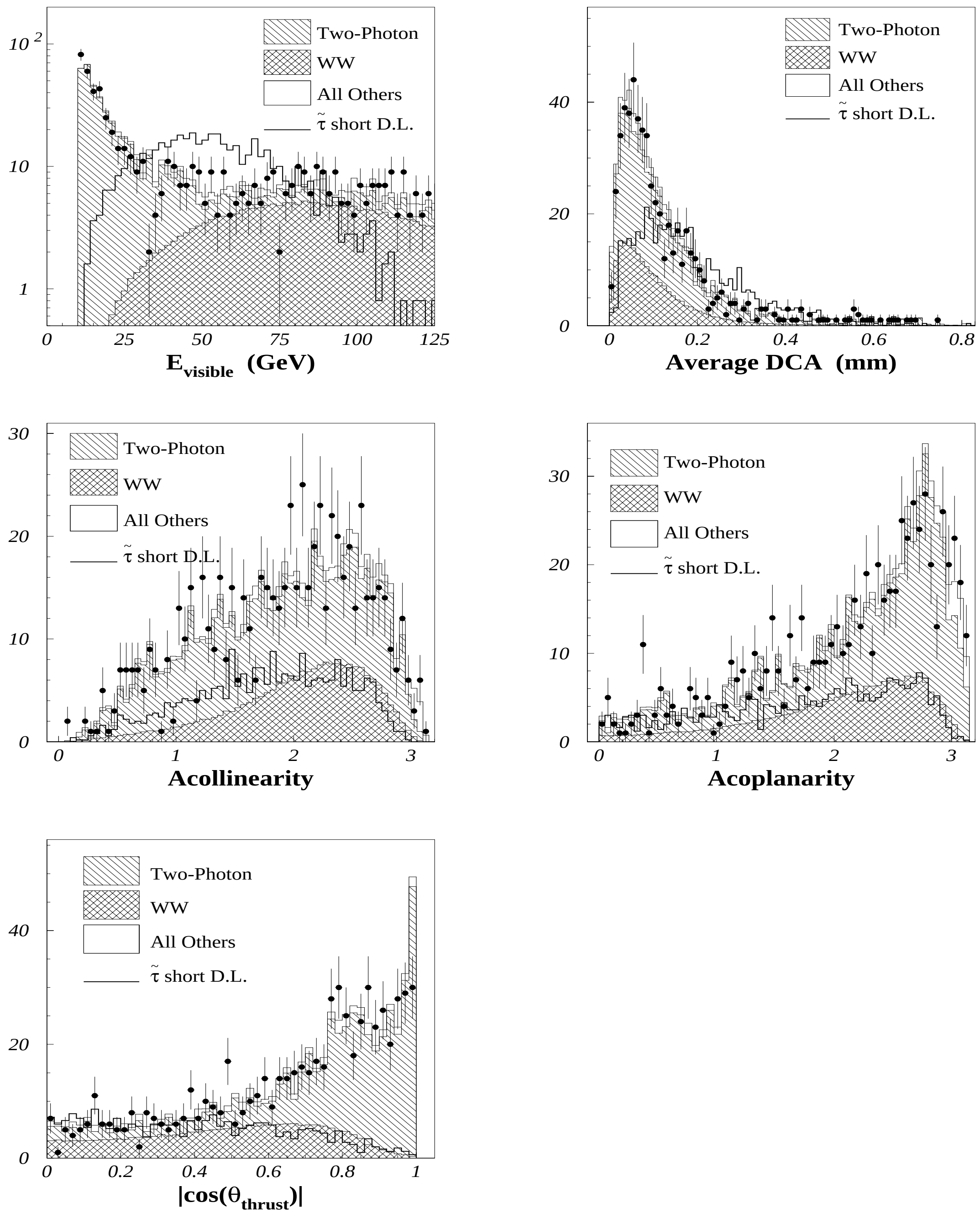

Figure 7.5: Data and Monte Carlo simulation agreement on important variables: after pre-selection in the search for a scalar tau with short decay length. Plots shown are for the data sample of 1999. The simulated $\tilde{\tau}$ signal with $M_{\tilde{\tau}} = 75\,GeV$ and decay length of $\sim 1\,mm$ is also shown as an open histogram in each plot.

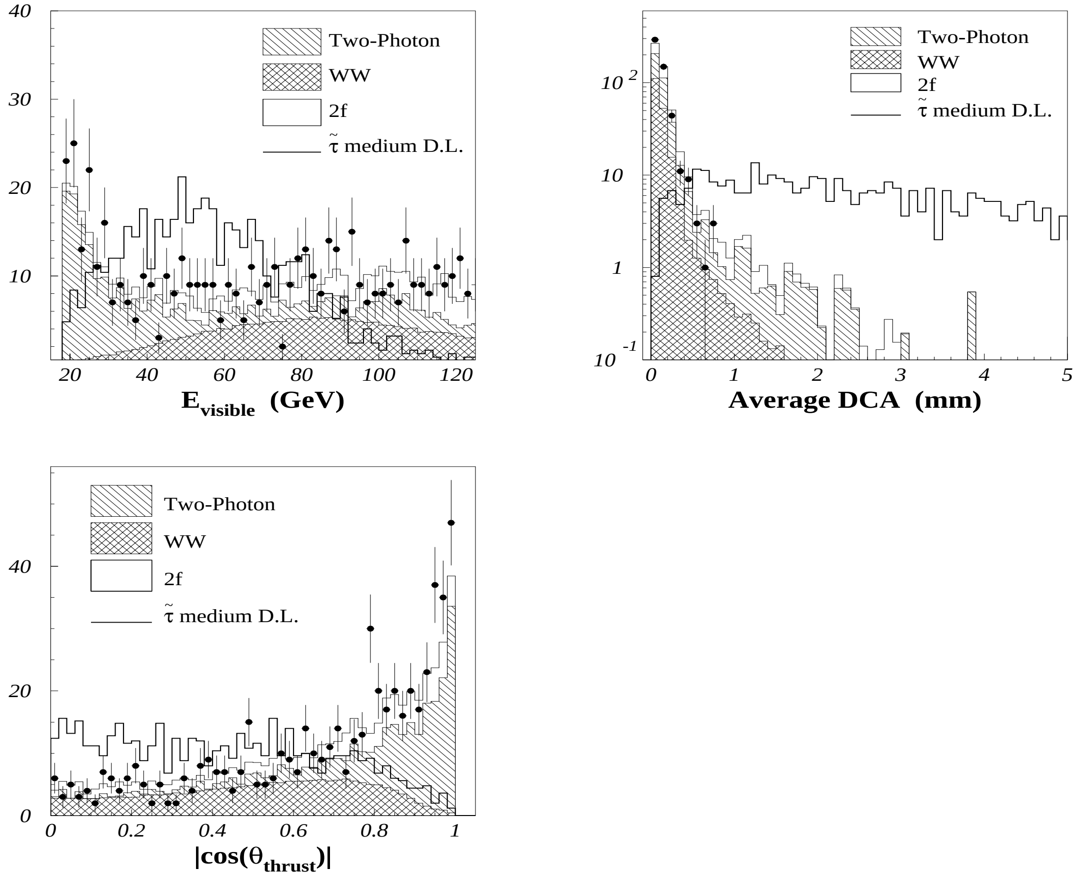

Figure 7.6: Data and Monte Carlo simulation agreement on important variables: after pre-selection in the search for a scalar tau with medium decay length. Plots shown are for the data sample of 1999. The simulated $\tilde{\tau}$ signal with $M_{\tilde{\tau}} = 75\ GeV$ and decay length of $\sim 1\ cm$ is also shown as an open histogram in each plot.

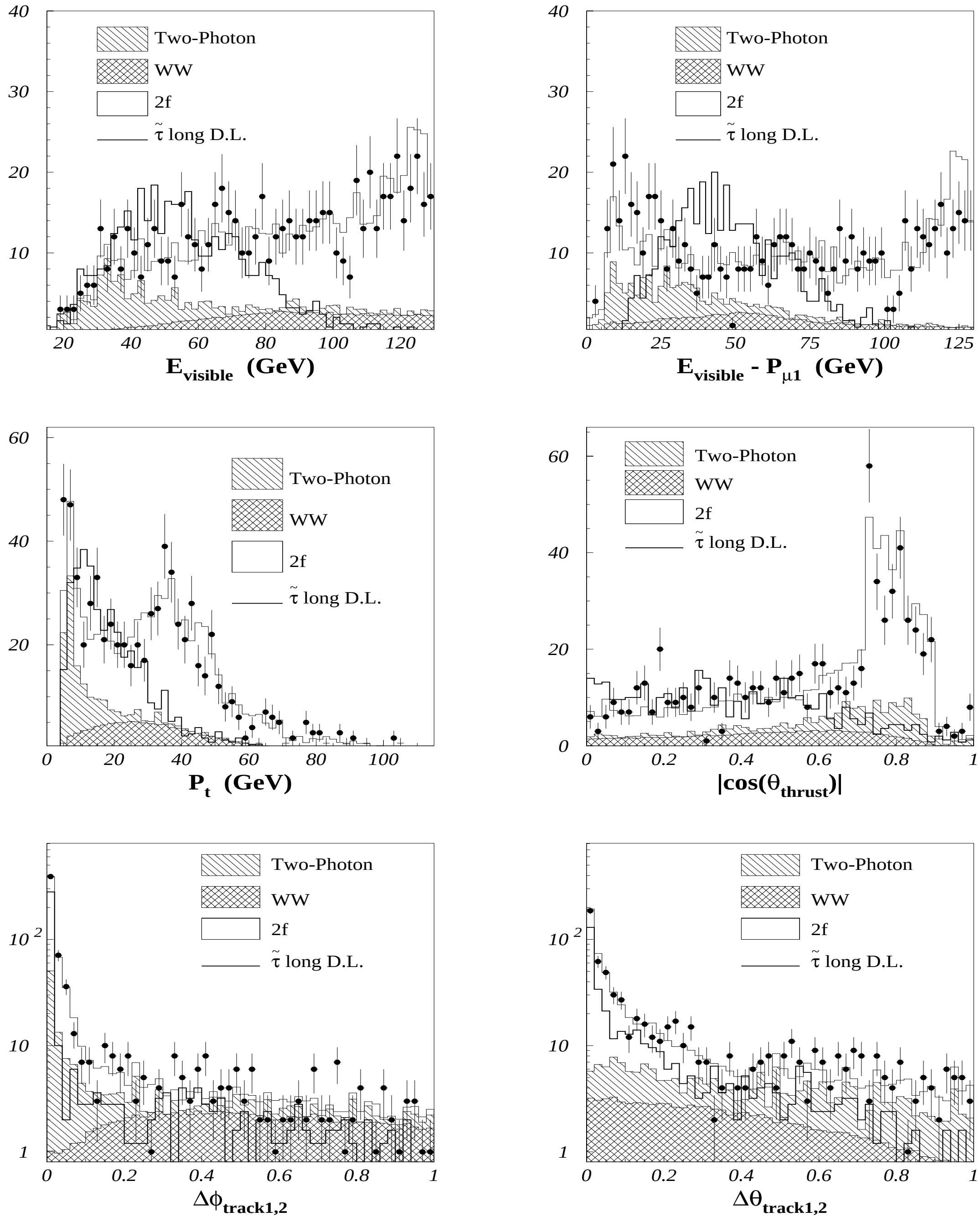

Figure 7.7: Data and Monte Carlo simulation agreement on important variables: after pre-selection for a scalar tau with long decay length. Plots shown are for the data sample of 1999. The simulated $\tilde{\tau}$ signal with $M_{\tilde{\tau}} = 75\ GeV$ and a decay length of $\sim 90\ cm$ is also shown as an open histogram in each plot.

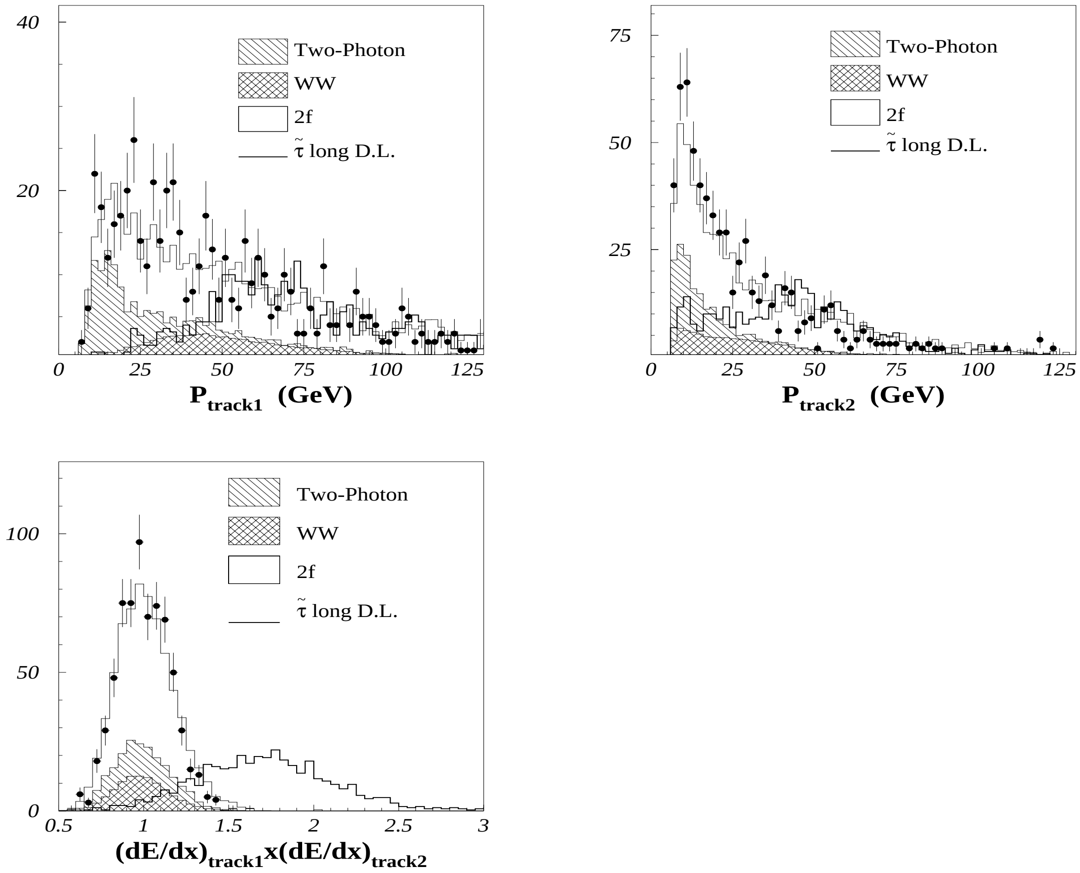

Figure 7.8: Data and Monte Carlo simulation agreement on important variables (continued): after pre-selection for a scalar tau with long decay length. Plots shown are for the data sample of 1999. The simulated $\tilde{\tau}$ signal with $M_{\tilde{\tau}} = 75\ GeV$ and a decay length of $\sim 90\ cm$ is also shown as an open histogram in each plot.

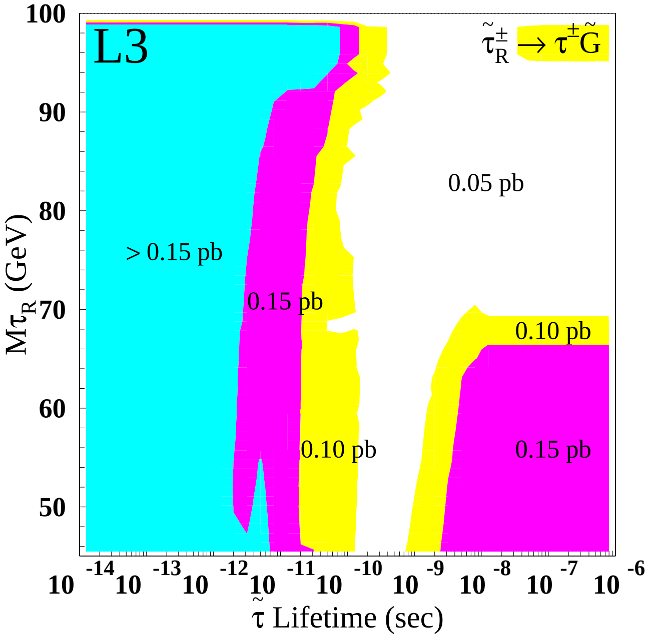

Figure 7.9: Model independent limit on the production cross section of $\tilde{\tau}$ at $\sqrt{s} = 205$ GeV, as a function of $M_{\tilde{\tau}}$ and its lifetime.

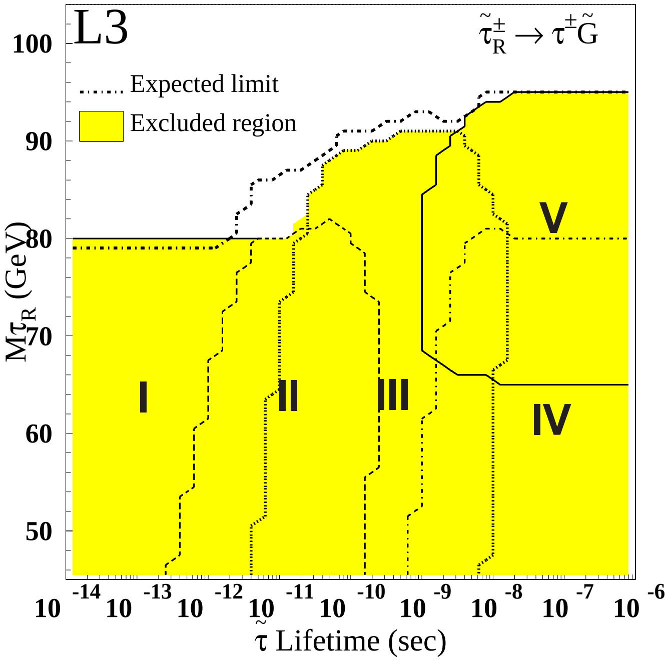

Figure 7.10: Excluded region at 95% C.L. in the $M_{\tilde{\tau}}$−lifetime plane for $\tilde{\tau}$, using different selections for: I, prompt decay; II, short decay length; III, medium decay length; IV, long decay length using kinematic cuts only; and V, long decay length using dE/dx information.

8. Results and Discussion

In this thesis, we presented the analysis searching for the scalar leptons predicted by supersymmetry theory. We analysed data samples from 1999 and 2000, taken with the L3 detector at LEP. The final results combined previous analyses at lower center-of-mass energies whenever possible. This analysis covers both the SUGRA and GMSB scenarios. We summarize the results obtained from this analysis, and from the combination with other analyses, and draw our conclusions in this chapter.

8.1 Summary of Results

8.1.1 Scalar leptons in SUGRA

To search for scalar leptons in SUGRA, we developed parametrized selections for each slepton flavor. The selected data events are in good agreement with the Standard Model background expectations. And we achieved the following mass limits for scalar leptons, for large ΔM[1] ($\Delta M > 0.3 \times M_{\tilde{l}}$):

$$M_{\tilde{e}_R} > 97\ GeV \quad (\textit{expected}\ 97\ GeV) \tag{8.1}$$

$$M_{\tilde{\mu}_R} > 86\ GeV \quad (\textit{expected}\ 86\ GeV) \tag{8.2}$$

$$M_{\tilde{\tau}_R} > 78\ GeV \quad (\textit{expected}\ 79\ GeV). \tag{8.3}$$

To compare this result with our LEP colleagues, I list the scalar lepton mass limits in the following Table (8.1), together with the LEP combined (ADLO) limit. The differences among the limits obtained by the experiments are mainly due to the differences of the detectors. OPAL didn't provide their selectron result in a comparable format, however, their contribution is properly taken into account in the LEP combined result.

8.1.2 Scalar tau in GMSB models

To search for scalar taus in GMSB models, we developed four new selections for stau signals with short, medium and long decay length. Together with the prompt decay region which is covered by selections

---

[1] The mass difference between scalar lepton and the lightest neutralino.

$\sqrt{s}$ up to 208 GeV			
	$M_{\tilde{e}_R}$ GeV Observed (expected)	$M_{\tilde{\mu}_R}$ GeV Observed (expected)	$M_{\tilde{\tau}_R}$ GeV Observed (expected)
ALEPH	95 (97)	88 (87)	79 (83)
DELPHI	98 (98)	88 (87)	83 (83)
L3	97 (97)	86 (86)	79 (79)
OPAL	— (—)	82 (84)	81 (78)
Combined (ADLO)	99.6 (99.2)	94.9 (91.4)	85.9 (85.8)

Table 8.1: Scalar lepton mass limits at large ΔM from all LEP experiments, as well as the combined result from the LEP SUSY working group [79].

developed in the SUGRA scenario, we are able to set a stau limit for any lifetime:

$$M_{\tilde{\tau}_R} \ > \ 80\,GeV \quad (\textit{expected}\ 79\ GeV). \tag{8.4}$$

To compare with the other LEP experiments, the lifetime independent limit and the mass limit in the very long lifetime region (where they searched for charged heavy stable particles) are shown in Table 8.2 for all the LEP experiments as well as the LEP combined result. The lifetime independent limit is always determined by the prompt decay search, so we compare the limits at the two ends of the possible stau lifetime range. OPAL didn't report its results in a comparable format, however, their contribution is taken into account in the final combination by the LEP SUSY working group.

	$\sqrt{s}$ up to 208 GeV				
	ALEPH Obs.(Exp.)	DELPHI Obs.(Exp.)	L3 Obs.(Exp.)	OPAL Obs.(Exp.)	Combined (ADLO) Obs.(Exp.)
$M_{\tilde{\tau}}$ GeV (overall)	77 (82)	83 (83)	80 (79)	— (—)	87 (90)
$M_{\tilde{\tau}}$ GeV (stable $\tilde{\tau}$)	97 (95)	96 (96)	95 (95)	— (—)	97 (97)

Table 8.2: Scalar tau mass limit for any $\tilde{\tau}$ lifetime (overall) and for a very long lifetime (stable), from all LEP experiments, as well as the combined result from LEP SUSY working group [80].

8.2 Results obtained by combining this and other analyses

Having the results from scalar leptons, we can obtain more exclusion power in the SUSY parameter space by combining the results from different searches.

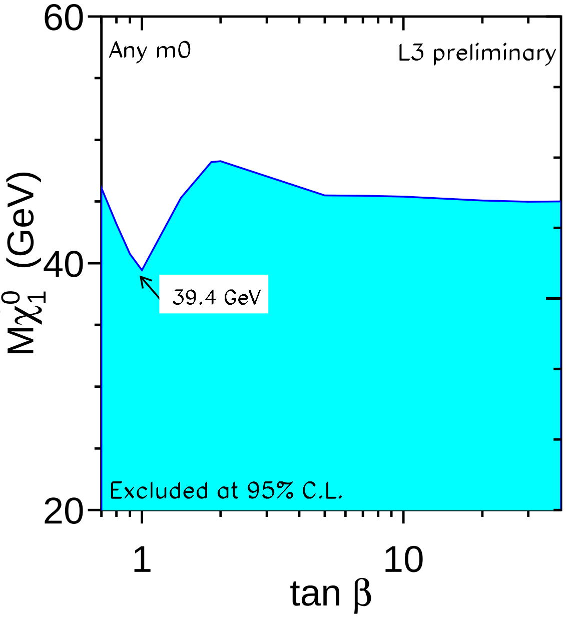

Figure 8.1: Lower limit on $M_{\tilde{\chi}_1^0}$ as a function of $tan\beta$ for any m_0, when combining the slepton, chargino and neutralino searches.

In the framework of the CMSSM, the scalar lepton mass and cross section depend strongly on m_0, the universal scalar mass at the GUT scale. By knowing the cross section limit for scalar leptons at any mass, this analysis can contribute to an indirect limit on the LSP in some region of the parameter space. Figure 8.1 shows this indirect limit on the lightest neutralino for any m_0, obtained by combining the slepton, chargino and neutralino searches. Scalar lepton searches contribute in the low m_0 region, chargino searches contribute mainly in the high m_0 region. For low tanβ values, the neutralino searches give an additional contribution in the intermediate m_0 region [81]. This work is done by Sylvie Lee-Rosier.

Combining the results from stau searches and neutralino searches in GMSB models, one can cover all the possible NLSP scenarios, and thus, obtain exclusion power in more of the parameter space. This has been done by Haijun Yang, using a scan in the parameter space of the minimal GMSB model [2]. Table 8.3 shows the lower limit obtained for SUSY parameters for different numbers of messenger particle pairs[3], in which Λ is the universal mass scale of SUSY particles, M_{mess} is the common messenger mass scale, and N_5 is the number of messenger pairs.

Minimal GMSB		Number of Messenger Pairs (N_5)				
Parameters		1	2	3	4	5
Λ	(TeV)	52	28	20	18	16
M_{mess}	(TeV)	63	40	25	25	25
$m_{\tilde{G}}$	(eV)	1	0.25	0.16	0.10	0.06
$m_{\tilde{\chi}_1^0}$	(GeV)	77.0	74.4	77.6	85.9	95.7
$m_{\tilde{\tau}_1}$	(GeV)	73.9	74.0	73.9	74.0	74.3
$m_{\tilde{\mu}_R}$	(GeV)	95.7	75.8	75.7	76.0	76.0
$m_{\tilde{e}_R}$	(GeV)	95.7	75.8	75.7	76.0	76.0

Table 8.3: Lower limits for SUSY parameters in the minimal GMSB model, from stau and neutralino searches [82].

---

[2] Here, minimal refers to minimum particle content. Compared with the MSSM with gravity mediated SUSY breaking, GMSB models introduce one more messenger sector. In some papers in the literature, it refers to specific models with the number of messenger particle pairs $N_5 = 1$. Here, we consider the $N_5 > 1$ case as well.

[3] The messenger particles are in additional chiral supermultiplets which couple to the ultimate source of supersymmetry breaking, and also couple indirectly to the MSSM through the ordinary $SU(3)_C \times SU(2)_L \times U(1)_Y$ gauge interactions.

8.3 Conclusion

We performed searches for scalar leptons in two major SUSY scenarios using data samples obtained at the highest possible LEP center-of-mass energies. We found no significant excess of events over the expected level of Standard Model processes. Supersymmetry, if it exists, is still hiding somewhere. By searching in a new energy range, we have been able to set new limits on scalar lepton masses and SUSY parameters.

LEP and the four LEP experiments, ALEPH, DELPHI, L3 and OPAL, finished a period of successful running stretching over 11 years. All the results obtained at LEP once again confirmed the Standard Model, with extraordinary precision. The task of searching for new physics has now been passed to the Tevatron, and in the near future, to the LHC.

A. The Hierarchy Problem

The hierarchy problem is not really a difficulty with the Standard Model itself, but rather a disturbing sensitivity of the Higgs potential to new physics in almost any imaginable extension of the Standard Model [12].

The Standard Model Higgs field is a complex scalar H with a potential given by

$$V(H) \;=\; m_H^2\, |H|^2 \;+\; \lambda\, |H|^4. \tag{A.1}$$

This potential has a non-vanishing vacuum expectation value at the minimum, which requires $m_H^2 < 0$, resulting in $\langle H \rangle = \sqrt{-m_H^2/2\lambda}$. From the precise measurement of the properties of the electroweak interaction, we know that m_H^2 is roughly $-(100\ GeV)^2$. However, m_H^2 receives enormous quantum corrections from the virtual effects of every particle which couples, directly or indirectly, to the Higgs field [12].

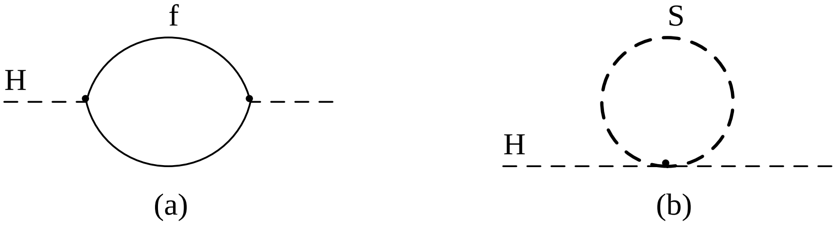

Figure A.1: Quantum corrections to the Higgs (mass)^2 [12].

For example, a fermion f with mass m_f, which couples to the Higgs field through a term $-\lambda_f H f \bar{f}$, will introduce the following correction through the diagram in Figure A.1a:

$$\Delta m_H^2 \;=\; \frac{|\lambda_f|^2}{16\pi^2}\,[-2\Lambda_{UV}^2 \;+\; 6m_f^2\; ln(\Lambda_{UV}/m_f) \;+\; ...], \tag{A.2}$$

in which Λ_{UV} is an ultraviolet momentum cutoff. Similarly, for a scalar particle S with mass m_S, which couples to the Higgs field through a term $-\lambda_S |H|^2 |S|^2$, the correction is (through the diagram in Figure A.1b):

$$\Delta m_H^2 \;=\; \frac{\lambda_S}{16\pi^2}\,[\Lambda_{UV}^2 \;-\; 2m_S^2\; ln(\Lambda_{UV}/m_S) \;+\; ...]. \tag{A.3}$$

The momentum cutoff Λ_{UV} should represent an energy scale at which new physics enters. The problem is that if Λ_{UV} is very large, say at M_P, then the quantum correction to m_H^2 would be many

(30, in the case of M_P) orders of magnitude larger than m_H^2. Such a cancellation of all the huge corrections is extremely unnatural. In addition, all the fermions and the electroweak gauge bosons of the Standard Model owe their masses to $\langle H \rangle$, so that the entire mass spectrum of the Standard Model is sensitive to the cutoff Λ_{UV} [12].

The systematic cancellation of the huge contributions to Δm_H^2 can only be brought about by some sort of symmetry. The supersymmetry theory forced us to introduce two complex scalar fields to each Standard Model Dirac fermion, which is just needed for the cancellation of the quadratically divergent (Λ_{UV}^2) pieces. This cancellation requires that the associated dimensionless couplings should be related as

$$\lambda_S = |\lambda_f|^2 \qquad \text{(A.4)}$$

and this is exactly the relation for particles in the same supermultiplet. So the supersymmetry theory indeed provides a beautiful solution to the hierarchy problem.

B. Prospect for SUSY Searches at Future Colliders

LEP finished a period of successful running stretching over 11 years, but supersymmetry searches will remain one of the main physics goals for experiments at future colliders. Here we briefly discuss supersymmetry searches at Tevatron Run II, LHC, and NLC.

B.1 SUSY Searches at Tevatron Run II and LHC [83, 84]

At hadron colliders, such as Tevatron and LHC, the detectors are capable of measuring isolated electrons, muons, and photons with high P_T, tagging b quarks, and measuring missing P_T, E_T, and energetic jets. The strategy for supersymmetry searches is set according to the capability of these measurements.

Several channels of sparticle production in the R-parity conserving scenario are considered for Run II at the Tevatron. Among them the production of $\tilde{\chi}_1^0\tilde{\chi}_2^0$, $\tilde{\chi}_1^{\pm}\tilde{\chi}_2^0$, $\tilde{t}_1\tilde{t}_1$, $\tilde{b}_1\tilde{b}_1$, and $\tilde{g}\tilde{g}$ are the most important ones. In particular, the stop and sbotom searches are the most promising discovery channels of gravity mediated SUSY model with R-parity conservation. Scalar lepton production processes are not favored due to their low cross sections.

The approximate reach of Run II for the sparticle masses, after collecting 25 (2) fb^{-1} data, is: 150 (110) GeV for $m_{\tilde{\chi}_1^{\pm}}$; 75 (55) GeV for $m_{\tilde{\chi}_1^0}$; 450 (330) GeV for $m_{\tilde{g}}$, provided $m_0 \ < 200\ GeV$. The stop could be observed up to 260 (180) GeV, and sbottom up to 280 (210) GeV. However, due to the nature of the backgrounds at a hadron collider, the low ΔM region in the parameter space is not reachable.

At LHC, similar final states can be searched for. With higher beam energy, the ultimate sensitivity could reach up to 2 TeV for the masses of squarks and gluinos. Moreover, the large cross sections for squarks and gluinos with masses up to about 600 GeV should allow one to discover supersymmetry at the very beginning of LHC. Figure B.1 shows the expected sensitivity in the mSUGRA parameter space, assuming an integrated luminosity of 10 fb^{-1}.

B.2 SUSY Searches at NLC [86]

At NLC, the supersymmetry searches will be carried out using the same channels as we did at LEP: chargino, neutralino, scalar lepton, and scalar quark productions are the most important channels. Compared to LHC, the lower center-of-mass energy of NLC will be compensated by its clean background conditions, so that one can search for sparticles with the lowest masses. Figure B.2 shows a comparison of the supersymmetry reach by the LHC, and NLC at different center-of-mass energies, with their most favored channels: $gg \to \tilde{g}\tilde{g}$ for LHC; $e^+e^- \to \tilde{\chi}_1^+\tilde{\chi}_1^-$ and $e^+e^- \to \tilde{e}_R^+\tilde{e}_R^-$ for NLC.

In addition, NLC may also exploit the ability to adjust the beam energy and to polarize the beam. The former helps to produce just the particles of interest, while the latter helps to measure supersymmetry parameters and separate the signal from the background. If supersymmetry is discovered, NLC will also be able to accurately measure the properties of sparticles within its reach and determine the supersymmetry parameters.

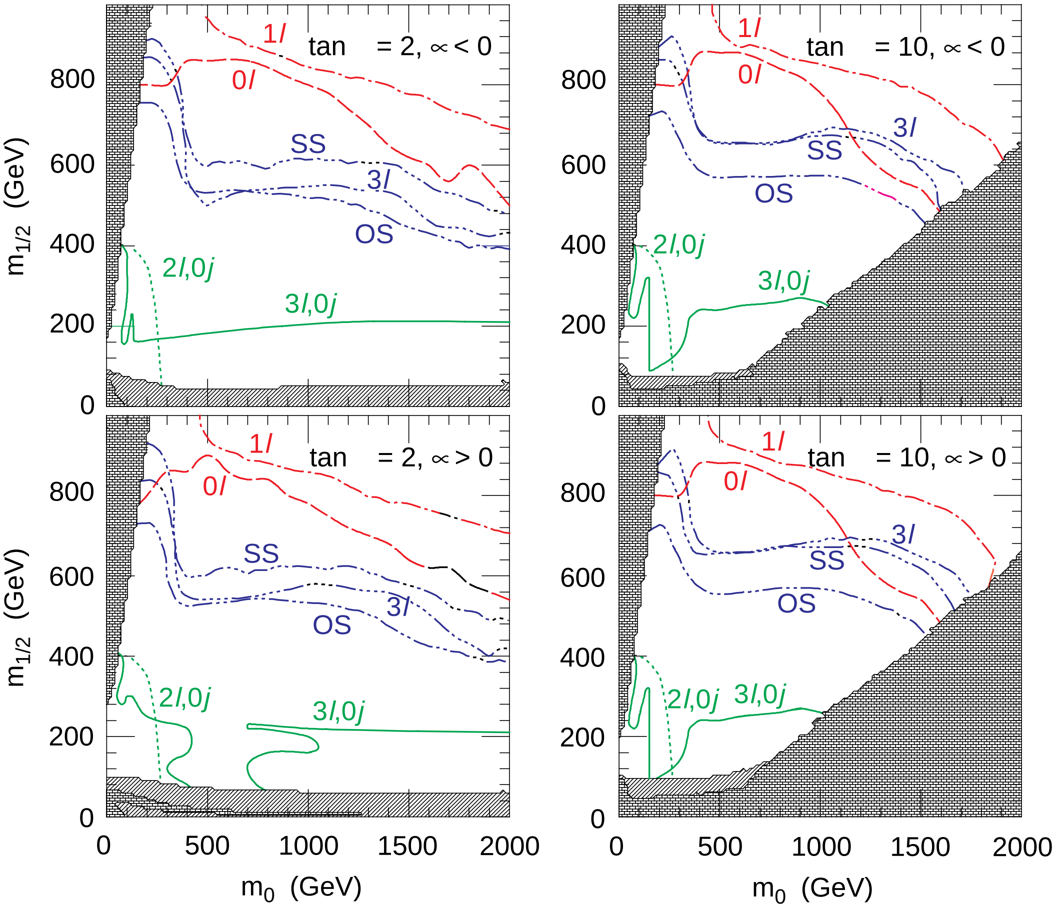

Figure B.1: Expected mSUGRA sensitivity for various signatures in the $m_0 - m_{1/2}$ plane at LHC, assuming an integrated luminosity of 10 fb^{-1}. Different curves indicate the expected sensitivity from different final states: l for lepton, j for jet, SS for lepton pairs with same charge, and OS for lepton pairs with opposite charge [85].

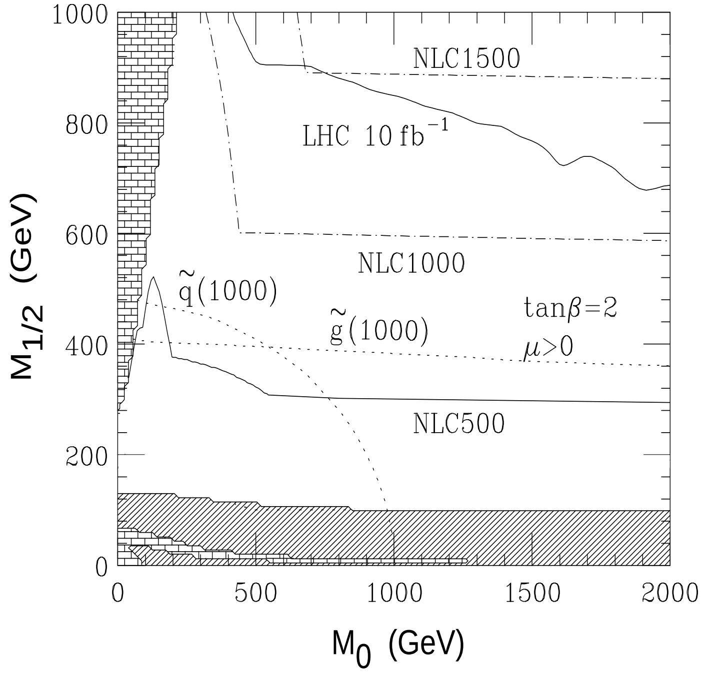

Figure B.2: The supersymmetry reach of various facilities in the mSUGRA model, for tan$\beta = 2$, $A_0 = 0$ and $\mu > 0$. The reach of a $1.2 - 1.5$ TeV NLC is approximately equivalent to that of LHC [86].

Bibliography

[1] N. Cabibbo, Phys. Rev. Lett. 10 (1963) 531

[2] M. Kobayashi and T. Maskawa, Prog. Theor. Phys. 49, (1973) 652

[3] S. Fukuda *et al.*, proceeding Letter, Phys. Rev. Lett. 86 (2001) 5651

[4] S. L. Glashow, Nucl. Phys. 22 (1961) 579,
S. Weinberg, Phys. Rev. Lett. 19 (1967) 1264,
A. Salam, in Elementary Particle Theory, ed. N. Svartholm, Almquist and Wiksell, Stockholm, 1968, 367

[5] C. N. Yang and R. L. Mills, Phys. Rev. 96 (1954) 191

[6] P. W. Higgs, Phys. Lett. 12 (1964),
Phys. Lett. 13 (1964) 508,
Phys. Rev. 145 (1966) 1156

[7] G.'t Hooft, Nucl. Phys. B33 (1971) 173, ibid. B35 (1971) 167

[8] The LEP Electroweak Working Group, http://lepewwg.web.cern.ch/LEPEWWG/,
The LEP Collaborations and the Line Shape Sub-group of the LEP Electroweak Working Group, CERN-EP-2000-153

[9] The LEP W Working Group, http://lepww.web.cern.ch/lepww/,
The LEP Collaborations and the LEP W Working Group, L3 note 2695,
The LEP Collaborations and the LEP TCG Working Group, L3 note 2741

[10] J. Drees, Review of Final LEP Results or a Tribute to LEP, hep-ex/0110077

[11] J. Wess, J. Bagger, Supersymmetry and Supergravity, 2nd ed., Princeton University Press, 1991

[12] S. P. Martin, A Supersymmetry Primer, hep-ph/9709356, 1999

[13] M.E. Peskin, D.V. Schroeder, An introduction to Quantum Field Theory

[14] P. Fayet, Phys. Lett. B69 (1977) 489,
P. Fayet, Phys. Lett. B84 (1979) 416

[15] S. Dimopoulos, H. Georgi, Nucl. Phys. B193 (1981) 150,
N. Sakai, Z. Phys. C11 (1981) 153

[16] H. Goldberg, Phys. Rev. Lett. 50, (1983) 1419,
J. Ellis *et al.*, Nucl. Phys. B238, (1984) 453

[17] G.F Giudice, R. Rattazzi, Phys. Reports 332 (1999) 419

[18] L. Girardello and M. Grisaru, Nucl. Phys. B194 (1982) 65,
H. Harada and N. Sakai, Prog. Theor. Phys. 67 (1982) 67.

[19] S. Dimopoulos, D. Sutter, Nucl. Phys. B452 (1995) 496

[20] K. Inoue *et al.*, Prog. Theor. Phys. 68 (1982) 927, 71 (1984) 413

[21] F. Gabbiani *et al.*, Nucl. Phys. B477 (1996) 321,
J. Ellis, D. V. Nanopoulos, Phys. Lett. B110 (1982) 44

[22] L. Ibáñez, G.G. Ross, Phys. Lett. B110 (1982) 215,
L. Ibáñez, Phys. Lett. B118 (1982) 73,
J. Ellis *et al.*, Phys. Lett. B121 (1983) 123,
J. Ellis *et al.*, Phys. Lett. B125 (1983) 275,
L. Alvarez-Gaumé, J. Polchinski, M. Wise, Nucl. Phys. B211 (1983) 495,
G. Kane, Phys. Rev. D49 (1944) 6173

[23] M. Dine, A.E. Nelson, Phys. Rev. D48 (1993) 1277;
M. Dine, A.E. Nelson, Y. Shirman, ibid. D51 (1995) 1362;
M. Dine *et al.*, ibid. D53 (1996)2658

[24] ALEPH Collab., D. Decamp *et al.*, Nucl. Inst. Meth. A294 (1990) 121

[25] DELPHI Collab., P. Aarnio *et al.*, Nucl. Inst. Meth. A303 (1990) 233

[26] L3 Collab., B. Adeva *et al.*, Nucl. Inst. Meth. A289 (1990) 35

[27] OPAL Collab., K. Ahmet *et al.*, Nucl. Inst. Meth. A305 (1991) 275

[28] The LEP Collider: from Design to Approval and Commissioning, The John Adams Memorial Lecture, CERN, 26 November 1990

[29] R. W. Assmann, LEP Operation and Performance with Electron-Positron Collisions at 209 GeV, Chamonix XI

[30] P. Brown *et al.*, Ultimate Performance of the LEP RF System, Proceedings of the 2001 Particle Accelerator Conference, Chicago

[31] Werner Herr, Which Optics Allows the Highest Energy, CERN, SL Division

[32] G. Arduini *et al.*, Electron-Positron Collisions at 209 GeV in LEP, Proceedings of the 2001 Particle Accelerator Conference, Chicago

[33] L. Ardaudon *et al.*, Accurate Determination of the LEP Beam Energy by Resonant Depolarization, CERN SL/94-71 (BI), 1994

[34] L. Ardaudon *et al.*, The Energy Calibration of LEP in 1991, CERN-PPE/92-125, 1992

[35] A.A. Sokolov, I.M. Ternov, Dokl. Akad. Nauk. SSSR 153 (1963) 1052

[36] G. Grun *et al.*, A Newly Observed Effect Affects the LEP Beam Energy, CERN-SL 96-036

[37] LEP energy working group, Evaluation of the LEP centre-of-mass energy for data taken in 1999, 2000/01

[38] LEP energy working group, Evaluation of the LEP centre-of-mass energy for data taken in 2000, 2001/01

[39] B. Dehning *et al.*, Status of the LEP2 Spectrometer Project, Proceedings of EPAC 2000, Vienna, Austria.

[40] C. Ainsley, LEP2 Beam Energy Measurement Using Radiative Return Events, ICHEP'02, http://www.ichep02.nl/Transparencies/EW/EW-2/ew-2-1.ainsley.pdf

[41] G. von Holtey, Particle Backgrounds at the LEP Detectors at 94.5 GeV, Chamonix IX

[42] Physics at LEP2, vol 1, CERN yellow report, CERN 96-01 v1

[43] M. Lamont, Twelve Years of LEP, Proceedings fo the 2001 Particle Accelerator Conference, Chicago, USA

[44] The Construction of L3, April 1985

[45] M. Acciarri *et al.*, The L3 silicon microvertex detector, Nucl. Inst. Meth. A351 (1994) 300

[46] H. Akbari *et al.*, The L3 vertex detector: design and performance, Nucl. Inst. Meth. A315 (1992) 161

[47] The L3 Collaboration, Results from the L3 Experiment at LEP, CERN-PPE/93-31, Phys. Rep. 236 Nos. 1 & 2 (1993) 1.

[48] A. Bay *et al.*, The Xenon Monitor of the L3 Electromagnetic Calorimeter, Nucl. Instrum. Methods Phys. Res.A (1992) 1-2, 119-128, Preprint UGVA-DPNC 1992/01-150

[49] H. Ma, H. Newman, R. Y. Zhu, and R. Hamm, Nucl. Instr. Meth. A281 (1989) 467
H. Ma *et al.*, Nucl. Instr. Meth. A274 (1989) 113

[50] R. Y. Zhu *et al.*, Nuclear Physics B (Proc. Suppl.) 44 (1995) 109

[51] Wenwen Lu, Caltech, A Study of Bhabha Scattering at the Z Resonance, PhD thesis, 1997

[52] A. Favara *et al.*, Nuclear Physics B (Proc. Suppl.) 78 (1999) 456

[53] I. C. Brock *et al.*, Luminosity measurement in the L3 detector at LEP, Nucl. Instr. Meth. A381 (1996) 236-266

[54] O. Adriani *et al.*, The L3+C detector, an unique tool-set to study cosmic rays, accepted by Nucl. Instr. Meth. A (2002)

[55] S. Ahlen *et al.*, The L3 Radiation Monitor, Nucl. Inst. Meth. A369 (1996) 92-100

[56] S. Ahlen *et al.*, The Operational Results of the L3 Radiation Monitor in 1995 and 1996, L3 Internal Note 2145, 1997

[57] S. Ahlen *et al.*, The Operational Results of the L3 Radiation Monitor in 1997, L3 Internal Note 2215, 1998

[58] C.H. Lin *et al.*, The Operational Results of the L3 Radiation Monitor in 1998, L3 Internal Note 2361, 1999

[59] Boston University, L3 Group, The Radiation Monitor System Data Summary for 1993 and 1994 Runs, L3 Internal Note 1709, 1995

[60] Aly Aamer Syed, Particle Correlations in Hadronic Decays of the Z Boson, Ph.D. Thesis of L3 experiment

[61] Gerald Grenier, Search for Radiative Pair Production of Charginos with masses close to the LSP mass at $\sqrt{s} = 189GeV$, L3 Internal Note 2491, 2000

[62] Private communication with Gerald Grenier

[63] CERN Program Library Long Writeup W5013, GEANT – Detector Description and Simulation Tool, CERN, Geneva 1993. http://wwwinfo.cern.ch/asdoc/geant_html3/geantall.html

[64] Patrick Deglon, Identification de π, K et p provenant de l'interaction de deux photons et etude de la section efficace de production de paires $\pi^+ \pi^-$, $K^+ K^-$ et $p \bar{p}$, travail de deplome, 1997

[65] L. Landau, J. Physics (USSR) 8 (1944) 201

[66] CERNLIB Short Writeup, http://wwwinfo.cern.ch/asdoc/cernlib.html

[67] CERNLIB Short Writeup, http://wwwinfo.cern.ch/asdoc/shortwrupsdir/g110/top.html

[68] J.E. Moyal, Theory of ionization fluctuations, Phil. Mag. 46 (1955) 263

[69] Particle Data Group, Review of Particle Physics

[70] R. M. Sternheimer, R. F. Peierls, General Expression for the Density Effect for the Ionization Loss of Charged Particles, Physical Review B 3(1971) 3681

[71] Private communication with Chih-Hsun Lin

[72] S. Braccini, L3 note 2631, Jan. 31, 2001

[73] For a recent review, see P. Nath, "SUSY/SUGRA/String Phenomenology", hep-ph/9708221 and references therein

[74] S. Catani *et al.*, Phys. Lett. B 249(1991) 432;
S. Bethke *et al.*, Nucl. Phys. B 370(1992) 310

[75] A. Favara *et al.*, L3 Internal Note 1728, March 1995

[76] Thomas Junk, Confidence Level Computation for Combining Searches using the Likelihood Ratio, OPAL Technical Note TN-570

[77] L. Ibanez, Phys. Lett. B118 (1982) 73;
R. Barbieri *et al.*, Phys. Lett. B119(1982) 343

[78] Private communication with Wolfgang Lohmann

[79] http://lepsusy.web.cern.ch/lepsusy/www/sleptons_summer02/slep_2002.html

[80] http://lepsusy.web.cern.ch/lepsusy/www/sleptons_summer02/gmsb.html

[81] L3 collaborations, L3 internal note 2731, March 6, 2002

[82] Haijun Yang, L3 Analysis Meeting, April 24, 2002;
http://tenaya.physics.lsa.umich.edu/ hyang/talks.html

[83] A. Lipniacha, Can SUSY be Found at the Tevatron Run II?, 4th Nordic Workshop for the LHC Physics, December, 2001

[84] M. Dittmar, SUSY discovery strategies at the LHC, hep-ex/9901004

[85] H. Baer *et al.*, hep-ph/9512383

[86] J.A. Bagger, Supersymmetry at LHC and NLC, hep-ph/9709335